Padova University, Padova, Italy

Department of Developmental Psychology

Ph.D. School in Psychological Science

Cycle: *XXVI*

Shedding light into the brain: Methodological innovations in optical neuroimaging

Headmaster of the school: Ch.ma Prof.ssa Francesca Peressotti

Supervisor: Ch.mo Prof. Roberto Dell'Acqua

PhD candidate: Sabrina Brigadoi

To Marco

Shedding light into the brain: Methodological innovations in optical neuroimaging

Abstract

Functional near-infrared spectroscopy (fNIRS) and diffuse optical tomography (DOT) are non-invasive techniques used to infer stimulus-locked variations in human cortical activity from optical variations of near-infrared light injected and subsequently detected at specified scalp locations. Relative to functional magnetic resonance imaging (fMRI) and electroencephalography (EEG), these optical techniques are more portable, less invasive and less sensitive to motion artifacts, making them ideal to explore brain activity in a variety of cognitive situations, and in a range of populations, including newborns and children.

FNIRS and DOT measure stimulus-locked hemodynamic response in the form of changes in oxy- (HbO) and deoxy- (HbR) hemoglobin concentration taking place in specific areas. This signal is however structurally intertwined with physiological noise owing to cardiac pulsations, respiratory oscillations and vasopressure wave. Furthermore, the absolute magnitude of hemodynamic responses is substantially smaller than these non-informative components of the measured optical signal, and has a frequency which largely overlaps with that of the vasopressure wave. Thus, recovering the hemodynamic response is a challenging task. Several methods have been proposed in the literature to try to reduce physiological noise oscillations and recover the hemodynamic response, but none of them has become a common standard in the optical signal

processing pipeline. In this thesis, a novel algorithm, devised to overcome a large subset of drawbacks associated with the use of these literature techniques, is presented and validated.

Reduced sensitivity to motion artifacts notwithstanding, the optical signal must always be assumed as contaminated by some form of mechanical instability, most prominently during signal acquisitions from pathological (e.g., stroke patients) or difficult (e.g., newborns) populations. Several techniques have been proposed to correct for motion artifacts with the specific aim of preserving contaminated measures as opposed to rejecting them. However, none of them has become the gold standard in the optical signal processing pipeline, and there are currently no objective approaches to choose the most appropriate filtering technique based on objective parameters. In fact, due to the extreme variability in shape, frequency content and amplitude of the motion artifacts, it is likely that the best technique to apply is data-dependent and, in this vein, it is essential to provide users with objective tools able to select the best motion correction technique for the data set under examination. In this thesis, a novel objective approach to perform this selection is proposed and validated on a data-set containing a very challenging type of motion artifacts.

While fNIRS allows only spectroscopic measurements of hemoglobin concentration changes, DOT allows to obtain 3D reconstructed images of HbO and HbR concentration changes. To increase the accuracy and interpretability of DOT reconstructed images, valuable anatomical information should be provided. While several adult head models have been

proposed and validated in this context, only few single-ages head models have been presented for the neonatal population. However, due to the rapid growth and maturation of the infant's brain, single-age models fail to capture precise information about the correct anatomy of every infant's head under examination. In this thesis, a novel 4D head model, ranging from the preterm to the term age, is proposed, allowing developmental neuroscientists to make finer-grained choices about the age-matched head model and perform image reconstruction with an anatomy as similar as possible to the real one.

The outline of the thesis will be as follows. In the first two chapters of this thesis, the state of the art of optical techniques will be reviewed. Particularly, in chapter 1, a brief introduction on the physical principles of optical techniques and a comparison with other more common neuroimaging techniques will be presented. In chapter 2, the components of the measured optical signal will be described and a brief review of state of the art of the algorithms that perform physiological noise removal will be presented. The theory on which optical image reconstruction is based will be reviewed afterwards. In the final part of the chapter, some of the studies and achievements of optical techniques in the adult and infants populations will be reviewed and the open issues and aims of the thesis will be presented.

In chapters 3, 4 and 5, new methodologies and tools for signal processing and image reconstruction will be presented. Particularly, in chapter 3, a novel algorithm to reduce physiological noise contamination and recover the hemodynamic response will be introduced. The proposed

methodology will be validated against two literature methods and results and consequent discussion will be reported. In chapter 4, instead, a novel objective approach for the selection of the best motion correction technique will be proposed. The main literature algorithms for motion correction will be reviewed and the proposed approach will be validated using these motion correction techniques on real cognitive data. In chapter 5, instead, a novel 4D neonatal optical head model will be presented. All the steps performed for its creation will be explained and discussed and a demonstration of the head model in use will also be exhibited.

The last part of the thesis (chapters 6, 7 and 8) will be dedicated to illustrate three distinct examples of application of the proposed methodologies and tools on neural empirical data. In chapter 6, the physiological noise removal algorithm proposed in chapter 3 will be applied to recover subtle temporal differences between hemodynamic responses measured in two different areas of the motor cortex in short- vs. long- duration tapping. In chapter 7, the same algorithm will be applied to reduce physiological noise and recover hemodynamic responses measured during a visual short-term memory paradigm. In both chapters, cognitive results and a brief discussion will be reported. In chapter 8, instead, the neonatal optical head model proposed in chapter 5 will be applied to perform image reconstruction with data acquired on a healthy full term baby. In the same chapter, the importance of motion artifact correction will be highlighted, reconstructing HbO concentration changes images before and after the correction took place.

Far luce sul cervello: Innovazioni metodologiche nelle neuroimmagini ottiche

SOMMARIO

La spettroscopia funzionale nel vicino infrarosso (fNIRS) e la tomografia ottica diffusa (DOT) sono tecniche non invasive che, sfruttando le proprietà della luce nel vicino infrarosso, permettono di misurare l'attività cerebrale. Sorgente e detettore sono posti a contatto con il cuoio capelluto ad una distanza prestabilita. Dall'attenuazione subita dalla luce nel passaggio attraverso i tessuti cerebrali, è possibile ricavare le variazioni nell'attività corticale, che avvengono in seguito alla presentazione di uno stimolo. Rispetto alla risonanza magnetica funzionale (fMRI) ed all'elettroencefalografia (EEG), le tecniche ottiche sono più portatili, meno invasive e meno sensibili agli artefatti da movimento; sono pertanto tecniche ideali per esplorare l'attività cerebrale in numerosi ambiti cognitivi e in un gran numero di popolazioni, come neonati e bambini.

FNIRS e DOT misurano la risposta emodinamica in seguito alla presentazione di uno stimolo nella forma di variazioni nella concentrazione di emoglobina ossigenata (HbO) e deossigenata (HbR) che avvengono in specifiche aree della corteccia. Tuttavia, il segnale misurato non contiene solo la risposta emodinamica d'interesse, ma anche rumore fisiologico, dovuto per esempio alla pulsazione cardiaca, alle oscillazioni dovute alla respirazione e all'onda vasomotrice. Inoltre, la risposta emodinamica d'interesse si presenta di solito con un'ampiezza ridotta rispetto

alle componenti non informative del rumore fisiologico e con una frequenza molto simile a quella dell'onda vasomotrice. Da ciò si deduce come stimare la risposta emodinamica sia un compito molto difficile. Molti metodi sono stati proposti in letteratura per cercare di ridurre il rumore fisiologico e stimare la risposta emodinamica. Tuttavia, ad oggi, non esiste un metodo standard per l'analisi del segnale ottico. In questa tesi, quindi, è stato proposto e validato un nuovo algoritmo, messo a punto per far fronte agli svantaggi associati ai metodi presenti in letteratura.

Nonostante la ridotta sensibilità agli artefatti da movimento, il segnale ottico ne risulta comunque contaminato, soprattutto durante acquisizioni di popolazioni patologiche (per esempio pazienti diagnosticati con ictus) o difficili (come per esempio i neonati). Sono state proposte numerose tecniche per correggere gli artefatti da movimento, invece di eliminare la parte di segnale da essi contaminata. Tuttavia, nessuna di queste tecniche, per il momento, è riuscita a emergere come la più adatta per l'analisi del segnale ottico. In aggiunta a questo, non esistono criteri oggettivi con cui sia possibile selezionare la tecnica migliore da applicare, dato un segnale misurato. Si suppone, infatti, che, data l'estrema variabilità presente negli artefatti da movimento in termini di forma, contenuto in frequenza e ampiezza, la tecnica da applicare sia dipendente dal segnale misurato nello specifico caso. Da ciò emerge la necessità di fornire agli sperimentatori dei criteri oggettivi, che permettano loro di selezionare la tecnica di correzione più adatta ad ogni segnale misurato. In questa tesi, quindi, è stato proposto un innovativo ed oggettivo approccio per

la selezione della tecnica di correzione da utilizzare. La validazione è stata eseguita su dei segnali contenenti una tipologia di artefatto da movimento molto difficile da identificare e correggere.

FNIRS permette di ottenere solo misure spettroscopiche delle variazioni di concentrazione di emoglobina; DOT invece è in grado di ricostruire immagini tridimensionali delle variazioni di concentrazione di HbO e HbR. Per aumentare l'accuratezza e l'interpretabilità delle immagini ricostruite con DOT, è necessario fornire accurate informazioni anatomiche di supporto. Numerosi modelli di teste per tecniche ottiche sono stati proposti e validati nella popolazione adulta. Al contrario, in quella neonatale, i modelli analoghi creati finora sono molto pochi e tutti riferiti ad una sola età neonatale. Tuttavia, nei neonati, il cervello è soggetto ad una crescita ed una maturazione molto rapida. Per questo motivo, modelli riferiti ad una singola età neonatale falliscono nel fornire informazioni anatomiche corrette per ogni neonato sotto esame. In questa tesi si è proposto un innovativo modello 4D di teste per tecniche ottiche, contenente informazioni anatomiche per neonati pretermine e a termine. Questo modello può fornire ai neuroscienziati che lavorano in ambito evolutivo la possibilità di selezionare il modello corrispondente all'età del neonato in esame e ricostruire quindi le immagini di variazione di concentrazione di emoglobina usando un'anatomia il più possibile vicina a quella reale.

L'organizzazione della tesi è la seguente. Nei primi capitoli verrà analizzato lo stato dell'arte delle tecniche ottiche. In particolare nel capitolo 1 verrà presentata una breve introduzione dei principi fisici alla base di queste tecniche alla quale seguirà un confronto con le tecniche di neu-

roimmagini più diffuse. Il capitolo 2 descriverà le componenti del segnale ottico misurato e verrà illustrato lo stato dell'arte relativo ad algoritmi di rimozione del rumore fisiologico. Successivamente sarà esposta la teoria che sta alla base del processo di ricostruzione delle immagini. Nella parte finale del capitolo, invece, verranno presentati alcuni studi che hanno utilizzato tecniche ottiche sia nella popolazione adulta che in età evolutiva. Infine saranno presentati gli scopi di questa tesi.

I capitoli 3, 4 e 5 saranno dedicati alla presentazione di nuovi strumenti e metodologie per l'analisi del segnale ottico e per la ricostruzione di immagini ottiche. In particolare nel capitolo 3 verrà introdotto un nuovo algoritmo per la rimozione del rumore fisiologico e la stima della risposta emodinamica. La metodologia proposta verrà validata tramite il confronto con due algoritmi preesistenti. Il capitolo 4 tratterà il problema degli artefatti da movimento e proporrà un innovativo e oggettivo approccio per la selezione della tecnica di correzione da utilizzare. Le principali tecniche di correzione verranno illustrate e il nuovo approccio verrà validato utilizzando dati cognitivi reali. Nel capitolo 5 verrà presentato un nuovo atlante 4D neonatale di modelli di teste per tecniche ottiche. Verranno descritti tutti i passaggi che hanno portato allo sviluppo di questo atlante e ne sarà riportato un esempio applicativo.

La parte finale di questa tesi (capitoli 6, 7 e 8) presenterà tre distinti esempi applicativi, su dati neurali empirici, delle metodologie e strumenti proposti. L'algoritmo per la rimozione del rumore fisiologico proposto nel capitolo 3 sarà utilizzato nel capitolo 6 per stimare differenze temporali poco evidenti tra risposte emodinamiche, misurate in due di-

verse aree della corteccia durante compiti di movimento manuale di diversa durata. Nel capitolo 7 lo stesso algoritmo verrà applicato a dati acquisiti durante un paradigma di memoria visiva a breve termine. Infine nel capitolo 8 verranno ricostruite immagini di variazioni di concentrazione di emoglobina, utilizzando il modello di teste per tecniche ottiche presentato nel capitolo 5. I dati sono stati acquisiti da un neonato a termine e il modello di testa utilizzato nella ricostruzione è quello relativo all'età corrispondente. Nello stesso capitolo verranno ricostruite immagini di concentrazione sia in presenza che in assenza di tecniche di correzione di artefatti da movimento, evidenziandone così l'importanza.

Table of Contents

ABSTRACT **i**

SOMMARIO **v**

INDEX **x**

PART I. Optical techniques for brain function investigation: Physical principles, methodologies, applications **1**

1 PRINCIPLES AND APPLICATIONS OF OPTICAL TECHNIQUES IN NEUROSCIENTIFIC INVESTIGATIONS **3**

1.1 Historical notes 4

1.2 Physical principles of fNIRS and DOT 5

1.2.1 fNIRS and DOT rationale 5

1.2.2 Theoretical formulation 8

1.2.3 Photon migration forward problem 11

1.3 Classes of NIRS and DOT instrumentations available in the market 12

1.4 Pros and cons of fNIRS and DOT 15

1.4.1 Comparison with EEG 15

1.4.2 Comparison with fMRI 16

1.4.3 Other general advantages and drawbacks of fNIRS/DOT 18

1.5 Conclusive remarks 20

2 fNIRS AND DOT: STATE OF THE ART ON MODELING METHODOLOGIES, OPEN ISSUES AND AIMS OF THE THESIS **21**

2.1 Features of fNIRS and DOT measured signal 21
2.1.1 The hemodynamic response 22
2.1.2 Noise and physiological noise components 24
2.2 State of the art of algorithms for physiological noise removal: The potentials of short- separation channels 28
2.2.1 Frequency filtering 29
2.2.2 Subtraction of a non-activated channel 30
2.2.3 Principal Component Analysis (PCA) 31
2.2.4 General Linear Model (GLM) 32
2.2.5 Wavelet filtering 34
2.2.6 Short-separation channel regression 36
2.3 Image reconstruction 39
2.3.1 Image reconstruction theory 40
2.3.2 DOT optical head models 42
2.3.2.1 Adult optical head models 43
2.3.2.2 Neonatal optical head models 45
2.4 fNIRS and DOT in cognitive neuroscience 47
2.4.1 Infants and children 48
2.4.2 Adults 51
2.5 Open issues and aims of the thesis 54
2.5.1 Open issues 54
2.5.2 Aims of the thesis 55

PART II. New methodologies and tools for fNIRS signal processing and neonatal DOT image reconstruction 57

3 REMCOBA, A NOVEL ALGORITHM FOR PHYSIOLOGICAL NOISE REMOVAL AND HR ESTIMATION FOR fNIRS SIGNALS **59**

3.1 Reference-channel Modeling Corrected Bayesian Approach (ReMCoBA) . . . 60
3.1.1 Step 1: SS-channel modeling and fNIRS data correction . . . 60
3.1.2 Step 2: Single trial Bayesian filtering and hemodynamic response estimation . . . 62
3.2 Literature methods used as reference in the comparison . . 65
3.2.1 Reference-channel based fNIRS data correction following Conventional Averaging (rCA) . . . 66
3.2.2 Conventional Averaging (CA) . . . 67
3.3 Data and indexes used for the assessment . . . 67
3.3.1 Real data . . . 67
3.3.2 Synthetic data . . . 70
3.3.3 Indexes used for comparing methods performances 72
3.4 Results . . . 73
3.4.1 Synthetic data . . . 73
3.4.1.1 Performance indexes results . . . 73
3.4.1.2 ROC analyses . . . 77
3.4.1.3 Precision of ReMCoBA HR estimation . . 79
3.4.2 Real data . . . 81
3.4.3 Investigation of differences between hemispheres and conditions . . . 84
3.5 Considerations and conclusive remarks . . . 85

4 ALGORITHMS FOR MOTION CORRECTION IN FNIRS DATA: A NEW STRATEGY FOR THEIR QUANTITATIVE ASSESSMENT ON REAL DATA **89**
4.1 Motion artifacts in fNIRS signals . . . 89
4.2 Classification of approaches to deal with motion artifacts . 91
4.2.1 Correction vs. rejection . . . 92
4.2.2 Assessment of the performance of motion-correction algorithms . . . 93
4.3 Literature algorithms for motion artifact correction . . . 93

4.3.1 Spline interpolation 94
4.3.2 Kalman filtering 95
4.3.3 Principal Component Analysis 96
4.3.4 Wavelet filtering 97
4.3.5 Correlation-Based Signal Improvement 99
4.4 Data 100
4.5 Data processing 103
4.6 Metrics for comparison 105
4.7 Results 107
4.7.1 Rejection vs. no-motion correction 110
4.7.2 Motion correction techniques vs. no-motion correction 112
4.8 Conclusive considerations and remarks 114
4.8.1 Rejection vs no-motion correction 115
4.8.2 Motion-correction techniques vs no-motion correction 116
4.8.3 Final remarks 119

5 NEONATAL OPTICAL HEAD MODELS FOR DOT IMAGE RECONSTRUCTION **121**
5.1 Preterm to term neonates and DOT 121
5.2 Optical head models 123
5.2.1 Data 123
5.2.2 MRI Atlas pre-processing 124
5.2.3 Multi-layer tissue mask 125
5.2.4 Volumetric tetrahedral mesh construction 127
5.2.5 GM, WM and scalp surface mesh construction . . . 128
5.2.6 Cranial landmarks and 10-5 positions 130
5.3 Demonstration of the head models in use 131
5.4 Results 132
5.5 Conclusive considerations and remarks 134
5.5.1 From baby's cranial landmarks to atlas registration to forward problem solutions 135

5.5.2 Neonatal brain development in MRIs and meshes . 137
5.5.3 Head models' limitations 139
5.5.4 Standard coordinate system for neonatal atlases . . 140
5.5.5 Head models' additional applications 141
5.5.6 Final remarks 141

PART III. Application of the new methodologies and tools to empirical neural activation 143

6 THE ROLE OF M1 AND SMA IN SIMPLE MOTOR TASKS **145**
6.1 Data 147
6.2 Probe placement and fNIRS data acquisition 148
6.3 Signal processing and data analysis 149
6.4 Results 151
6.5 Discussion 152

7 VISUAL SHORT-TERM MEMORY: AN EXPLORATORY STUDY **153**
7.1 Visual short-term memory 153
7.2 Data 155
7.3 Probe Placement and data acquisition 157
7.4 Signal processing and data analysis 158
7.4.1 EEG 158
7.4.2 fNIRS 159
7.5 Results 160
7.6 Discussion 161

8 NEONATAL RESTING STATE: APPLICATION OF THE OPTICAL HEAD MODELS **163**
8.1 Probe placement and DOT data acquisition 164
8.2 Signal processing and image recontruction 166
8.2.1 Signal processing 166
8.2.2 Image reconstruction 167
8.3 Results 168

8.4 Discussion 170

9 CONCLUSIONS **173**

REFERENCES **175**

ACKNOWLEDGMENTS **195**

PART I
Optical techniques for brain function investigation: Physical principles, methodologies, applications

1

Principles and applications of optical techniques in neuroscientific investigations

Functional near-infrared Spectroscopy (fNIRS) and Diffuse Optical Tomography (DOT) are non-invasive optical techniques, which use light in the near-infrared range to infer cerebral activity. Both are gaining popularity all over the world in recent years, thanks to hardware and software developments which have made these techniques more and more used both in clinical and in psychological fields. For instance, a recently published special issue of NeuroImage (Boas et al., 2014) celebrated 20 years of fNIRS research, showing the great progress achieved in the field. In the following paragraphs a brief overview of the history, physical principles, instrumentations and advantages and drawbacks of fNIRS and DOT is presented.

1.1 HISTORICAL NOTES

Optical methods have been used for decades to measure physiological parameters (e.g. pulse-oximetry, used to measure O_2 saturation) and they originated from the muscle oximeter developed by Millikan in the forties (Ferrari and Quaresima, 2012). However, it has been only in the last 30 years that they have started to be used to monitor cerebral activity and physiology. The spread of optical techniques in neuroscience, indeed, was hindered by two main obstacles: the need to find a sensible range of wavelengths able to be absorbed mainly by the molecules of interest and the need to better understand the propagation of light in highly scattering tissues. It was found that the near-infrared wavelength range (600-1000 nm) was the ideal choice, since it was poorly absorbed by biological tissues, but it was instead well absorbed by oxy-hemoglobin (HbO), deoxy-hemoglobin (HbR or reduced-hemoglobin) and cytochrome oxidase, which turn out to be important biological markers. Furthermore, these three chromophores, within this near-infrared range, behave differently, being more or less absorbent depending on the specific wavelength and hence allowing the computation of important physiological parameters. In 1977, Jöbsis (Jöbsis, 1977), who can be considered the founder of in vivo NIRS, was the first to use near-infrared light to non-invasively monitor cerebral hemodynamics in adults. In the following years, studies of light propagation in highly scattering tissues, phantom studies and the development of image reconstruction algorithms allowed imaging in the brain using light to become a reality (Boas et al., 2009).

Near-infrared spectroscopy was first used in the 1980s and 1990s to monitor tissue oxygen saturation in neonates and adults. In 1992 the era of functional magnetic resonance imaging (fMRI) began (Bandettini et al., 1992; Kwong et al., 1992; Ogawa et al., 1992): it provided whole brain images of the blood oxygen level-dependent (BOLD) signal, which was found to be associated with oxygen metabolism and altered blood flow in the brain (Boas et al., 2009). Although fMRI developed very quickly, becoming the predominant imaging technique in neuroscience, it is in-

teresting to observe that fNIRS was born during exactly the same years, with research carried out in different research groups in Japan (Hoshi and Tamura, 1993; Kato et al., 1993), Germany (Villringer et al., 1993) and in the US (Chance et al., 1993). Even if the progress and developments in the optics field were much slower compared to those of fMRI, fNIRS is now becoming more and more common in laboratories all around the world thanks to recent advances both in the hardware and in the signal processing methods. By focusing on applications where it displays advantages compared to fMRI or other neuroimaging techniques, fNIRS is now becoming an established neuroimaging and clinical tool, as confirmed by the more than 200 publications in 2012 alone (Boas et al., 2014).

1.2 Physical principles of fNIRS and DOT

1.2.1 fNIRS and DOT rationale

fNIRS and DOT instrumentations are composed by a certain number of sources (usually laser diodes or light emitting diodes) and a certain number of detectors (photomultiplier tubes or avalanche photo-diodes) both placed on the human scalp non-invasively (Fig. 1.2.1). In order to perform a NIRS acquisition, at least one detector and a pair of co-located sources are needed, creating a so-called channel. The difference in light intensity between the light emitted by a source and the one measured at a nearby detector reflects the changes in the optical properties of the tissue underlying the source-detector pair.

Indeed, even if the way that light interacts with tissues is complicated, due to the inhomogeneity and anisotropy of the different travelled tissues, this interaction can be simplified by taking into account only two phenomena: scattering and absorption. Biological tissues are relatively transparent to light in the near-infrared window, near-infrared light is either absorbed by specific chromophores or scattered and scattering is 100 times more likely than absorption. As a result, near-infrared light is able

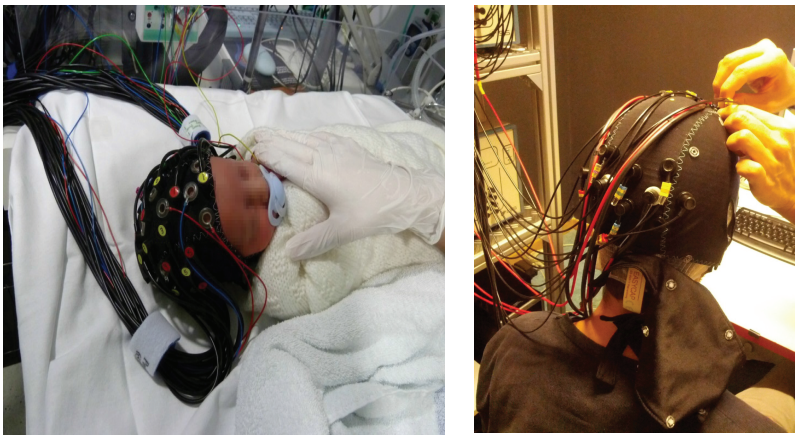

a) b)

Figure 1.2.1: Examples of fNIRS/DOT cap configurations for neonates and adults. a) Courtesy of dr. Rob Cooper, University College London, U.K.. Yellow and red optodes are labeling sources and detectors, respectively. Optical fibers are covered by the black shell and are fastened together. b) Typical fNIRS probe for adults acquisition in the fNIRS lab of the University of Padova. To note, red fibers are labeling detectors positions, while black fibers are the sources.

to penetrate the human head to a depth of several centimeters. Studies on the propagation of light in simplified media (e.g. semi-homogenous medium) allowed the formulation of the so-called 'banana-shaped' path (or Photon Measurement Density Function, PMDF), which constitutes a three-dimensional model of the probability that a photon, leaving a source and being measured at a detector, travels through a given optical path (Fig. 1.2.2). The PMDF allows an accurate assessment of the size of the brain volume sampled by a given source-detector pair. The depth reached by the photons is related to the source-detector distance and it is usually approximately one half of it. Increasing the source-detector distance allows us to probe deeper regions of the brain, at the expense of a Signal to Noise Ratio (SNR) reduction (Calderon-Arnulphi et al., 2009).

Light emitted from a source travels through the scalp, skull, cerebrospinal fluid and reaches the brain. During this path, the main encountered absorbent chromophores for the near-infrared wavelength range are oxy- and deoxy-hemoglobin. As seen in Fig. 1.2.3, where the absorp-

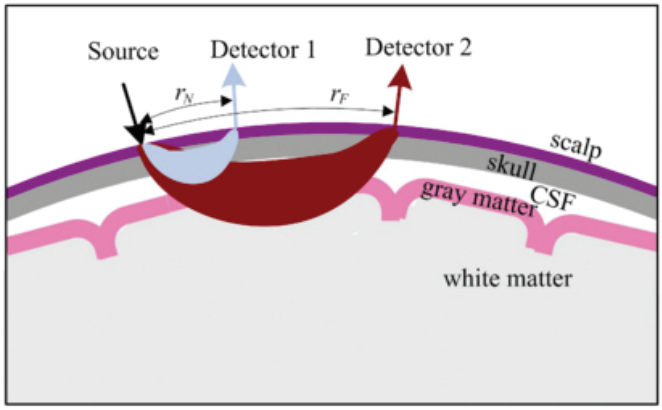

Figure 1.2.2: Banana-shaped path indicating the three-dimensional model of the probability that a photon, leaving a source position (black arrow) and being measured at the detector positions (red and light blue arrows), travels through a given optical path. Source and Detector1 and Source and Detector2 make two different channels. Photons will travel through scalp, skull, cerebrospinal fluid (indicated as CSF in the figure) and grey and white matter. The depth reached by photons is directly proportional to the source-detector distance (taken from Zhang et al. (2012))

tion spectra of HbO and HbR in the near-infrared (NIR) range are displayed. These two molecules absorb light differently depending on the specific wavelength, allowing thus the computation of the absorbance of both of them, depending on the wavelength used. In areas of the brain where a higher hemoglobin concentration is present (e.g. areas where more oxygen is needed), the NIR light will be more heavily absorbed; hence, the detected light will have much lower intensity compared to the emitted one.

Other chromophores also have the ability to absorb the near-infrared light: water, lipids, melanin and cytochrome oxidase. Nevertheless, the absorption spectrum of water has a peak after 900 nm, that is the end of the near-infrared window, while lipids present a very low absorption in this window. Melanin strongly absorbs near-infrared light, however, due to its low concentration, its contribution to absorption of tissue is limited. Cytochrome oxidase is a chromophore of interest: it is an indicator of intracellular metabolism. However, it has a small effect on the total absorption of tissue (at least one order of magnitude lower than the

absorption due to hemoglobin, because its concentration is ~ 1 tenth of that of hemoglobin). Although HbO and HbR are dominant in the NIR window, the absorption due to water, lipids, melanin and cytochrome oxidase can heavily influence the measured signal. However, we can assume their contribution to be constant in time and hence the variations over time in the measured absorption signal can be considered due only to hemoglobin.

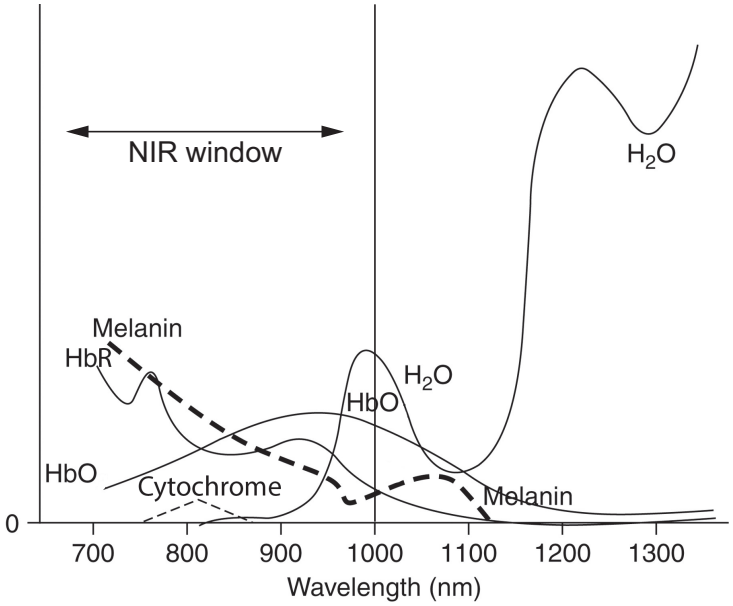

Figure 1.2.3: Absorption spectra of the main absorbers in the NIR wavelength range (600-1000 nm). Note the peak in the water (H_20) absorption spectrum around 1000 nm, at the border of the NIR range. Cytochrome oxidase has a very low absorption spectrum in the NIR window. Melanin (dashed line) greatly absorbs light in the NIR range, however its concentration in tissue is low. To note also the different absorption spectra of HbO and HbR, whose contributions can thus be separated (Figure adapted from Murkin and Arango (2009))

1.2.2 Theoretical formulation

Let's now formulate mathematically the previously description of the way of NIR light interacts with tissue. These mathematical formulas will

make clear how it is possible to compute HbO and HbR concentration changes from measures of intensity of the NIR light.

The Beer-Lambert law describes the ratio between the intensity of light emitted by the source (I_0) and the intensity measured at a detector (I), in the case of non-scattering medium:

$$OD = -\log \frac{I}{I_0} = \mu_a(\lambda) \cdot L \tag{1.1}$$

where OD is the optical density or attenuation, $\mu_a(\lambda)$ is the absorption coefficient of the medium at a particular wavelength (λ) and L is the distance travelled by photons through the medium (optical pathlength). The absorption coefficient can be written as the product of the chromophore concentration (c) and its extinction coefficient (ϵ); thus, equation 1.1 becomes:

$$OD = c \cdot \epsilon(\lambda) \cdot L \tag{1.2}$$

Besides absorption, however, there is another way light can interact with tissues, as we have stated before: scattering, which is actually even more frequent than absorption. Scattering makes the path followed by each photon, between scattering events, random; photons, which are subjected to more scattering events will take longer to exit the tissues and thus will have more probability to be absorbed. To incorporate scattering, the modified Beer-Lambert law (MBLL) has been formulated. It is derived from the solutions of certain photon transport equations under some simplified hypotheses: homogeneous medium, high but constant scattering and homogenous variations of the parameters of interest in the measured volume:

$$OD = c \cdot \epsilon(\lambda) \cdot d \cdot DPF(\lambda) + G(\lambda) \tag{1.3}$$

where G(λ) has been introduced to account for scattering losses and it depends on the measurement geometry and scattering coefficient, d is the real source-detector distance and DPF(λ) is the differential pathlength

factor, which takes into account the increased path followed by the photons due to scattering.

Under the simplified hypothesis of high but constant scattering, the parameters G(λ) and DPF(λ) can be considered constant. Hence, when a change in optical density (ΔOD) is measured, this latter can only be caused by a change in concentration (Δc):

$$\Delta OD = OD_t - OD_{t_0} = \Delta c \cdot \epsilon(\lambda) \cdot d \cdot DPF(\lambda) \tag{1.4}$$

where OD_{t_0} is the attenuation at time t_0 and OD_t the attenuation measured at time t.

As we have previously stated, the main absorber in the near-infrared range is hemoglobin; even if other chromophores absorb light in this range, we can assume constant their contributions. Thus, the variation in attenuation can be considered, at each wavelength, as the linear combination of the contributions of HbO and HbR:

$$\Delta OD(\lambda) = (\Delta[HbO] \cdot \epsilon_{HbO}(\lambda) + \Delta[HbR] \cdot \epsilon_{HbR}(\lambda)) \cdot d \cdot DPF(\lambda) \tag{1.5}$$

where $\epsilon_{HbO}(\lambda)$ and $\epsilon_{HbR}(\lambda)$ are the extinction coefficients of HbO and HbR at a particular wavelength λ, and [HbO] and [HbR] are HbO and HbR concentrations, respectively. Thus, NIRS measurements are usually performed by recording the attenuation changes at two different wavelengths over approximately the same volume of tissue (thanks to the two co-located sources) and, using the MBLL and the known extinction coefficients of HbO and HbR, determining the concentration changes of these chromophores (Boas et al., 2009):

$$\Delta[HbO] = \frac{\epsilon_{HbR}(\lambda_1)\frac{\Delta OD(\lambda_2)}{DPF(\lambda_2)} - \epsilon_{HbR}(\lambda_2)\frac{\Delta OD(\lambda_1)}{DPF(\lambda_1)}}{(\epsilon_{HbR}(\lambda_1) \cdot \epsilon_{HbO}(\lambda_2) - \epsilon_{HbR}(\lambda_2) \cdot \epsilon_{HbO}(\lambda_1)) \cdot d} \tag{1.6}$$

$$\Delta[HbR] = \frac{\epsilon_{HbO}(\lambda_2)\frac{\Delta OD(\lambda_1)}{DPF(\lambda_1)} - \epsilon_{HbO}(\lambda_1)\frac{\Delta OD(\lambda_2)}{DPF(\lambda_2)}}{(\epsilon_{HbR}(\lambda_1) \cdot \epsilon_{HbO}(\lambda_2) - \epsilon_{HbR}(\lambda_2) \cdot \epsilon_{HbO}(\lambda_1)) \cdot d} \tag{1.7}$$

Thus, it emerges how fNIRS and DOT are able to probe the cortical

portion of the brain and to provide measures of concentration changes of oxy- and deoxy-hemoglobin, obtained by the corresponding measured changes in optical absorption.

1.2.3 PHOTON MIGRATION FORWARD PROBLEM

Unfortunately, the simplified hypotheses of the MBLL are not met when probing the human head. For example, the composition of the human head, i.e. skin, skull, brain, is clearly not homogeneous. Thus, the MBLL cannot provide accurate values of concentration changes in the cortex and cannot be used to produce meaningful images. The first step to reconstructing images from optical data is to provide a model of how light diffuses into the given medium, i.e. to solve the so-called photon migration forward problem. A more sophisticated and realistic model for the propagation of photons in the brain is the radiative transport equation (RTE). Unfortunately, the solution of the RTE for a large 3D volume is too computationally expensive. Thus, for optical image reconstruction the diffusion approximation of the RTE is usually used, the so-called diffusion equation, given by:

$$-D \cdot \nabla^2 \phi(r,t) + \nu \cdot \mu_a \cdot \phi(r,t) + \frac{\partial \phi(r,t)}{\partial t} = \nu \cdot S(r,t) \tag{1.8}$$

where $\phi(r,t)$ is the photon fluence at time t and position r, which is proportional to intensity, $S(r,t)$ is the distribution of the sources of photons, ν is the speed of light in the medium, and $D = \nu/(3\mu_s')$ is the photon diffusion coefficient with μ_s' the reduced scattering coefficient. When the scattering coefficient is much greater than the absorption coefficient, the diffusion equation accurately models the migration of light (Boas et al., 2001). However, this assumption can be invalid for example near sources or at tissue boundaries or when light is travelling through tissues with high absorption (for example bleeding regions) and low scattering (for example cerebrospinal fluid). The accuracy of the solution of the photon migration forward problem is essential in order to produce accurate image reconstructions in optical tomography.

Many methods have been proposed in order to deterministically solve the diffusion approximation: the radiosity-diffusion model (Arridge et al., 2000), the transport diffusion model (Bal, 2002), the radiative transfer-diffusion model (Tarvainen et al., 2005), the finite-difference (Pogue et al., 1995), the finite-element method (FEM) (Arridge et al., 1993) and the boundary element method (BEM) (Elisee et al., 2011) and others (Arridge and Schweiger, 1997; Xu et al., 2004).

Another interesting approach to solve the photon migration forward problem is to statistically model the individual photon paths using Monte Carlo (MC) simulations, where a photon probability distribution, after launching a large number of independent random trials, is estimated (Boas et al., 2002). Monte Carlo simulations do not need the same assumptions as the diffusion equation and hence give better solutions to the forward problem when, for example, the diffusion approximation is not valid. However, Monte Carlo approaches are usually computationally more expensive than the numerical models, even if, in recent years, new developments in graphics processors (GPUs) (Fang and Boas, 2009a) and image-based 3D mesh generation software have highly increased their computational speed (Fang, 2010).

1.3 Classes of NIRS and DOT instrumentations available in the market

NIRS/DOT instrumentation can be divided in three main classes, depending on how light is emitted by the sources and how the information is obtained from the detected light: continuous-wave systems (CW), frequency-domain (FD) systems and time-domain (TD) systems (Fig. 1.3.1).

CW systems were the first to be developed: light is emitted continuously and with constant amplitude by the light source and detectors measure changes in the attenuation in amplitude suffered by the light ray when exiting the tissue layer. CW systems are easy to implement, relatively inexpensive and portable and are the most common NIRS systems

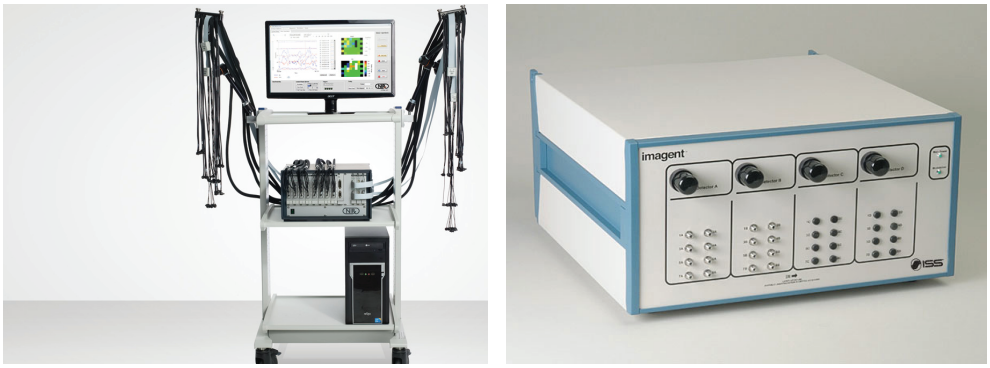

a) b)

Figure 1.3.1: Examples of NIR instrumentations. a) An example of continuos wave optical tomography instrumentation, taken from www.nirx.net. b) An example of frequency-domain fNIRS instrumentation, taken from www.iss.com. Note the different number of sources and detectors available: only 4 in the fNIRS instrumentation and much more in the optical tomography one.

in the world (Scholkmann et al., 2014). Due to their simplicity, however, they can measure only changes of HbO and HbR concentrations with respect to a baseline value, and not absolute values or separate scattering and absorption coefficients (Ferrari and Quaresima, 2012).

FD and TD systems (in ascending order) are more expensive and more complex than CW systems but allow the measurements of more parameters. Indeed, with FD and TD systems it is possible, in certain cases, to measure the absolute optical properties of tissues, i.e. the absorption coefficient and reduced scattering coefficient, and thus the absolute values of HbO and HbR (Ferrari and Quaresima, 2012).

In FD systems light is emitted continuously as in the CW systems, but its amplitude is modulated in frequencies on the order of tens to hundreds of megahertz. From the attenuation in amplitude and the phase shifting between the emitted and detected photons it is possible to obtain information about scattering and absorption coefficients.

TD systems, instead, use short duration (picosecond) pulses of light and detect the temporal distribution of the photons (time of flight or temporal point spread function) after they have travelled through the tissues. The shape of this distribution provides information about the scattering

and absorption of the traversed tissues. Moreover, information about the depth reached by the photons can be extracted from this distribution, which represents a histogram of the time taken by each photon to reach the detector, since it is more likely that a photon measured later by the detector has reached a greater depth (Torricelli et al., 2014).

TD systems tend to have higher depth resolution than FD systems, but lower temporal resolution. Furthermore, TD systems need longer acquisition times in order to obtain a suitable SNR. Nevertheless, TD systems provide more information compared to FD systems: these latter, indeed, allow obtaining information only at certain frequencies of modulation, while the former at all frequencies (Boas et al., 2009). Indeed, the Fourier transform of the point spread function provides information on the amplitude attenuation and phase shifting in a continuous spectrum of frequencies.

These three classes of NIR instrumentations can be utilized in three different types of measurements: spectroscopy (NIRS), topography and tomography (DOT). The differences among these measurements are the number of sources and detectors available, the allowable distance between sources and detectors and whether the system has been designed to create images. NIRS is the simplest measurement type and can be performed with just one source-detector pair, which probes the underlying cortical region. If multiple source-detector pairs are used, multi-channel NIRS can be performed, but the result will still be a series of spectroscopic measurements. If the number of source-detector pairs is increased, using for example a planar array, optical topography can be performed: 2D topographic maps of the concentration changes of HbO and HbR in the underlying areas can be obtained. DOT instruments are composed of an array of sources and detectors, as in the topography case, but placed in order to get 3D images, i.e. non-sparse whole-head coverage and with varying source-detector distances and overlapping measurements in order to probe different depths (Gibson et al., 2005).

1.4 Pros and cons of fNIRS and DOT

fNIRS and DOT are gaining popularity in the clinical and psychological fields due to some great advantages they have compared to other better known and consolidated electrical or functional neuroimaging techniques, such as electroencephalography (EEG) and magnetoencephalography (MEG), which detect the direct electrical activity of the brain (of the order of milliseconds), and Position Emission Tomography (PET), and functional Magnetic Resonance Imaging (fMRI), which are more similar to the optical techniques, measuring the consequences of functional hemodynamic response (of the order of seconds). In the following paragraphs a brief overview of the EEG technique (the most common technique in infant studies) and of the fMRI technique (which can be considered the gold standard of functional neuroimaging) are presented, together with their pros and cons compared to fNIRS and DOT.

1.4.1 Comparison with EEG

EEG is probably the most common neuroimaging technique in biomedical fields. This technique measures at the skin level the changes in electrical potentials coming primarily from the superficial cortical layer of the brain. Specific electrical patterns can emerge from the measured electrical activity during specific tasks or conditions. When more electrodes are used to record the electrical activity, a topographical image can be reconstructed, which represents the spatial distribution of the electrical activity.

Billions of neurons are present in the brain, and each of them is polarized at rest; neurons communicate with each other through the depolarization of the cell membrane. Unfortunately, the depolarization of a single neuron is not detectable at the skin level. Hence, what EEG is measuring is the summation of electric fields created by thousands of neurons, which fire synchronously, in a given volume of tissue. Coupled with the smearing effect of the semi-conducting skull, the result is that

the spatial resolution of EEG is low and it is very difficult to precisely link the measured electrical signal at the skin level to the area of the cortex from which it originates. On the other hand, the temporal resolution of EEG is very high: measurements can be obtained with sample rates in the KHz range (Niedermeyer and da Silva, 2005; Purves et al., 2007).

A very important application of EEG is the study of event related potentials (ERP): they are useful, for example, to localize functional deficit in neurological patients and to describe the temporal course of cognitive processing. Usually the person under examination is stimulated with an acoustic, visual or tactile stimulus and the electrical potential generated by this stimulation is recorded and recovered by block averaging the parts of the signal following each stimulus. They provide an accurate temporal description of the induced cerebral activity (Handy, 2005; Luck, 2005).

EEG and fNIRS/DOT share the same experimental requirements, allowing a painless and non-invasive measurement of cerebral activity. The spatial resolution of EEG ($\sim$ cm) is worse than that of the NIR techniques, while its temporal resolution ($\sim$ ms) is better. This means that, while with EEG a spatial localization of the measured activity at the level of the lobes can be performed, with optical techniques it is possible to localize the brain response to specific cortical areas. The great advantage of the NIR techniques compared to EEG is that the optical signal is less susceptible to motion artifact corruption, making optical techniques particularly suitable for babies and challenging populations (i.e. stroke patients), which by definition, will not be able to stay still for the entire duration of the acquisition (Lloyd-Fox et al., 2010).

1.4.2 Comparison with fMRI

fMRI is a non-invasive technique, which uses magnetic fields to image the functional activity of the brain. We refer the reader to Brown and Semelka (2010) and Purves et al. (2007) for a comprehensive description of its physical principles. Briefly, when the human body is placed in a

strong magnetic field, all protons (hydrogen atoms) present in the body (~ 65% of the human body is made up of water) will orient themselves to be parallel or antiparallel to the direction of the magnetic field. Spins under a magnetic field continue precessing about the magnetic field direction at a constant rate. When a brief radio-frequency magnetic field pulse with the resonant frequency of the rotating protons is applied, these protons can change energy state. This causes the magnetization vector M to rotate away from its equilibrium orientation. When the radio-frequency magnetic pulse is terminated, protons tend to release the absorbed energy as a radio-frequency electromagnetic wave, which is measurable. This process is called relaxation and it is time dependent.

The fMRI technique is based on T2* relaxation, which is the time required for the perpendicular components of M to decay to 37% of its initial value. Oxy-hemoglobin is diamagnetic, with a small magnetic moment, while deoxy-hemoglobin is paramagnetic, and has a large magnetic moment. Large concentrations of deoxy-hemoglobin cause a reduction in the T2* relaxation time of the tissue, resulting in a decrease of the measured signal. Under sensory stimulation, the activated brain areas undergo an increase in blood flow, and consequently in delivered oxygenated hemoglobin. Deoxygenated hemoglobin concentration instead decreases, and, as a consequence, the T2* relaxation time for the stimulated tissue increases compared to the non-stimulated tissue. This phenomenon is called the Blood Oxygen Level-Dependent (BOLD) effect (Brown and Semelka, 2010). Hence, fMRI is based on the BOLD signal, which depends on the balance between the consumption and supply of oxygen in the activated cerebral area.

fMRI and optical techniques are both non-invasive and share the same measured signal, both recovering the hemodynamic response. Nevertheless, while fMRI is able to measure only the BOLD signal (i.e. a function of the deoxy-hemoglobin contribution), optical techniques are able to measure both oxy- and deoxy-hemoglobin contributions separately. The spatial resolution of fMRI (2-3 mm) is higher than that of NIR techniques (~cm), even if in recent years, with new hardware developments, high-

density DOT acquisitions have reached a spatial resolution comparable to that of fMRI (Eggebrecht et al., 2012; Zhan et al., 2012). The temporal resolution of fMRI is instead lower than that of optical techniques. fMRI is very sensitive to motion artifacts: thus, it requires the participant to lay still, inside a closed and noisy scanner for the entire duration of the acquisition. On the contrary, optical techniques are silent, creating not only a more relaxed experimental environment, but also allowing a clear presentation of, for example, auditory stimuli (Lloyd-Fox et al., 2010). Moreover, fMRI facilities are cumbersome and expensive and prevent easy access and transportation. It is clear how fMRI is unsuitable in awake babies and children, patients suffering from particular pathologies (e.g. schizophrenia, Parkinson disease) which limit their motor control, or those with metallic prosthesis or pacemakers.

1.4.3 Other general advantages and drawbacks of fNIRS/DOT

As it emerges from the previous paragraphs, EEG and fMRI are limited by intrinsically unavoidable disadvantages. Optical techniques, instead, seem able to overcome some of these drawbacks. Their instrumentation is inexpensive and portable, and the measured signal is less sensitive to motion artifacts, enabling the participant to sit upright and be less restricted than with the other techniques. In recent years, new wireless optical devices have been proposed (Muehlemann et al., 2008), which are even less sensitive to motion artifacts and allow a higher freedom of movement. There are several scenarios where wireless NIR techniques can improve the quality of the acquired information: monitoring children, epileptic patients and patients during motor rehabilitation training are only a few examples. NIR techniques are also ideal for clinical monitoring, since they do not interfere with other instruments and can be performed at the bedside, without the need to move the patients elsewhere. This is an important feature when considering patients located in the intensive care unit, for example (Calderon-Arnulphi et al., 2009).

This lack of interference makes optical techniques ideal for multi-modal approaches. Several studies have been presented where EEG (Cooper et al., 2011; Wallois et al., 2010, 2012) or MRI (Cooper et al., 2012a; Erdoan et al., 2013; Gagnon et al., 2012b; Yuan and Ye, 2013; Yücel et al., 2012) and optical techniques have been used in combination. The simultaneous measurement of cerebral activation with different modalities allows a better insight in the studied phenomenon. Combination with the MRI technique, furthermore, makes it possible to couple the functional information obtained with optical techniques with anatomical information measured with MRI, allowing a more precise localization of the activated brain areas. Indeed, one of the limitations of optical techniques is their inability to provide structural information.

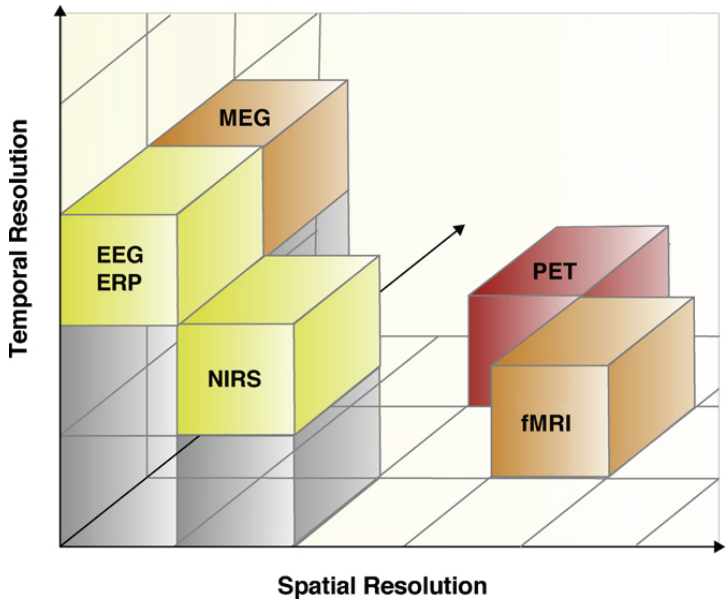

Figure 1.4.1: Comparison of spatial and temporal resolutions between fNIRS and other neuroimaging modalities. EEG/ERP and MEG are characterized by a good temporal resolution, while fMRI and PET have the best spatial resolution. Optical techniques are in the middle of the diagram, showing both a good temporal and spatial resolution (adapted from Lloyd-Fox et al. (2010)).

The temporal resolution of optical techniques depends on the available instrumentation: it is better than that of fMRI and worse than that

of EEG, with a typical sample time on the order of 100 milliseconds. The spatial resolution is on the order of the centimeters, better than that of EEG but worse than fMRI. An overview of the spatial and temporal resolution properties of the main neuroimaging techniques is presented in Fig. 1.4.1. Optical techniques are located in the middle of the diagram, exhibiting both a good spatial and temporal resolution. A limiting factor of the optical techniques is depth resolution, which is dependent on the optical properties of the tissues and the source-detector distance. Usually, particularly in adults, only the cortex can be probed. This prevents optical techniques from gathering information about deeper regions of the brain, which can be monitored using fMRI (Lloyd-Fox et al., 2010).

Another drawback of NIR techniques is that the signal to noise ratio is variable. Indeed, it can change depending on the thickness of the skull (increasing the thickness increases the pathlength to the brain and increases the absorption of light) and on the color of the hair and skin (black hair or skin reduce the amount of light penetrating the brain compared to light colored hair and white skin). Hence, the quality of NIR measurements is dependent on the features of the participant under examination (Calderon-Arnulphi et al., 2009).

1.5 Conclusive remarks

Optical techniques are very promising in the clinical and neuroscientific fields. They exhibit some remarkable advantages compared to other neuroimaging techniques and, with a non-invasive measurement, can monitor brain activity by measuring hemoglobin concentration changes. Nevertheless, there are still some methodological problems inherent to the measured signal, which have hindered the uptake of fNIRS and DOT in many fields.

2

fNIRS and DOT: State of the art on modeling methodologies, open issues and aims of the thesis

2.1 Features of fNIRS and DOT measured signal

As previously stated, fNIRS and DOT measures are performed with a varying number of sources and detectors placed non-invasively on the human scalp. Sources and detectors may be placed at different distances between each other and their distance is directly proportional to the depth reached by photons, i.e. short source-detector distances ($<$ 1 cm) will probe only the skin and skull, source-detector distances of ~3 cm will probe the cortex and distances $>$ 4 cm will probe deeper regions of the brain, but at the expense of a signal to noise ratio reduction. In the present section the origin and components of the measured optical signal will be

presented, highlighting the difference between the signal measured at standard channels (source-detector distance ~3 cm) and that measured at short-separation channels (source-detector distance < 1 cm). The main algorithms used to filter the optical signal in order to correctly estimate the brain response will also be presented, and their pros and cons highlighted.

2.1.1 The hemodynamic response

Optical techniques measure the concentration changes of HbO and HbR: hence, they are usually applied in experiments where a change in their concentration is invoked by the presentation of stimuli. Neuroscientists are interested in localizing where in the brain and how the response to a particular task develops: the performance of the cognitive task causes an increase in the electro-chemical activity of those neurons dedicated to the task, which increase their energy-consumption. In brief, neurons start firing in a repetitive way and each time they fire, they need to repolarize their cell membranes back to the resting potential. This process requires ATP (adenosine-tri-phosphate), an energy-rich molecule, which is the basis of almost all cellular processes, in order to actively transport charged ions through the membrane. ATP is produced by a process known as cellular respiration, which requires glucose and (usually) oxygen. When neurons fire continuously, the demand of glucose and oxygen increases, because more ATP has to be produced. This metabolic demand is met by the nearby vasculature: capillaries dilate and consequently cerebral blood flow (CBF) in the needed brain area increases. This interaction between the neural and vascular systems is known as neurovascular coupling and this process is at the heart of many functional neuroimaging methods, including optical techniques and fMRI (Buxton, 2002; Shulman and Rothman, 2004).

The increase in CBF and the rate at which oxygen is consumed are not balanced. The oxygen provided by the local increase in CBF is much greater than the consumption of oxygen and this leads to an increase in

the concentration of HbO and a decrease in the concentration of HbR. When the stimulation is terminated, and neurons come back to their previous metabolic rate, CBF decreases and the concentration of HbO and HbR return to their baseline values. These concentration changes can be measured with optical methods and are the bases of functional brain activation mapping and are referred to as the hemodynamic response (HR). The classical hemodynamic response measured with optical techniques therefore consists of an increase in oxy-hemoglobin and a smaller and later decrease in deoxy-hemoglobin, as displayed in Fig. 2.1.1. This response is quite slow compared to the neural response, usually reaching a peak in 3-5 seconds, but the duration, shape and peak latency are dependent on the type of stimulation, duration of the stimulation, brain areas involved and age of the participant.

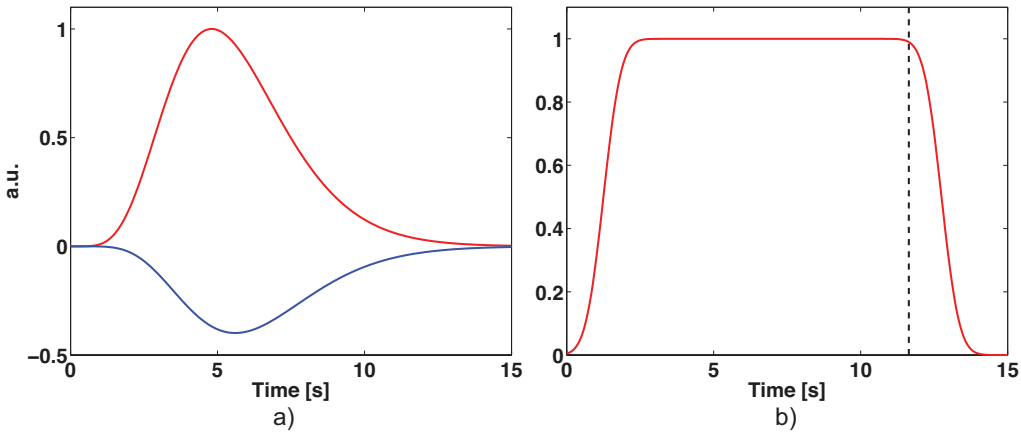

Figure 2.1.1: Examples of hemodynamic responses for a) an event-related design and for b) a block-design. In red oxy-hemoglobin, in blue deoxy-hemoglobin. In the event-related design, considering the presentation of a single stimulus at time 0, the HbO hemodynamic response increases after the presentation of the stimulus, reaching a peak around 4-5 seconds and decreasing after that. Deoxy-hemoglobin instead has an opposite behavior with a small delay in the presentation of the peak. In block designs, instead, the shape of the HR is different, with an increase in HbO after the presentation of the first stimulus at time 0 and then a plateaux phase lasting the entire duration of the stimulation. The dashed line represents the end of the train of stimuli presented.

The hemodynamic response is usually very small, in the order of 100

nanoMolar for event related design, where the response to each single stimulus is measured, and of microMolar for a block design, where the total response after a train of stimuli is measured. In block design usually the concentration changes of oxy-hemoglobin increase until they reach a plateau; indeed, the increase in CBF does not increase endlessly, but only up to a certain value, then remaining approximately constant until the end of the stimulation (Fig. 2.1.1). The frequency of the hemodynamic response depends on the paradigm used, but it is usually around 0.1 Hz.

The actual raw optical measured signal contains a number of physiological components and presents a higher amplitude than the HR (usually $>$ 2000 nM). The HR is therefore not visible in the raw data (Fig. 2.1.2). Recovering the hemodynamic response from the physiological background as well as possible is essential for a correct interpretation of the results.

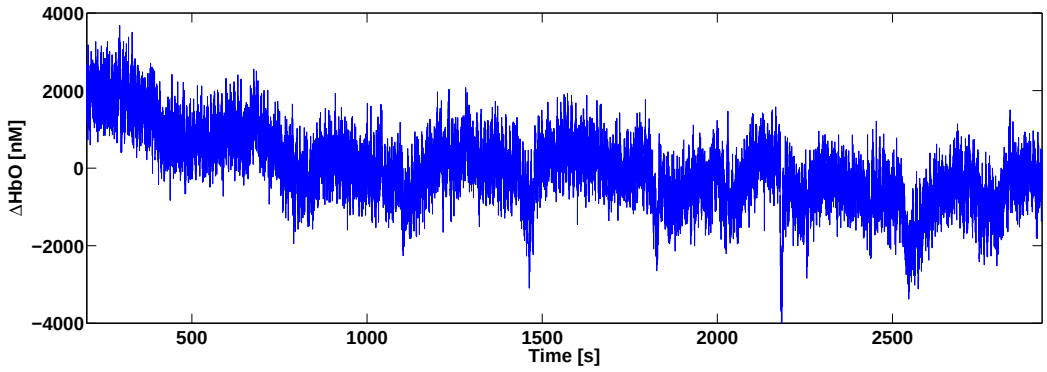

Figure 2.1.2: Example of NIRS measured signal for a representative channel. Note the high amplitude of the signal relatively to the expected HR amplitude.

2.1.2 Noise and physiological noise components

Besides the hemodynamic response, the optical measured signal contains many other components, which can be considered noise, since they hamper an easy recovery of the hemodynamic response. These components can be divided into three categories: measurement noise, motion artifacts and physiological noise.

Measurement noise is always present in every acquisition and has a random evolution. A way to reduce environmental noise is to perform acquisitions in a dimly lit room, so that the light measured at the detector positions is only that coming from the near-infrared sources.

Although the improvement in optical technology has been significant in recent years, effectively coupling the sources and the detectors to the head can be problematic and motion artifacts are often a significant component of the measured optical signal. Indeed, every movement of the head causes a decoupling between the source/detector fiber and the scalp, which is reflected in the measured signal, usually as a high-frequency spike and a shift from the baseline intensity (see Fig. 2.1.3 for an example). In order to properly estimate the hemodynamic response, motion artifacts should be detected and removed. Motion artifacts will be dealt with more thoroughly in chapter 4, where several motion correction techniques will be presented and compared.

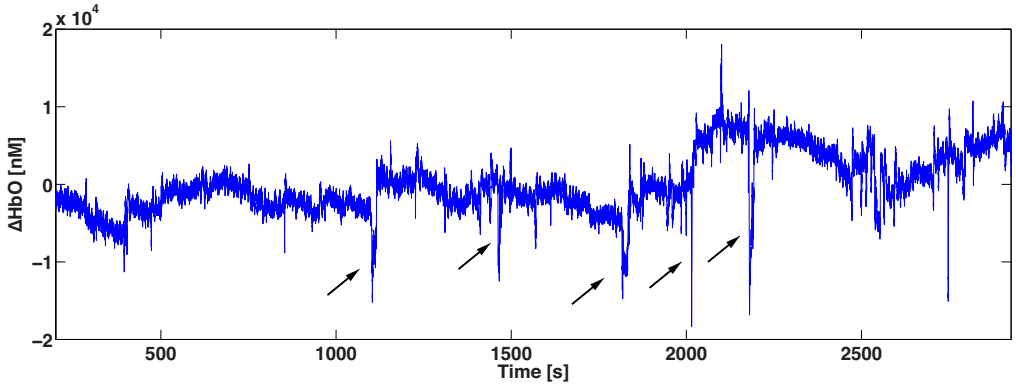

Figure 2.1.3: Example of motion artifacts present in a representative optical signal due to sudden subject's movement. Motion artifacts are indicated by arrows. They are usually high-frequency spikes occurring suddenly in the time-series.

Physiological noise can be further distinguished into four components: heart beat, respiration, low-frequency oscillations (or vasomotor waves or Mayer's waves) and very low frequency oscillations. The cardiac pulsation has a frequency around 1 Hz in adults and can be represented by a pseudo-constant sinusoidal wave, easily visible in the raw optical data.

Thanks to the difference in frequency compared to the hemodynamic response, the hearth beat can easily be removed from the measured signal by applying a low-pass filter. The respiratory oscillation has a frequency around 0.2 Hz, and can be modeled as well with a sinusoidal wave. It is usually removed by temporal means, assuming the stimulus is not synched to the respiration cycle. Very-low frequency oscillations have a frequency lower than 0.1 Hz and usually appear as particular trends, constant, decreasing or increasing and may be easily removed with a high-pass filter with a very low frequency cut-off.

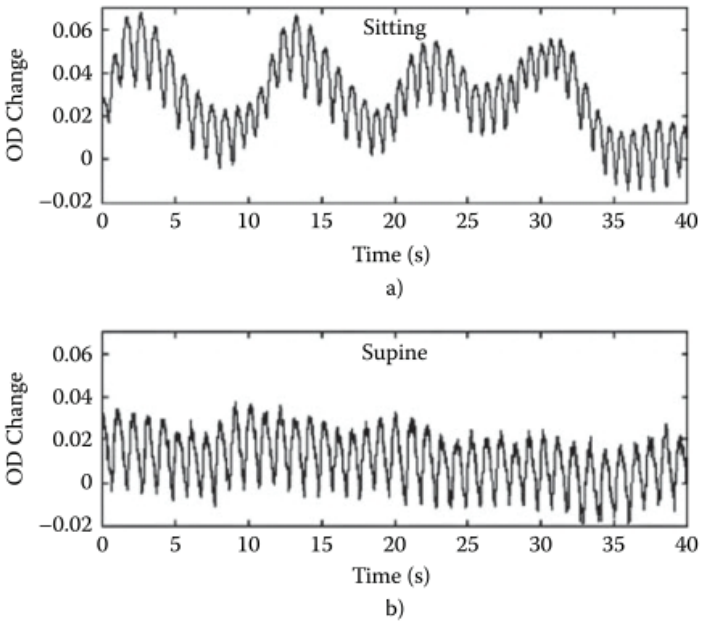

Figure 2.1.4: Examples of NIRS time series (ΔOD) acquired with the participant a) in a sitting position and b) in a supine position. Note the presence of a slow oscillation, with a frequency ~0.1 Hz only when the participant is in a sitting position. This oscillation is the Mayer's wave. Clearly visible also the cardiac pulsation in both time-series (taken from (Boas et al., 2009)).

The vasomotor wave, or Mayer's wave, can be considered the most problematic physiological component, because it has a frequency similar to that of the hemodynamic response (0.04-0.15 Hz) and its amplitude is usually higher than that of the HR. Thus, it cannot be removed with a

normal filtering method (Boas et al., 2004). The exact origins of Mayer's wave are still controversial; it is believed it is linked to oscillations in systemic blood pressure. A hypothesis is that it is generated by oscillations in the vascular tone, not correlated with cardiac or respiratory fluctuations but caused by local changes in the contraction of smooth muscles present in the vascular wall (Lloyd-Fox et al., 2010). The vasomotor wave has been extensively studied (Julien, 2006) and it has been demonstrated that it is more prominent when the person is sitting than when lying down (see Fig. 2.1.4). This is the reason why Mayer's waves are not a major confounding component in fMRI experiments, as it can be in optical studies (Boas et al., 2009).

The optical signal is contaminated not only by physiological oscillations coming from the cerebral compartment, but also from those originating in the superficial layer, i.e. skin, scalp and the pial vasculature layer, located above the surface of the cortex (Dehaes et al., 2011; Elwell et al., 1999; Gagnon et al., 2012b; Kirilina et al., 2012). Furthermore, while in the cerebral compartment blood flow is subject to autoregulation, skin blood flow is more strongly affected by systemic physiological oscillations. This leads physiological noise to account for more than 10% of the measured optical signal change, while brain activation contribution is usually much smaller than 5% (Boas et al., 2004). Skin blood flow also plays an important role in the regulations of many functions (e.g. body temperature, fight-and-flight response, emotions), which can be altered during experimental paradigms. Since these evoked physiological changes tend to be time-locked to the stimulus, they can produce false positive activations (Kirilina et al., 2012; Tachtsidis et al., 2009).

All these studies and reasons highlight the importance of removing physiological noise components from the superficial layers of the head from the measured optical signal in order to correctly estimate the hemodynamic response and interpret unbiased activation results.

2.2 State of the art of algorithms for physiological noise removal: The potentials of short-separation channels

As previously stated, there are two different types of channels, which can be present during an acquisition: standard channels and short-separation (SS) channels (Fig. 2.2.1). Standard channels have a source-detector distance, which allow them to probe the cortex. In adults' studies, this distance is around 2-4 cm, while in infant studies it can be shorter, around 1.5-4 cm. The optical signal recorded by standard channels contains all the components previously described, i.e. the cortical hemodynamic response, measurement noise, motion artifacts and physiological noise. Note that it includes also physiological noise originating in the scalp layer, because light is passing through the scalp to reach the cortex. Short separation channels, instead, have a source-detector distance < 1 cm, usually around 0.7-0.8 cm. This short distance prevents the light from reaching the cortex and hence, the optical signal measured in these channels will not contain signal coming from the cerebral cortex. Instead, the signal measured in these channels includes only measurement noise, motion artifacts and physiological noise originating in the scalp layer, but not the hemodynamic response.

As highlighted in paragraph 2.1.2, in order to correctly estimate the hemodynamic response, it is important to get rid of physiological noise contamination. Thus, in this context it is clear the importance of the short-separation channels. Since the signal at standard channels and at short separation channels is measured simultaneously and at nearly the same location, it can be supposed that the physiological noise measured at the two channels will be the same (Fig. 2.2.1). This is the reason why short-separation channels are also called reference channels. Physiological noise recorded at short-separation channels can be regressed from the signal measured at standard channels, thus removing most of the physiological noise contamination without affecting the hemodynamic

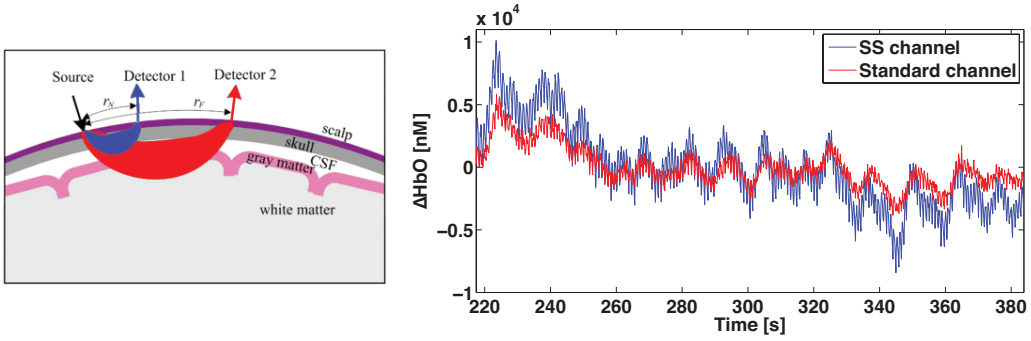

Figure 2.2.1: Short-separation (SS) channel and standard channel. a) Schematic representation of SS (in blue, Source and Detector1) and standard (red, Source and Detector2) channels. Note the different probing regions of the head of the two channels (adapted from Zhang et al. (2012)). b) Examples of measured optical signals from a SS channel (blue) and a standard channel (red). Physiological noise oscillations in the two channels are highly correlated, thus corroborating the idea of regressing SS channel signal from standard channels in order to reduce physiological noise contamination.

response.

Since physiological noise removal has been a major problem in optical measurements for many years, many algorithms have been proposed in order to remove this difficult component from the optical measured signal, even before the discovery of the properties of SS channels. Some of these methods are briefly described in the following paragraphs. Despite their importance, most of these techniques are yet to become standard in optical signal-processing.

2.2.1 Frequency filtering

One of the first attempts to try to remove physiological noise was the application of a frequency filter to the measured standard channel signal. For instance, a band-pass filter can be applied, which will remove all frequency components present in the signal with a frequency higher than that of the higher filter cut-off and lower than that of the lower filter cut-off. This method has been employed by Jasdzewski et al. (2003) and they used cut-off frequencies of 1/30 Hz and 1 Hz. Franceschini et al. (2003),

instead, band-passed filter the data between 0.02 and 0.5 Hz.

Band-pass filtering has been widely used in the literature, because it is very easy and straightforward to apply. It is very effective in removing the cardiac component, which has a frequency around 1 Hz in adults, and the very low frequency oscillations, i.e. drifts. Unfortunately, band-pass filters cannot remove physiological oscillations such as respiration or Mayer's wave, due to the overlap in the frequency spectrum between these fluctuations and the hemodynamic response. Using excessively restrictive cut-off frequencies will result in the removal of both physiological oscillations and hemodynamic response itself, while applying too relaxed cut-offs will result in the maintenance of the brain response but in the failure of physiological noise removal. Hence, band-pass filtering could be considered a good pre-processing step in the optical signal-processing pipeline, in order to remove cardiac pulsation and very slowly drift, but it has to be followed by a further step to reduce low frequency oscillations.

2.2.2 Subtraction of a non-activated channel

In order to build on the performance of the band-pass filtering method, Franceschini et al. (2003) proposed subtracting a signal measured at a standard channel located far from the activated brain area from the standard channel signal measured in the brain area expected to be activated by the task. The distant signal was considered to be composed of physiological noise only and this noise was hypothesized to be homogeneous in the whole probed area. Unfortunately, these assumptions are not always met. Indeed, in many tasks there are many active brain areas and it could be difficult to select a channel located exactly on a brain area that remains inactive. Also the hypothesis of spatial homogeneity of the physiological noise has been demonstrated to be invalid (Gagnon et al., 2012a).

2.2.3 Principal Component Analysis (PCA)

The idea of exploiting Principal component analysis (PCA) to reduce physiological noise was proposed by Zhang et al. (2005b) and was subsequently applied by Franceschini et al. (2006).

PCA is a multi-channel technique, which applies an orthogonal transformation to the original data set composed of N signals to produce N uncorrelated components. The order of these components is related to the variance of the original data which the component accounts for. Thus, the first PCA component will account for the largest proportion of the variance of the data. The hypothesis on which this method is based is that the physiological noise subspace and the evoked activation subspace are orthogonal. Indeed, physiological noise is present in all channels, and thus more spatially global than the usually localized hemodynamic response, is often much larger in amplitude than hemodynamic responses and accounts for a much larger percentage of the measured signal: thus, it should constitute a large proportion of the variance of the data. Hence, it is supposed that the first M PCA components will represent the variance caused by physiological noise. Thus, removing the first M components from the signal before performing an inverse PCA transform should correct for physiological noise.

The idea is to estimate the physiological noise subspace from baseline data (i.e. without stimulus presentation) and use this to attenuate the physiological components present in activation (i.e. with stimulus presentation) data. Indeed, physiological oscillations may be time-locked with the timing of stimulus presentation and, in this case, it would be difficult to separate the physiological noise and activation subspaces. The assumption is that baseline data should contain the same physiological oscillations as the activation data, and that without activation, the estimation of the physiological noise subspace should be easier. Zhang et al. (2005b), indeed, demonstrated that when estimating the physiological noise subspace from activation data, the first principal component explains a greater variance of the data compared to when this subspace is

computed from baseline data. This means that, in activation data, physiological oscillations and hemodynamic response are coupled and the first component is accounting for both of them.

PCA is very easy to implement and use, even if it requires a subjective choice of the number of principal components to be removed. The standard approach consists in choosing the percentage of the variance to be removed (e.g. 80% of the total variance) and the number of components to be removed can be automatically computed (Franceschini et al., 2006). However, the assumption of orthogonality between the physiological noise and activation subspaces is not always met and the requirement of baseline data implies an increase in the time of acquisition, which is not always possible, particularly when studying infants and pathological populations.

2.2.4 General Linear Model (GLM)

A General Linear Model (GLM) is the standard technique for the analysis of fMRI data. The hypothesis on which it is based is that hemodynamic changes are linearly additive, that is the signal is made up by the sum of all physiological noise oscillations and the HR. However, fMRI and optical data differs by two main aspects: optical data are contaminated by physiological noise on a wider frequency range than fMRI data and optical data can discern between HbO and HbR, thus there is the need to recover two different hemodynamic responses. Hence, the GLM used in standard fMRI analysis has to be modified in order to be applied to optical data.

Cohen-Adad et al. (2007) proposed an improved version of the general linear model, which removes physiological noise contamination and detects the hemodynamic response. The idea is to model both the hemodynamic response and physiological oscillations inside the GLM using a Bayesian framework in order to give some a priori information to the model. Thus, a large set of drift functions is used as regressor parameters in the GLM to account for physiological oscillations. Those that have

high correlation with the stimulation paradigm are then discarded. This leads to a better estimation of the parameters related to activation. Moreover, the authors proposed to detect the presence of activation by running multiple GLMs, instead of only one. Adding a resting state period before and after the task period, there is the possibility to move the measured signal away from the stimulus-modeled signal and to run the GLM at each moving step. The estimated weights for the hemodynamic response in the GLM should be maxima when there is the greatest synchrony between the measured signal and the protocol. The authors proposed also a method to recover the shape of the hemodynamic response. However, in order to achieve this, they needed to include strong priors for HbO and HbR in the model. One drawback of this approach is indeed the need to give a prior parametric model of HbO and HbR; indeed, they can vary from task to task and from brain area to brain area, and it is thus difficult to give a precise model for these chromophores.

Abdelnour and Huppert (2009), instead, proposed an adaptive (i.e. time-varying) version of the canonical GLM in order to estimate the hemodynamic response in real time trial by trial. They modeled the hemodynamic response as a sum of gamma-variant functions and the physiological noise oscillations as a linear combination of sinusoids at specific frequencies (e.g. 0.1 Hz for Mayer's wave and so on). The innovation of this approach is to assume that the phase and amplitude of these sinusoids are adaptive, and hence time-varying. This means that these parameters have to be estimated at each time step and to do so the authors used an extended Kalman filter. For a more detailed description of the Kalman filter approach, see paragraph 2.2.6. The great advantage of the adaptive GLM approach is the possibility of recovering brain activity on a single-trial basis. Moreover, compared to the canonical GLM, such as the one proposed by Cohen-Adad et al. (2007), it utilizes the given initial model for the HR only as a prior, modifying it later according to the encountered data. This also holds true for the physiological noise model. Nevertheless, the priors have to be provided and this is a drawback, because their model has to be hypothesized. Moreover, the prior models

used for HbO and HbR are derived from the BOLD model used in fMRI studies. While the HbR HR measured with NIRS has been found to have a similar shape to the BOLD response, the HbO HR measured with NIRS has a different shape compared to the BOLD response, since it measures a different process. Hence, the prior given for the HbO HR is clearly not valid. This time-varying version of the GLM is clearly more realistic than the canonical version, since both hemodynamic responses and physiological fluctuations are never constant over long periods of acquisition. However, in order to perform these time-varying estimations, the filter needs to start with good initial parameters and thus requires some initial training, which further increases the time of the acquisition.

Other groups have tried to improve the standard GLM in order to more accurately estimate the hemodynamic response from optical data: Ciftçi et al. (2008) proposed a constrained GLM approach, which avoids unrealistic hemodynamic response estimation; Ye et al. (2009), instead, created a new statistical toolbox (NIRS-SPM), which tries to emulate the more famous SPM toolbox for fMRI data analysis, and uses the GLM to statistically analyze NIRS data; Kamran and Hong (2013) presented a new linear parameter varying method and adaptive signal processing. Nevertheless, the drawbacks highlighted before still persist with these new approaches.

2.2.5 Wavelet filtering

The wavelet transform is a powerful approach that provides time-frequency representations of the transformed signal. Lina et al. (2008) proposed to apply continuous wavelet transforms to the optical signal to help separate the physiological noise from the hemodynamic response. Wavelet transformation produces a complex representation of the signal, which can be further synthesized; however, this synthesized representation will not reproduce exactly the original signal, because of the presence of vanishing moments of the wavelet: polynomial content up to a certain degree is filtered out, thus removing slow drifts. Furthermore, the au-

thors proposed a synchrony-based approach, which tries to isolate the presence of the hemodynamic response, independently from its amplitude, using the phase wavelet coefficients and computing the synchrony between constituents of the signal at each epoch and the timing of the stimulus. Despite this approach being shown to be successful in block-design paradigms, its application to randomized event-related designs is more challenging. Indeed, in this case, there is a chance that physiological oscillations and hemodynamic responses are overlapping and contain the same frequency content, they are therefore inseparable using a time-frequency approach.

Researchers from the same group (Lina et al., 2010), then, proposed to use the discrete wavelet transform and a deconvolution approach to recover the whole temporal shape of the hemodynamic response, and not just its amplitude. The regression was performed in the wavelet domain, while the estimation of the hemodynamic response was performed in the temporal domain. The PCA approach proposed by Zhang et al. (2005b) was modified and applied in the wavelet domain, instead of the temporal domain, to remove physiological noise. However, the residual signal contains correlated noise, which wavelet can successfully decorrelate to improve the estimation of the HR. Deconvolution is performed using wavelet coefficients and priors based on the temporal shape of the hemodynamic response.

Jang et al. (2009), instead, introduced the wavelet minimum description length (MDL) detrending algorithm. Here, the wavelet transform is applied to decompose the optical signal into hemodynamic response, physiological noise and other noise components. The wavelet transform of the physiological noise can then be incorporated into a GLM approach; the number of coefficients to incorporate is computed using the minimum description length principle, which, for optical signal data, gives the lowest over-fitting probability.

The wavelet approach may be very powerful but it is usually challenging to implement and not computationally efficient. It requires the user to provide inputs, for example, which wavelet family to use. Furthermore,

when physiological noise and hemodynamic responses are overlapping both in the frequency domain and in the temporal one, this approach is not able to differentiate the brain response from the physiological oscillations.

2.2.6 Short-separation channel regression

In 2005, Saager and Berger (2005) proposed the use of short-separation channels, located in the activated area near standard channels, which are sensitive only to superficial noise contamination, to regress physiological noise from standard channels. Physiological noise was reduced in standard channels by performing a least-square fit of the short-separation channel signal to the standard channel signal and then subtracting the result from the standard channel signal. The same authors, in a later study (Saager and Berger, 2008), confirmed that physiological noise present in the scalp can significantly contribute to optical measures. Indeed, using the method previously described to reduce physiological noise, they showed that, on average, 60% of the hemoglobin changes are removed after the subtraction of the short-separation channel signal from the standard channels signal. Furthermore, they demonstrated that the hemodynamics of the brain and the scalp can be modeled with a homogeneous two-layer model, justifying again the idea of subtracting the signal measured at short-separation channels from the one measured at standard channels. The approach proposed by Saager and Berger (2008) is very easy to implement and launched a number of approaches that use short-separation channels.

However, this approach can lead to a subtraction of a part of the brain signal. When fitting with the least square method the short-separation channel signal to the standard channel signal, there is a chance that some brain activity is removed if physiological noise and hemodynamic responses are synchronous. Hence, when subtracted the computed signal from the standard channel signal, part of the hemodynamic response could be removed as well.

Zhang et al. (2007a,b, 2009) refined the approach proposed by Saager and Berger (2008) in order to consider the non-stationary behavior of the physiological oscillations. They used an adaptive filter with a Finite Impulse Response (FIR) to remove physiological oscillations. The standard channel signal was used as the target measurement, with the signal measured at a short-separation channel used as a reference measurement. The filter converted the physiological noise acquired at the short-separation channel to provide an estimate of the physiological oscillations present in the standard channel and then subtracted this estimate. The coefficients of the filter were updated via the Widrow-Hoff least mean square algorithm on a step-by-step basis, to account for variations of the physiological oscillations during the acquisition. The adaptive filter needed a pre-training session to get a good initial estimate of the filter coefficients. Importantly, the authors also demonstrated that there is a great improvement in regressing the short-separation channel only when the short-separation channel signal and standard channel signal are highly correlated. This finding highlights the importance of the selection of which short-separation channel to utilize in the regression. The adaptive filtering approach is very promising, however the problems described before when using a least-square fitting approach are still present.

Gregg et al. (2010), inspired by the approach by Saager and Berger (2008), showed the feasibility of using short-separation channel regression methods to reduce physiological noise in DOT measures. In DOT, the number of channels with varying source-detector distance is bigger than in fNIRS measures, where a sparse array is usually used. In DOT acquisitions, the information coming from both the brain and the superficial scalp layer is greatly increased and should be fully utilized to better recover the brain response. Instead of regressing one short-separation channel from the standard channel signal, an average of all short-separation channel signals is performed and then regressed from all standard channel signals. If this choice could seem counterintuitive, based on the evidence that physiological noise is not homogeneous (Gagnon et al.,

2012a), it is however necessary, because of the geometric constraints imposed by the imaging array. In fact, in the study by Gregg et al. (2010), the source-detector distances for short-separation channels is greater than usual (14 mm) and this results in an increased sensitivity to brain activation for these channels. Averaging all short-separation channels and considering the resulting signal as physiological noise, should reduce the chance of including brain activation in the regressor. However, new developments in probe design and the miniaturization of optode components should solve this problem and allow for a more localized regression of the physiological oscillations.

While all previously described methods reduced the physiological noise and then recovered the hemodynamic response via a block-average or GLM, Gagnon et al. (2011) tried to simultaneously reduce physiological noise and estimate the hemodynamic response using a state-space modeling approach. They developed both a static and a dynamic estimator (a Kalman filter estimator) and they showed that the latter was performing better in recovering the hemodynamic response. The static estimator was an improved version of the method proposed by Saager and Berger (2008): the reduction of physiological noise from standard channels signal and the estimate of the hemodynamic response were performed in a unique step. The Kalman filter estimator acts on a state-space representation of a dynamic system to provide, recursively, a solution to the linear optimal filtering problem (for more information on the Kalman filter theory see Grewal and Andrews (2001); Haykin (2001)). Here, the Kalman filter estimator was able to simultaneously remove physiological noise and recover the hemodynamic response. It performed better than the static estimator because physiological noise is non-stationary. Moreover, performing the two steps simultaneously prevented underestimation of the hemodynamic response. This approach is very powerful, however it has some pitfalls. First of all, the Kalman filter estimator needs some initial estimates (measurement noise and process noise covariance matrices, for example), which can be difficult to obtain. Secondly, the filter needs a prior model of the hemodynamic response. The model chosen by Gagnon

et al. (2011), a set of Gaussian temporal basis functions, was very flexible. However, choosing the number of basis functions is not so trivial, since a high number may cause over-fitting of the phase-locked physiological noise, while a low number may raise the number of constraints imposed by the model, preventing the estimation of hemodynamic responses with different dynamics.

The same authors (Gagnon et al., 2012a) demonstrated that physiological noise oscillations in the scalp layer are not homogeneous in the whole head. Indeed, they showed that using the signal acquired at short-separation channels located nearby the standard channels is more efficient in removing physiological noise contamination than using a signal coming from a short-separation channel located far from the standard channels. They also showed that the performance of the Kalman filter estimator in reducing physiological noise oscillations and recovering the hemodynamic response is further improved when using two short-separation channels, one located near the source and the other near the detector (Gagnon et al., 2014). These results are very promising, showing a great improvement in the reduction of physiological fluctuations. Nevertheless, a great number of sources and detectors is needed in order to implement these advances. Unfortunately, all NIRS instruments have a limited number of sources and detectors, which can limit the use of multiple short-separation channels.

2.3 Image reconstruction

When performing a DOT acquisition, the aim is to produce a 3D image of the concentration changes of HbO and HbR occurring in the probed volume, instead of being limited to time-series plots of the signal at each channel, as in the fNIRS case. Image reconstruction with optical data is not as straightforward as image reconstruction in x-ray computed tomography (CT). Indeed, in CT, the scattering is minimal and the path taken by x-rays between source and detector can thus be approximated by a straight line. In optical tomography, instead, scattering is the dom-

inant effect and hence, the path taken by photons cannot be expressed as a straight line. This condition makes image reconstruction with optical data a challenging mathematical problem (Arridge, 1999, 2011). A realistic model of the probed volume and an accurate model of how light will propagate in the tissues are the first key elements to solving the image reconstruction problem. As we have seen in paragraph 1.2, several methods have been proposed to solve the forward problem. For a given array of sources and detectors, these methods can be used to compute the distribution of light in the given tissues. By simulating the path taken by photons according to the specified source-detector configuration, it is possible to predict how a set of optical measurements would change for a given change in optical properties in the volume. The output of the forward problem is a sensitivity matrix, which links the optical properties of the probed tissues to the simulated optical signals at each channel. This sensitivity matrix is the key element in the final stage of image reconstruction: solving the inverse problem. This involves calculating the optical properties of the tissues given a set of real optical measured signals and thus imaging the concentration changes of HbO and HbR occurring in the brain.

In the following paragraph a brief overview of the theory of the inverse problem in image reconstruction is presented. Even if the best methods to solve the forward and inverse problem are used, an accurate solution can be computed only when an accurate and realistic optical head model is used. Hence, an overview of the available optical head models for image reconstruction is also presented.

2.3.1 Image reconstruction theory

If the forward problem is formulated as:

$$y = F(x) \tag{2.1}$$

where y are the channel-wise data, x the tissue optical properties (i.e. the image) and F the forward operator, then the inverse problem can be

expressed as:

$$x = F^{-1}(y) \tag{2.2}$$

If the aim is imaging the difference between two states, that is two time points, and this difference is considered small, then the non-linear inverse problem can be linearized. This assumption is usually valid when imaging functional activation studies, since functional brain responses usually cause a small change in tissue optical properties. Thus, equation 2.1 can be expanded in a Taylor series about x_0:

$$y = y_0 + F'(x_0) \cdot (x - x_0) + F''(x_0) \cdot (x - x_0)^2 + ... \tag{2.3}$$

where F′ and F″ are the first and second Fréchet derivatives of F, where the Fréchet derivatives are a linear integral operator. F′ and F″ can be represented by matrices J, the Jacobian, and H, the Hessian, in order to solve the forward problem. Neglecting higher order approximations terms equation 2.3 can be linearized:

$$\Delta y = J \Delta x \tag{2.4}$$

where $\Delta x = x - x_0$ and $\Delta y = y - y_0$ represent the changes in optical properties and data, respectively. Thus, what is actually computed solving the forward problem is the Jacobian matrix J. When the optical data y are expressed as intensity, the obtained linearization is called the Born approximation, while when the optical data y are expressed as log intensity, the linearization gives rise to the Rytov approximation.

The inverse problem of image reconstruction consists of inverting the matrix J. There are several approaches to perform this task, which differ mainly in the regularization step of the matrix (e.g. Tikhonov regularization). The most common is the Moore-Penrose generalized inverse with a Tikhonov regularization parameter (λ):

$$\Delta x = J^T (J J^T + \lambda I)^{-1} \Delta y \tag{2.5}$$

where I is the identity matrix (Boas et al., 2009; Gibson et al., 2005).

In cases when the linear approximation is not justified, e.g. when absolute values of optical properties are to be reconstructed, the non-linear inverse problem has to be solved. An example is when static brain images are acquired. In this case, an objective function, given by the difference between data simulated in the forward problem and real acquired data, is defined and the inverse problem is solved by trying to minimize this objective function via numerical methods (e.g. Newton or gradient method) (Arridge, 2011; Gibson et al., 2005).

Whichever way image reconstruction is performed, it remains a non-unique, ill-posed and underdetermined problem. In order to improve the accuracy of the reconstructed image, several ideas have emerged. Among these is the need to use overlapping measurements in order to provide more uniformity in the spatial sampling of the target. This highlights the importance of the design of the array of sources and detectors. Another way to improve image reconstruction is to use prior anatomical information, derived for example from MRI images. This will lead to a more accurate solution of the forward problem, enhancing the accuracy of the final reconstructed image. Prior anatomical information may also be included in the inverse problem, improving its solution (Boas et al., 2004).

2.3.2 DOT OPTICAL HEAD MODELS

Anatomical information not only helps restrain the ill-posed inverse problem, but also allows meaningful visualization of the DOT images (Bamett et al., 2003; Boas and Dale, 2005; Guven et al., 2005; Pogue and Paulsen, 1998; Schweiger and Arridge, 1999; Zhang et al., 2005a). To produce an accurate forward model, a realistic, multi-layered head model of the different tissues of the human head, each assigned accurate optical properties, is essential. Furthermore, an accurate localization of the sources and detectors on the participants' head is mandatory for an accurate solution.

The best practice approach to performing DOT image reconstruction

is therefore to register the DOT source and detector locations to each subject's individual MRI image, and use that MRI image to construct a subject-specific, multi-layered head model. However, acquiring an MRI image for every participant undermines the intrinsic advantages of the DOT technique, i.e. portability and applicability to challenging populations. The use of a generic head model, based on an MRI atlas, is a suitable and effective solution to this problem (Custo et al., 2010; Tsuzuki and Dan, 2014).

Each atlas must first be registered to each subject, usually by recording the location of a number of the subject's cranial landmarks and the DOT source and detector positions with a tracking system or with photogrammetric methods (Tsuzuki and Dan, 2014). As the corresponding cranial landmarks can be identified on the chosen atlas, the atlas volume can be transformed to match the subject's cranial dimensions (most simply by an affine transformation, see Singh et al. (2005); Tsuzuki et al. (2012)). This registered atlas volume will then match the size, and to some extent the shape, of the individual's head, and an accurate forward model can be computed within this space. Using this process, an optical head model can enable an MRI-free approach to diffuse optical image reconstruction.

2.3.2.1 Adult optical head models

A number of adult atlases have been applied to DOT (Custo et al., 2010; Ferradal et al., 2014; Habermehl et al., 2012; Tian and Liu, 2014). These include the Colin27 MRI atlas (Collins et al., 1998), which consists of a high-resolution MRI volume of a single individual and the non-linear ICBM152 atlas (Fonov et al., 2011), which constitutes a spatial average of 152 adults. Although the Colin27 atlas has been preferred by some groups because of its more detailed visualization of the cortical gyri, it can result in a biased head model, since it is based on a single subject brain. On the other hand, the MNI152, being an average of many brains, may be a better representation of the general population, although its cortical gyri are obviously less clear.

If using head models instead of the individual's MRI is essential in order to fully exploit all advantages of the optical techniques, a spontaneous question arises as to whether the head model is able to correctly localize the reconstructed activation changes in the brain. Atlas-guided DOT will obviously exhibit errors in the localization of cortical activation; the question is whether this error is small enough compared to DOT spatial resolution. The sources of this error can be due, firstly, to the difference between the subject's true anatomy and the atlas anatomy, secondly to the error in registration between the atlas and subject spaces and thirdly to the error inherent in the process of image reconstruction.

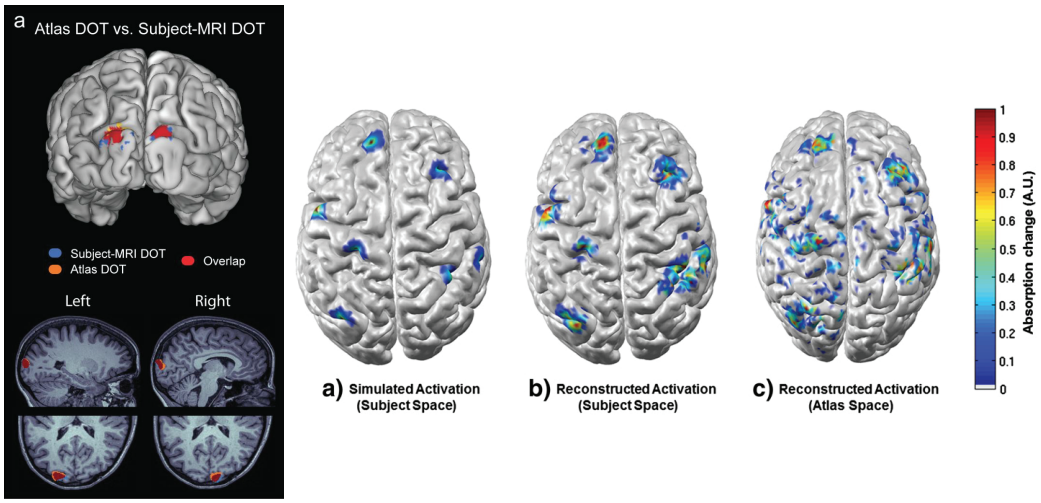

Figure 2.3.1: Comparison between the DOT activations computed using the subject's own MRI and the atlas. a) Note the high overlapping (red areas) between the two computed activations (taken from Ferradal et al. (2014)). b) Similar activation patterns recovered in the atlas and subject space, and both of them are similar to the simulated activation pattern (taken from Cooper et al. (2012b))

Cooper et al. (2012b) and Ferradal et al. (2014) answered this question, validating the use of head models for DOT reconstruction. They showed that by employing a generic atlas head model, the localization error associated with DOT reconstruction in adults increases significantly when compared to that obtained using the subject's own MRI. However, atlas-based DOT can obtain a localization accuracy of ~10 mm, which is suf-

ficient to identify the location of an activation within the gross cortical anatomy and even within a given cortical gyrus (Fig. 2.3.1). In this way, they validated the use of atlas-based DOT as a neuroimaging tool. Furthermore, with new hardware developments and improvements in high-density DOT source-detector designs, the localization accuracy of cortical activation should increase, allowing a more precise localization on the cortical gyri.

2.3.2.2 Neonatal optical head models

Despite the widespread use of DOT in the neonatal field, there are a limited number of studies that have attempted to produce accurate infant head models (Dehaes et al., 2013; Fournier et al., 2012; Heiskala et al., 2009; White et al., 2012). Indeed, acquiring an MRI image of a newborn baby is challenging and is rarely performed unless clinically necessary. There are also difficulties in dealing with newborn MRIs because of a lack of established automatic tools to segment the neonatal MRI images into different tissue types (cerebrospinal fluid (CSF), grey (GM) and white matter (WM) for example). Indeed, automatic segmentation of the neonatal brain tissues remains a challenging problem because the contrast between the tissues is different and usually lower than that in adults and the within-tissue intensity variability is high (Altaye et al., 2008; Prastawa et al., 2005). The tools available for adult MRI segmentation cannot always be utilized without introducing significant errors (Wilke et al., 2003). As a result, there are a limited number of high-resolution MRI data-sets available for newborns and even fewer for preterm babies.

Because the brain of the newborn infant is developing extremely quickly, accurate DOT reconstruction requires head models that are carefully age-matched. The brain structure of a 30 weeks PMA (Post Menstrual Age) newborn is markedly different from that of a full term (40 weeks) baby (Battin and Rutherford, 2002). A single generic atlas, which can be applied to adults spanning a wide range of ages, will not be suitable for neonatal DOT. An atlas with age-specific infant MRIs, from pre-term to

term, is therefore needed to produce suitable optical head models. DOT image reconstruction can then be performed using the correct, age-matched anatomy.

A small number of term-age MRI atlases have been constructed and described in the literature. The atlas proposed by Shi et al. (2011) was built by registering and spatially averaging MRIs obtained from 95 infants aged between 38.7 and 46.4 weeks PMA to produce a single, term-age atlas volume. Similarly, the atlas proposed by Oishi et al. (2011) used data from 25 infants aged between 38 and 41 weeks PMA and the atlas proposed by Heiskala et al. (2009) used 7 infants aged between 39 and 41 weeks PMA. The atlas proposed by Sanchez et al. (2012) averaged MRIs acquired on 23 babies aged between 8 days to 29 days after birth.

Although these single-age atlases have many applications, the ideal neonatal atlas should be built from MRI data obtained over a wide pre-term to term age range, and would ideally include enough data at each age to allow an atlas to be dynamically produced for any arbitrary age within that range. The atlas proposed by Kuklisova-Murga sova et al. (2011) does just that. Using MRI images recording on 142 infants ranging from 29 weeks PMA to 47 weeks PMA and using a weighted averaging approach this atlas allows the production of tissue probability maps for any age in this range, and the resulting volumes are publicly available for 29 to 44 weeks in one week intervals (`www.brain-development.org`) (see Fig. 2.3.2).

Although this 4D atlas provides a great resource for producing age-matched head models for DOT, there is one significant difficulty preventing the use of the volumes that are currently available online. Because DOT requires a forward model to be computed based on the scalp locations of each source and detector, a model of the extra-cerebral tissues is essential. For a number of reasons, including data protection and a more accurate registration and segmentation, the scalp and skull layers visible in the MRI data are usually stripped out of the image prior to that data being included in the atlas.

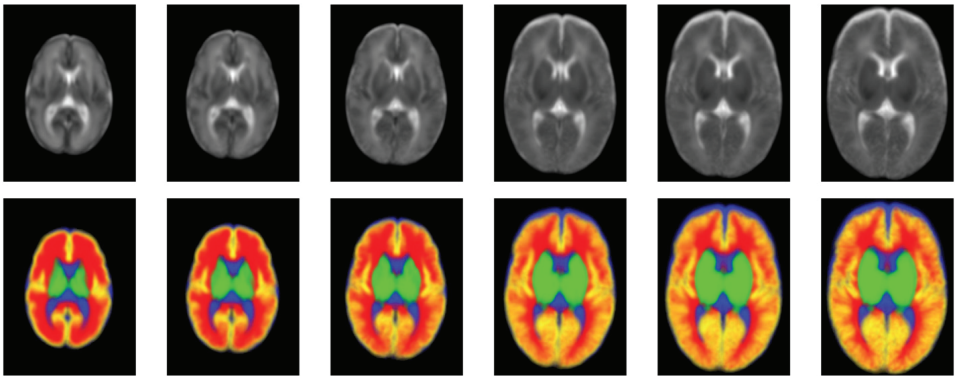

Figure 2.3.2: MRI atlases for some example ages (29, 32, 35, 38, 41 and 44 weeks PMA) taken from Kuklisova-Murga sova et al. (2011). Note the difference in head size and also anatomy between the different ages. In the first row the intensity template is shown, while in the second the color coded sum of the tissue probability maps (i.e. a map for every tissue indicating the probability of a certain voxel to be that tissue type). The tissue types considered are grey matter, white matter, CSF, cerebellum and brainstem.

Until now, it was not possible to create age-matched infant head models for DOT. Dehaes et al. (2013), used a term-age baby female subject to build their head model, thus restricting the possibility to make inferences at the population level, while Fournier et al. (2012) built their pre-term 30-weeks head model by averaging 19 baby's MRIs, 7 of which, however, had suffered a brain injury (Intra- Ventricular Hemorrhage), thus creating a likely biased head model. The head models created by Heiskala et al. (2009) and White et al. (2012) were less biased, since they were created using, respectively, 7 MRIs and 12 MRIs of healthy full-term neonates, but are valid only for 40-weeks term babies.

2.4 fNIRS and DOT in cognitive neuroscience

Optical techniques are ideal for cognitive neuroscience studies. Indeed, they are easily applicable to infants and children, giving new insights in the neuro-developmental processes from a hemodynamic point of view. Elderly people or psychiatric patients can benefit from optical techniques as well, because they are portable and less susceptible to motion artifacts.

Furthermore, all the fields of cognitive neuroscience in adults can take advantage of optical techniques, which are easily applicable in a range of cognitive studies, particularly in situations where other techniques, such as fMRI or EEG, are not feasible or cannot provide the desired parameters. In the next paragraph, a brief overview of the application of optical techniques in the field of cognitive neuroscience is presented, with a separate focus on adult and infant studies.

2.4.1 Infants and children

Infants and children are the ideal candidates for optical techniques, thanks to their relatively thin skull and scalp tissues and their generally sparse hair, which allows light to penetrate easily. Because of new hardware improvements, which have allowed the development of new arrays able to interrogate multiple brain areas and the non-invasive and portable nature of the instrumentation, studies investigating the developing brain using optical methods have shown tremendous growth in the last decade (Boas et al., 2014; Lloyd-Fox et al., 2010). Cristia et al. (2013) created an online database of infant studies where optical techniques were used. This database can be updated by the community, in order to share methodological knowledge and hence allow results to be more robust and replicable.

Auditory, visual, olfactory or motor stimuli can be presented to babies or children and the brain response to these stimuli can provide important information about cognitive functions, for example memory, face perception, attention, language acquisition, etc. Recently, for example, Buss et al. (2014) have shown the ability of fNIRS to detect task-specific variations in the fronto-parietal network during a visual working memory task in 3 and 4 years old children. They have demonstrated that, when reaching the visual working memory capacity, there is a continuous increase in HbO concentration changes, unlike in adults, where, instead, they stop increasing. This may lead to the conclusion that visual working memory is still not fully developed before 4 years of age. Wilcox et al.

(2014) showed the presence of color-priming in 8 and 9 month old babies. In this case, the anterior and posterior temporal cortices are the brain areas involved. Southgate et al. (2014), in a similar age group (9 month old infants), reported the brain areas involved in representing the goal of actions performed by others (e.g. the areas activated in the infant's brain when an adult was moving a red cone near a blue cube). They found a similar pattern and localization of activation as seen in adults, with the left anterior parietal region displaying suppression during action repetition and release from suppression when encountering new goals. Ding et al. (2014) investigated how face processing of other race and own race faces changes with age, in 7- to 13-year old children. They demonstrated that processing other race faces requires more resources, with an increase in HbO in the right middle frontal gyrus and inferior frontal gyrus regions and in the left cuneus compared to when processing own race faces, and that the size of this difference increases with age.

Optical techniques are also ideal for the study of atypical brain development (Vanderwert and Nelson, 2014). Example applications include the study of Attention Deficit Hyperactivity Disorder (ADHD) and Autism Spectral Disorder (ASD). Weber et al. (2005) acquired data on two groups of 10 year old children, one suffering from ADHD and one as control, using a trial-making test in which children had to connect in ascending order a series of numbers appearing on a screen. The task was performed 4 times. They found an increase in cerebral blood volume in both hemispheres and of HbO in the right hemisphere in the ADHD group during the first of the 4 sessions. These results may imply a deficit in the short-term attention of ADHD patients. Other than sustained attention, ADHD children also suffer deficits in attentional control. Many fNIRS studies have investigated these deficits with color-word matching Stroop task and go-nogo tasks, finding evidence of disrupted frontal cortex activity (Inoue et al., 2012; Jourdan Moser et al., 2009; Negoro et al., 2010; Xiao et al., 2012). The Stroop task required children to name the color in which the word appeared on the screen, with the difficulty being that the word was the name of a color but dif-

ferent from the printed one (e.g. 'green' printed in blue). In the go-nogo tasks children had to react to certain stimuli and inhibit their response when a particular stimulus was presented. These tasks are thus ideal to investigate deficits in attentional control. The studies investigating autism focused on face and speech/language processing, since the main deficits of autistic children include social communication and language. Minagawa-Kawai et al. (2009) studied phonemic and prosodic processing in a group of ASD children and a control group. They found a right lateralization for prosodic processing both in normal developing and ASD children, but a left lateralization for phonemic processing in the normal developing group only. These results may indicate a disruption in phonemic processing in patients suffering from ASD. Funabiki et al. (2012), instead, investigated where the problem of hypersensitivity to sounds or the lack of awareness to sounds originated from in the brain of ASD patients. They found a difference in hemodynamic response between an ASD group and the control group in the frontal cortex, and not in the auditory cortex. These results may suggest that these contrasting behaviors of hypersensitivity or unawareness to sounds in ASD may originate from difficulties in attention rather than auditory cortex dysfunctions. Kita et al. (2011) investigated social development functions in ASD, trying to find the neurological substrates of self-face recognition. They found increased levels of HbO in the right inferior frontal gyrus compared to the left and they also correlated the severity of ASD with the scale of the measured HbO response (lower activity levels for more serious ASD patients). These results may suggest that dysfunctions in the right inferior frontal gyrus play a key role in self-face processing deficits found in many ASD patients.

Resting state acquisitions can also give new insights in the study of the developing brain. For example, Cooper et al. (2011) applied DOT to neurologically damaged neonates, diagnosed with seizures. They found the presence of a slow and significant increase in HbO concentration, followed by rapid decrease and subsequent slow return to baseline in the neurologically damaged neonates group, while this pattern was never

found in the healthy group. These findings highlight the importance of applying optical techniques in the study of brain damage in neonates. Another example of resting state acquisition has been performed by Imai et al. (2014), who acquired data from neonates admitted to the neonatal intensive care unit classified as term babies, preterm babies or babies with Down's syndrome. They found a decrease in functional connectivity in neonates diagnosed with Down's syndrome, while no differences were found between term and preterm babies. These results may highlight a disruption in functional connectivity development in babies with Down's syndrome.

2.4.2 Adults

Optical techniques have also reached widespread use in the adult population, thanks to their portability and non-invasiveness (Boas et al., 2014; Cutini et al., 2012a; Homae, 2014). They can be applied to patients that cannot enter an fMRI scanner and, thanks to their higher temporal resolution compared to fMRI, they can give new insights into some cognitive processing in the brain. For example, Cutini et al. (2014), thanks to the high resolution of fNIRS, have been able to detect small differences in the peak latency between hemodynamic responses acquired during subitizing and those measured during estimation in a visual enumeration task. When presented with a certain number of dots, humans usually act in two different ways in order to enumerate them, depending on the numerosity of the set. For small sets (up to 4 items) numerosity judgments are usually rapid and precise, a process known as subitizing, while for larger sets the judgments are usually error-prone estimates. Furthermore, the authors localized the neural dissociation between subitizing and estimation in the right intraparietal sulcus (IPS). The same author (Cutini et al., 2012b) had already demonstrated the capability of fNIRS to measure the neural correlates of the SNARC (Spatial-Numerical Association of Response Codes) effect, i.e. of the interaction between numbers and space. In magnitude comparison, reaction times to small numbers are

faster with left than right effectors, while the opposite is found for large numbers. The neural correlates were found bilaterally in the IPS and in the left angular gyrus. There results suggest the intrinsic spatial nature of numerical magnitude representation.

In recent years, the neural correlates of emotions have been investigated and optical techniques may allow a more suitable experimental setting than other neuroimaging techniques. Tupak et al. (2014) acquired data from participants labeling neutral and threatening pictures and found an increased activation in the ventrolateral prefrontal cortex (VLPFC) during labeling of threatening pictures only. These results suggest that the VLPFC may have a key role in emotion regulation. Schneider et al. (2014), instead, investigated the neural correlates associated with emotionally expressive body movement and posture. Participants had to judge the emotional state of faceless avatars, which performed fearful, angry, sad, happy or neutral gait patterns. They found an increase in activation during negative emotions compared to neutral in the right occipito-temporal and left temporal and temporo-parietal brain regions. These results suggest the presence of a distributed brain network involved in the processing of body-related emotion.

Another field of interest for optical studies is motor control, since optical techniques are less susceptible to motion artifacts and allow easier data acquisition during motor tasks. Mihara et al. (2007) and Miyai et al. (2002, 2003) demonstrated the ability of optical techniques to gather brain activity information during normal and impaired locomotion. Mihara et al. (2007) measured stroke patients during recovery of ataxia during walking on a treadmill, and found a sustained prefrontal activation during ataxic gait. These results suggest that this brain area may play an important role in the compensatory mechanisms for ataxic gait. Miyai et al. (2002, 2003) acquired optical data during a hemiplegic walk on a treadmill in patients who suffered a severe stroke. They found enhanced activation in the premotor area of the affected hemisphere during hemiplegic gait. Their results suggest that the premotor cortex and the pre-supplementary motor area may play a key role in the process of restora-

tion of gait in patients who suffered a severe stroke. Recently, Koenraadt et al. (2014) acquired data on healthy subjects walking on a treadmill normally or on determined spots for the feet. They found an increased activation in the prefrontal cortex and in the supplementary motor area prior the beginning of both tasks. Tthey did not find significant differences between the activation in the sensorimotor cortex during standing and walking. These results suggest that the control of gait may depend on subcortical automatism only.

A further field that might benefit from fNIRS is the development of a Brain Computer Interface (BCI). BCI systems establish a direct connection between the brain and an external device: communication and rehabilitation are the most important applied fields of BCI systems (Birbaumer and Cohen, 2007). Indeed, the latter can provide an effective solution for severely disabled patients (e.g., those suffering from amyotrophic lateral sclerosis, brainstem stroke and spinal cord injury) to interact with the environment. fNIRS BCIs have already been used in non-clinical contexts, such as the decoding of individual preferences (Luu and Chau, 2009) and mental arithmetic (Bauernfeind et al., 2011). Moreover, a recent optical investigation by Power et al. (2012) attempted to perform a single-trial discrimination from the prefrontal activity elicited by three different mental activities: mental arithmetic, mental singing and a no-control state. The results are remarkably encouraging, showing that in some participants it is possible to achieve a three-state discrimination well above chance level. Recently, Kaiser et al. (2014) investigated the effect of training on the sensorimotor cortex using a motor imagery-based BCI. They found an enhanced activation pattern in the sensorimotor cortex mainly in participants with low BCI performance. These results suggest that this paradigm can affect cortical activation patterns and thus be suitable for BCI aimed at promoting neuroplasticity.

Optical techniques have been applied in many other fields, from psychiatry to neurology to cognitive science, in order to study other cognitive functions such as attention, memory, language, vision, pain, resting state networks, etc. Many fMRI studies have been replicated with opti-

cal techniques and many others have revealed new insights that fMRI or other techniques could not reveal.

2.5 Open issues and aims of the thesis

2.5.1 Open issues

As emerges from this introductory chapter, there are several problems still affecting optical near-infrared technology. One of the main difficulties in dealing with optical measured signals is the presence of physiological noise oscillations, which exert a strong camouflaging effect on the brain-driven optical signal and hence must be removed in order to properly estimate the hemodynamic response. Over the past decade, neuroscientists interested in localizing brain activity underpinning the execution of specific cognitive tasks have progressively abandoned blocked designs, where hemodynamic changes are tracked as temporally extended continua, in favor of event-related designs, where the signal of interest is partitioned in time-windows locked to the onset of each stimulus. Nevertheless, event-related designs suffer more strongly from physiological noise contamination, because of the very low amplitude of the hemodynamic response, and have thus brought to light even more the need to find a method to reduce physiological noise contamination in standard optical channels. As a result, several methods have been proposed in the literature in order to reduce these oscillations, but none has become the standard method. Recently, the use of a short-separation channel has further increased the possibility of removing physiological noise fluctuations in standard channel but the problem is not totally solved.

Another signal processing challenge with optical signals concerns motion artifacts. Several techniques have been proposed in the literature, but none has become a common standard in the NIRS processing pipeline. Indeed, motion artifacts can have different shapes, frequency content and timing. They can be high amplitude, high frequency spikes, easily detectable in the data-series or they can have lower frequency content and

be harder to distinguish from normal hemodynamic fNIRS signals. They can be isolated events or they can be temporally correlated with the HR. Therefore, it is likely that the efficacy of each motion artifact correction technique will vary with the type of motion artifact and that the best technique to apply is data-dependent. Hence, the user is forced to decide which technique to use at every acquisition and there are no objective tools available to perform this choice.

Moving to image reconstruction in the neonatal field, one of the biggest problems is the lack of age-specific MRI atlases to be used for image reconstruction in preterm and term babies. This causes image reconstruction to be performed on anatomically incorrect models of the infant brain.

2.5.2 Aims of the thesis

In chapter 3 of this thesis a novel short-separation channel-based method (ReMCoBA) to reduce physiological noise contamination is presented. As previously stated, the signal acquired at a short-separation channel is ideal to derive information about noise generated by physiological sources not influenced by stimulus-evoked brain activity. Removing the noise recorded from the short-separation channel from standard channels is the first step of the method presented herein. More specifically, the short-separation channel signal is used to estimate a parametric model of physiological noise, which is, in turn, used to correct the signal recorded from standard channels. The newly proposed algorithm includes a second step, in which residual random noise is further reduced by adopting a Bayesian filtering method. Hemodynamic response estimates are finally obtained by averaging stimulus- evoked HRs of to the same stimulus type. Every step of the method is performed on every single-trial separately; in this way, the proposed method can be considered a time-varying approach. One novelty of this approach is found in the non-parametric nature of HR estimates: contrary to, for example, the Kalman filter approach, HR estimates are obtained with a model-free approach and the only information needed by the Bayesian filter is the smoothness

of the hemodynamic response. ReMCoBA is thus a very flexible and general method for estimating hemodynamic responses. The method is very easy to implement and also computationally efficient.

In chapter 4 of this thesis, the problem of motion artifacts is addressed, and a comparison of the performance of the main motion correction techniques found in the literature on real cognitive data is undertaken. The results highlight the importance of the motion correction step in the fNIRS processing pipeline. Importantly, the objective approaches proposed in order to compare the different motion correction techniques have to be considered as the best approach for fNIRS motion correction analysis for the time being, since a single, universally effective motion correction method is not finalized. Indeed, it is only after many different data-sets with different types of motion artifacts have been analyzed and compared using different motion correction techniques, and the approaches proposed here, that a universal approach can be identified and accepted.

Eventually, in chapter 5 of this thesis, a 4D neonatal head model is presented, which can bridge the gap in the atlases available for image reconstruction. For the first time, a neonatal atlas, spanning the preterm to term age range (from 29 to 44 weeks post-menstrual age) is presented. The proposed head model includes, for each week: 1) A multi-layered tissue mask which identifies extra-cerebral layers, cerebrospinal fluid, grey matter, white matter, cerebellum and brainstem, 2) A high-density tetrahedral head mesh, 3) Surface meshes for the scalp, grey-matter and white matter layers and 4) Cranial landmarks and 10-5 locations on the scalp surface. This package, freely available online, can be applied by users of near-infrared spectroscopy and diffuse optical tomography to optimize probe locations, optimize image reconstruction, register data to cortical locations and ultimately improve the accuracy and interpretation of diffuse optical techniques in newborn populations.

Eventually, in the last chapters of this thesis, examples of applications of the proposed filtering techniques and head models on empirical neural activation data are presented.

PART II
New methodologies and tools for fNIRS signal processing and neonatal DOT image reconstruction

3

ReMCoBA, a novel algorithm for physiological noise removal and HR estimation for fNIRS signals

In the present chapter ReMCoBA (Reference-channel Modeling Corrected Bayesian Approach), a novel technique able to reduce physiological noise and recover hemodynamic responses both in event-related and block designs, is presented (Scarpa et al., 2013). To remind that the term reference-channel has the same meaning of short-separation channel, a channel with a source-detector distance < 1 cm, which measures physiological noise oscillations but no brain activity.

In the following paragraphs a description of the technique is presented. Two datasets will be used for the assessment of the proposed methodology on real and synthetic data and for the comparison with two literature methods for HR estimation, one of which implements a solution based

on the use of the SS-channel. The results of the comparison are hence reported and a discussion on the results achieved by the new method is proposed.

3.1 Reference-channel Modeling Corrected Bayesian Approach (ReMCoBA)

The proposed method consists in two main steps: a model of the physiological noise is derived by the SS-channel and used to correct raw fNIRS data of the other standard channels (see paragraph 3.1.1); the resulting data are then filtered, on a single-trial basis, with a nonparametric Bayesian approach to reduce residual random noise (see paragraph 3.1.2).

Raw data time-series of standard and SS-channels are first band-pass filtered (Butterworth, 4th order, band-pass 0.01-3 Hz) to remove any very slow drift and noise with frequency far from that of the HR. The signal is then segmented in trials and undergoes the two-step procedure.

3.1.1 Step 1: SS-channel modeling and fNIRS data correction

The fNIRS signal $y(t)$ acquired at standard channels after a stimulus given at $t = 0$ contains the event-related HR, which can be considered the useful component $u(t)$, and then a physiological noise component $\varphi(t)$ and random noise $v(t)$:

$$y(t) = u(t) + \varphi(t) + v(t) \tag{3.1}$$

An fNIRS SS-channel signal $y_{SS}(t)$ contains, by hypothesis, the same physiological noise $\varphi(t)$ of standard channels scaled by a coefficient s (constant in time) which takes into account the different paths crossed by photons and random noise $\epsilon(t)$:

$$y_{SS}(t) = \frac{\varphi(t)}{s} + \epsilon(t) \tag{3.2}$$

Thus, the idea is to exploit the signal $y_{SS}(t)$ to remove, or at least reduce, the physiological noise $\varphi(t)$, which is present also in the standard channels $y(t)$. This is feasible only if $y_{SS}(t)$ and $y(t)$ have a good correlation, otherwise there is the risk of adding more noise instead of reducing it. For this reason, Step 1 is performed only if the total Pearson's correlation coefficient between the two channels ($y(t)$ and $y_{SS}(t)$) is above 0.6; otherwise, Step 1 is skipped and the algorithm goes directly to Step 2 (see paragraph 3.1.2). In order to maximize the usefulness of the SS-channel, for each standard channel, the SS-channel chosen between the available ones is the one with the highest Pearson's correlation coefficient.

Physiological noise is modeled as a sum of M sinusoidal waves (similarly to Prince et al. (2003)), on a trial-by-trial basis:

$$\varphi(t) = \sum_{i=1}^{M} [a_i sin(2\pi\omega_i t) + b_i cos(2\pi\omega_i t)] + c + w(t) \tag{3.3}$$

where $w(t)$ is the model error. For each trial, the number M and the value ω_i of the dominant low frequencies (<0.18 Hz) are individuated from the power spectrum. In the procedure of Step 1 the maximum value allowed to M is 3, since, usually this is the maximum value of dominant low frequencies that could be detected in real data (corresponding to respiratory frequency, Mayer's and very low-frequency oscillations). Unlike Prince et al. (2003) where the number of sinusoidal waves is fixed at 3, M is kept variable among the trials, given that oscillatory components are not always detectable with a sufficient accuracy during the entire recording session. This yields a reduction of the number of parameters (e.g. in the used real data, M will result to be 1 in 19% of trials, 2 in 59%, and 3 in 22%). Even if physiological noise is composed of other components (e.g. heart beat), here we are interested in modeling only the 3 low frequency components, which lie in the same frequency band of HR. The initial value of the frequencies ω_i obtained from the spectrum is then optimized through a grid search method (Händel, 2000). In equation 3.3, the parameters a_i, b_i and c are estimated by the least-squares method. Having an estimate of φ, the scaling coefficient s in equation 3.2 is deter-

mined by minimizing the squared difference between the SS signal $y_{SS}(t)$ and the standard channel signal $y(t)$ observed in 30 s of resting state data acquired before each experimental session (so as to compensate for possible differences in the magnitude of the pathlength factor between short-separation and standard channels). Having provided the estimates of all unknown parameters (denoted by the hat symbol) in equations 3.2 and 3.3, the corresponding trial of the standard channels is so corrected:

$$y_c(t) = y(t) - \hat{s} \sum_{i=1}^{\hat{M}} [\hat{a}_i sin(2\pi\hat{\omega}_i t) + \hat{b}_i cos(2\pi\hat{\omega}_i t)] + \hat{c} \tag{3.4}$$

The resulting corrected signal $y_c(t)$ is then submitted to Step 2 (Fig. 3.1.1).

The procedure of the present subsection produces a result that may resemble that of a notch filter. However, this is not completely equivalent to what a notch filter would do on a data-stream. In fact, a notch filter would unavoidably introduce a distortion on the HR because of the superimposition of the spectral content of the HR with that of the physiological noise components.

3.1.2 Step 2: Single trial Bayesian filtering and hemodynamic response estimation

The corrected signal is filtered with a Bayesian approach developed and tested on fNIRS data by Scarpa et al. (2010). Briefly, data $y_c(t)$ of each standard channel can be described as:

$$y_c(t) = u(t) + v(t) \tag{3.5}$$

where $u(t)$ is the useful component (the HR) and $v(t)$ the remaining noise. Trial by trial, the signal $y_c(t)$ is filtered within a Bayesian embedding by exploiting a priori expectation on both HR and noise. Re-

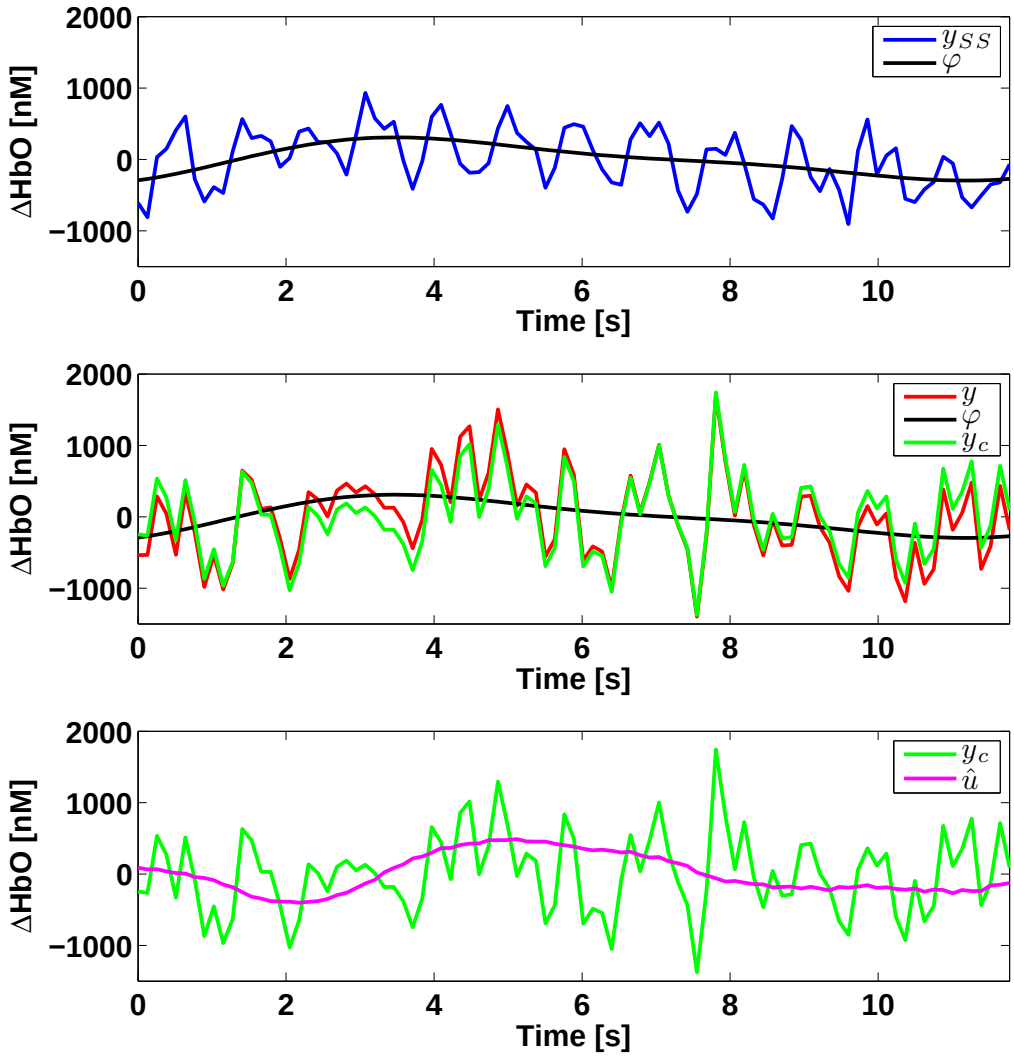

Figure 3.1.1: Examples on a selected trial of the steps performed by ReMCoBA. In the first row a 12 s trial measured at a short-separation channel (blue line) is displayed and superposed there is the computed noise model φ (black line). In the second row the correction step is visualized. The computed noise model φ is subtracted from the same trial of a standard channel signal (red line) to get the corrected signal y_c (green line). In the third row the bayesian filtering step is displayed: the corrected signal is filtered with a bayesian approach and the final estimated useful signal $\hat{u}$ is obtained (magenta line).

expressing equation 3.5 in vector form, we get:

$$y_c = u + v \tag{3.6}$$

where u and v are vectors containing the n samples of the trial. A stationary autoregressive (AR) model is employed as a priori description of v (different for each of the N available trials of each condition). In order to keep the number of parameters as low as possible, model order is determined by using the Akaike information criterion (AIC). On 80% of the trials, the most parsimonious model order was 4. This was the value that provided the best estimation error using the data of Scarpa et al. (2010). Hence, model order is set to 4 and the a priori covariance matrix of v is:

$$\Sigma_v = \sigma^2(A^T A)^{-1} \tag{3.7}$$

where A is a square (n-size) Toeplitz matrix the first column of which is $[1, a_1, a_2, a_3, a_4, 0, ...0]^T$, $\{a_k\}_{k=1,...,4}$ being the coefficients of the AR model, and σ^2 is the variance of the noise process which drives the AR model. For each of the available trials, $\{a_k\}_{k=1,...,4}$ and σ^2 are identified from data measured in an interval lasting 4 s and starting from 1.5 s before the stimulus (when HR is not present). Therefore, A and σ^2 in equation 3.7 are determined on a single-trial basis. As far as the a priori information on u, the strategy is to model its expected smoothness as the realization of a stochastic process obtained by the cascade of 2 integrators driven by a zero-mean white noise process ϵ_k with variance λ^2. Therefore, the covariance matrix of u is:

$$\Sigma_u = \lambda^2(F^T F)^{-1} \tag{3.8}$$

where $F = \Delta^2$, with Δ^2 being the square n-dimensional lower- triangular Toeplitz matrix the first column of which is $[1, -2, 1, ..., 0]^T$. While matrix F in equation 3.8 is fixed throughout the N trials, the scalar λ^2 varies on a single-trial basis and is estimated, independently trial-by-trial, by the so-called discrepancy criterion (Twomey, 1965). The optimally fil-

tered trial in the sense of minimum variance estimation is thus:

$$\hat{u} = (A^T A + \gamma F^T F)^{-1} A^T A\, y_c \tag{3.9}$$

where $\gamma = \sigma^2/\lambda^2$ (Fig. 3.1.1).

In order to remove trials irremediably affected by motion artifacts, for each vector $\hat{u_j}$ the difference d_j between its maximum and minimum is considered:

$$d_j = \max(\hat{u_j}) - \min(\hat{u_j}) \tag{3.10}$$

Vectors characterized by a difference d_j greater than the average of the d_js $\pm$ 2.5 SDs are discarded (~10%). The estimated mean HR $\bar{u}$ for the given channel is obtained from the average of the N_1 trials filtered as in equation 3.9, which remain after the artifact removal procedure above, belonging to the same stimulus type:

$$\bar{u} = \frac{\sum_{j=1}^{N_1} \hat{u_j}}{N_1} \tag{3.11}$$

To further reduce high frequency residual oscillations and facilitate later peak amplitude and latency determination, $\bar{u}$ is then smoothed with a Savitzky-Golay filter with 3rd polynomial order and frame size equal to 25 time-points (3 s). Finally, $\bar{u}$ is baseline-corrected by subtracting its mean intensity in the 0-500 ms interval from the onset.

3.2 Literature methods used as reference in the comparison

In the following two paragraphs a brief description of the two widely used algorithms that will be used to validate the proposed methodology is presented. The first method (rCA, reference-channel based fNIRS data correction following Conventional Averaging) exploits the short-separation channel, while the second (CA, Conventional Averaging) does

not.

3.2.1 Reference-channel based fNIRS data correction following Conventional Averaging (rCA)

This technique is a two-step method, which first exploits the short-separation channel signal to correct fNIRS data and then resorts to conventional averaging to recover the hemodynamic response (Saager and Berger, 2005). This method has been chosen for comparison because it is the most general and simple method for HR estimation based on the SS-channel and, like the proposed method, does not require a model of the unknown stimulus-evoked HR. As done in ReMCoBA processing pipeline (paragraph 3.1), data are first pre-processed by band-pass filtering (Butterworth, pass band: from 0.01 Hz to 1.25 Hz (Zhang et al., 2009)). The upper cutoff frequency has been reduced from 3 to 1.25 Hz compared to ReMCoBA: such a choice allows to take into account the cardiac component facilitating the correlation analysis made below, while removing higher frequencies, which instead have not been removed in the preprocessing for ReMCoBA since the Bayesian approach can cope with them. Then, similarly to what has been done in section 3.1.1, for each standard channel, the SS-channel signal with the highest correlation is scaled to fit the former signal in a least-squares sense (Saager and Berger, 2005). If the correlation between the SS and standard channel signals is greater than 0.6, the scaled SS-channel signal is subtracted from the standard channel signal, otherwise no subtraction is performed, since doing so brings with it the potential of increasing noise consequently (Zhang et al., 2009). The obtained time-series is then segmented into trials and those belonging to the same condition are grouped. Trials with artifacts are discarded following the same criteria used in the section 3.1.2. After averaging all trials corresponding to the same condition, residual high frequency noise is reduced as in the section 3.1.2 by a Savitzky-Golay's filter with polynomial order equal to 3 and frame-size equal to 25 time-points (corresponding to 3 s). The HR estimate is finally obtained after a baseline-correction

done with the same strategy presented in section 3.1.2.

3.2.2 Conventional Averaging (CA)

The second method entails the same operations as that in section 3.2.1, but SS-channels are not used. For simplicity, it will be referenced to as conventional averaging, even if other pre-processing steps, such as band-pass filtering, are performed. Since differences in the results will be due to the use of the SS-channel only, the comparison CA vs. rCA can be exploited to quantitatively demonstrate the benefits of the use of the short-separation channel in HR estimation.

3.3 Data and indexes used for the assessment

3.3.1 Real data

Ten right-handed participants (5 females, mean age 28, from 24 to 37) performed the experiment after providing informed consent. Each participant was seated on a comfortable chair in a dimly lit room in front of a LCD monitor placed at a viewing distance of 60 cm. The index fingers of the right and left hands were placed on the ”A” and ”L” key respectively. Each trial began with a central fixation cross, followed 2 s later by a white arrow head pointing unpredictably and with equal probability to the right (Condition 1) or left (Condition 2) side of the monitor. Participants had to press the ”A” key twice if the white arrow pointed to the left, or the ”L” key twice if the white arrow pointed to the right. Each participant performed a total of 80 trials, which were organized in two consecutive sessions of 40 trials. An ISI (inter-stimulus interval) ranging from 12 to 15 s elapsed between consecutive trials. The choice of this double-press finger-tapping task was largely motivated by the expected small HR amplitude (Brigadoi et al., 2012; Cutini et al., 2008, 2011a) characterized however by well-established features replicated in several prior fNIRS studies (Franceschini et al., 2006; Holper et al., 2009; Leff et al., 2011; Lutz et al., 2005; Sato et al., 2007). No resting state intervals were

added between stimuli in order to reduce experimental time, thereby limiting phenomena like fatigue, habituation, and reduction in sustained attention influencing the participants' performance.

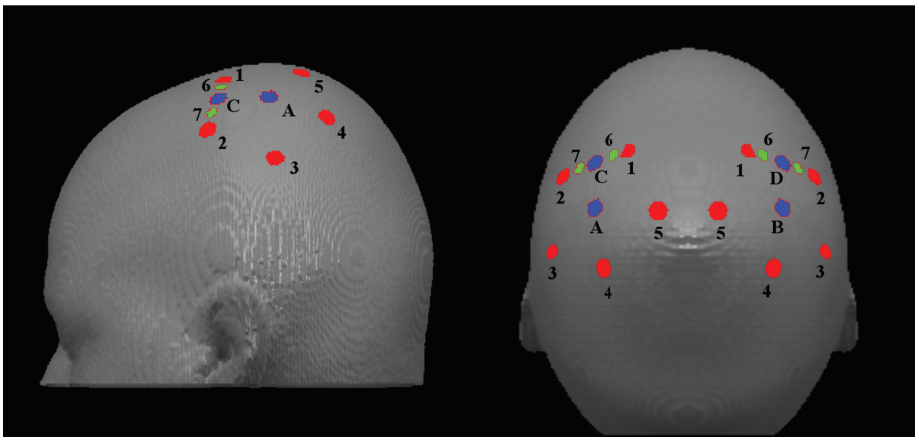

Figure 3.3.1: Probe placement: sources (red circles) and detectors (blue circles) overlaid on the head surface of the ICBM152 template. Green circles represent the sources of the SS-channels. Hence, C-6, C-7, D-6 and D-7 are the SS channels.

The fNIRS signal was acquired with a multi-channel frequency-domain NIR spectrometer (ISS ImagentTM, Champaign, Illinois), equipped with 32 laser diodes (16 emitting light at 690 nm, and 16 at 830 nm) and 4 photo-multiplier tubes. Sources and detectors were held in place on the scalp using a custom-made holder and velcro straps. Each source location comprised two source optical fibers, one for each wavelength. Sources and detectors were positioned using a probe-placement method based on a physical model of the ICBM152 template's head surface (Cutini et al., 2011b) and their position is illustrated in Fig. 3.3.1: detectors A and B were placed 1 cm behind C3 and C4 (according to the international 10-20 system), respectively. There were 10 standard channels (characterized by a source-detector distance of 3 cm): 1 (detector A - source 1), 2 (A-2), 3 (A-3), 4 (A-4), 5 (A-5) for the left and 6 (B-1), 7 (B-2), 8 (B-3), 9 (B-4), 10 (B-5) for the right hemisphere. In addition, there were 4 short-separation channels (characterized by a source-detector distance of 0.7 cm): 11 (C-6), 12 (C-7) for the left and 13 (D-6), 14 (D-7) for the right hemisphere. The

probe arrangement even provided 4 additional channels (sources 1 and 2 with detector C on the left hemisphere and sources 1 and 2 with detector D on the right hemisphere) with a source-detector distance equal to 1.5 cm: since they are too close to be considered as standard channels and, at the same time, too far to be considered as SS-channels, they are discarded from analyses. From each channel the signal relative to HbO and the corresponding signal relative to HbR is derived. To be noticed, only two SS-channels for each hemisphere were placed. The dataset for each channel contains about 12000 time-points, roughly corresponding to 25 min (1500 s). The sampling frequency was 7.8125 Hz.

A representative example of the signal acquired by a SS-channel and by a standard channel is reported in Fig. 3.3.2 a).

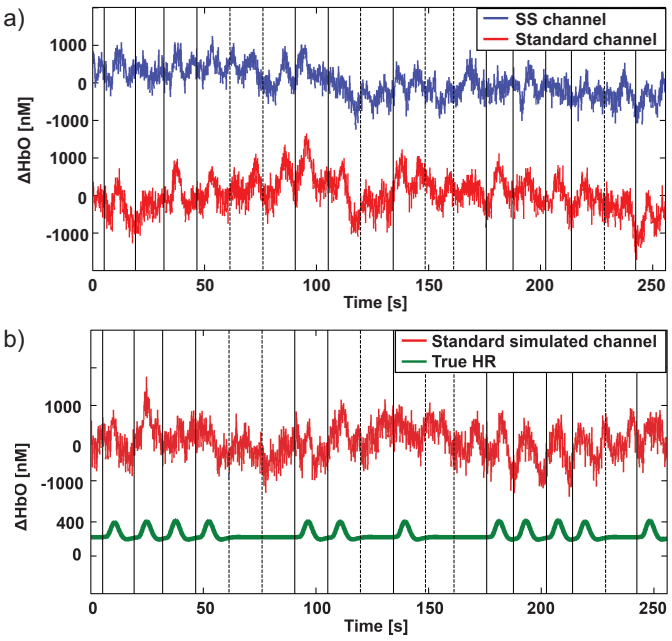

Figure 3.3.2: a) Representative examples of signal acquired at SS-channel (blue) and at standard channel (red). b) Synthetically generated standard channel time series (red line) and true HR (green line) in the synthetic dataset. The onset time is represented by a solid black vertical line for Condition 1, and by a dashed vertical line for Condition 2: it is the same for all represented signals in a) and b). The real signals reported in figure are relative to channels located in the left hemisphere, so in the reported simulated signal the HR was added only in correspondence of a stimulus relative to Condition 1.

3.3.2 SYNTHETIC DATA

Simulated datasets were generated so as to resemble as close as possible the characteristics of real data. For each of the 30 simulated subjects, 10 standard channels for HbO and the corresponding 10 channels for HbR were generated, in addition to 2 SS-channels for each hemisphere, for both HbO and HbR. Thus, there were a total of 14 channels for each type of hemoglobin.

Samples $y_{sim}(t)$ of each simulated channel were generated as:

$$y_{sim}(t) = k \cdot u_{true}(t) + \varphi_{sim}(t) + \eta(t) + r(t) \tag{3.12}$$

where $u_{true}(t)$ was the true HR and was multiplied by the constant k (which can be equal to 0, 0.5 or 1 depending on the channel; i.e., k is 0 in the SS-channels and halved in some standard channel, described below), $\varphi_{sim}(t)$ was the physiological noise term, $\eta(t)$ was the random noise, and $r(t)$ was a noise term due to possible motion artifacts.

The HR evoked by a single stimulus (t=0 corresponds to the presentation of the stimulus), was modeled by a linear combination of two gamma-variant functions Γ_n (Abdelnour and Huppert, 2009; Lindquist and Wager, 2007), time dependent, with a total of 6 variable parameters:

$$u_{true}(t) = \alpha \cdot [\Gamma_n(t, \tau_1, \rho_1) - \beta \cdot \Gamma_n(t, \tau_2, \rho_2)] \tag{3.13}$$

with

$$\Gamma_n(t, \tau_j, \rho_j) = \frac{1}{p!\,\tau_j} \left(\frac{t - \rho_j}{\tau_j} \right)^p e^{-(t-\rho_j)/\tau_j} \delta(t - \rho_j) \tag{3.14}$$

$$\delta(t - \rho_j) = \begin{cases} 1 & \text{if } t - \rho_j \geqslant 0 \\ 0 & \text{otherwise} \end{cases} \tag{3.15}$$

where α tuned the amplitude, τ_j and ρ_j tuned the response width and the onset time respectively, and β determined the ratio of the response to undershoot. The coefficient p was set to 5 following the nominative values reported in Glover (1999). In order to simulate the HR due to two

different stimuli and with shapes, amplitudes and latencies in agreement with previous findings regarding finger tapping tasks, two u_{true} profiles were generated by properly tuning the parameters in equation 3.13, allowing small variations in peak amplitude and latency between a trial and another. For HbO, this led to a first HR profile with a peak amplitude of 420±20 nM and a peak latency equal to 5.0±0.2 s, while the second HR profile had a peak amplitude of 360±20 nM and a peak latency equal to 5.5±0.2 s. The first profile was associated with Condition 1, the second with Condition 2. Note that HR amplitude was lower than that of physiological components (~400 nM vs ~2000 nM). 40 stimuli for each condition were simulated, with an ISI ranging between 12 and 15 s. The simulated HR u_{true} in equation 3.13 was added ($k = 1$) in channels 1, 4, 5 for Condition 1, and in channels 6, 9, 10 for Condition 2. In channels 2, 3, 7, 8 the amplitudes of the added HRs were halved ($k = 0.5$). In the other channels no HR was added ($k = 0$). Thus, there were 3 channels with full HR and 2 channels with halved HR in the left hemisphere for Condition 1 and the same in the right hemisphere for Condition 2.

Physiological noise $\varphi_{sim}(t)$ in equation 3.12 can be considered to be additive and modeled as a linear combination of sinusoids (Abdelnour and Huppert, 2009):

$$\varphi_{sim}(t) = \sum_{j=1}^{5} [A_j \sin(2\pi f_j t)] \tag{3.16}$$

Frequency f_j and amplitude A_j of each sinusoid varied in the channel, and were different between participants. They are reported in Table 3.3.1.

HbR channels were generated in the same way. According to our real data, for each component in equation 3.12, the sign was changed, a delay of 1 s was added, and all the amplitudes, except that of random noise, were reduced to 25%.

A representative example of the simulated signals is reported in Fig. 3.3.2 b), which also shows the true HR (u_{true}) which has been added in the synthetic signal. Note that real (Fig. 3.3.2 a)) and simulated (Fig. 3.3.2

Physiological components	Frequency (Hz)	Amplitude (nM)
Very low frequency	$f_1 = .002 \pm .0001$	$A_1 = 700 \pm 100$
Low frequency	$f_2 = .01 \pm .001$	$A_2 = 700 \pm 100$
Vasomotor	$f_3 = .07 \pm .04$	$A_3 = 400 \pm 10$
Respiratory	$f_4 = .2 \pm .03$	$A_4 = 200 \pm 10$
Cardiac	$f_5 = 1.1 \pm .1$	$A_5 = 400 \pm 10$

Table 3.3.1: Mean and standard deviation of frequency and amplitude of each physiological component used to create synthetic data.

b)) signals are dominated by physiological components and that their amplitude is greater than that of the true HR.

3.3.3 INDEXES USED FOR COMPARING METHODS PERFORMANCES

In order to quantitatively assess the performance of the three methods and the impact of the SS-channel in synthetic data, four quantitative accuracy indexes, E_{HR}, E_A, E_L and E_D were defined as follows. E_{HR} is a percentage estimation error index, defined as:

$$E_{HR} = 100 * \frac{\|u_{true} - \bar{u}\|^2}{\|u_{true}\|^2} \tag{3.17}$$

where u_{true} and $\bar{u}$ are the true and the estimated HR, respectively. Indexes E_A and E_L were used to describe the error in estimating crucial HR parameters such as peak amplitude and latency and were defined as:

$$E_A = 100 * \frac{|A_{true} - A|}{|A_{true}|} \tag{3.18}$$

$$E_L = 100 * \frac{|L_{true} - L|}{|L_{true}|} \tag{3.19}$$

where A_{true} and L_{true} are the peak amplitude and latency of the true HR, while A and L are those of the estimated HR. Finally, index E_D, defined as:

$$E_D = 100 * \sqrt{E_A^2 + E_L^2} \tag{3.20}$$

was used to assess the accuracy in estimating both amplitude and la-

tency at the same time.

3.4 RESULTS

In this section, ReMCoBA is compared with rCA and CA by using synthetic and real data. For the sake of completeness, the results obtained by HR peak amplitudes analyses on the different activation in each hemisphere induced by each condition are also reported, in line with previous findings of the literature regarding finger-tapping tasks.

3.4.1 SYNTHETIC DATA

Fig. 3.4.1 a) shows a representative example of synthetically generated HR (black line) estimated by ReMCoBA (green line), rCA (blue line) and CA (red line). Qualitatively, the ReMCoBA profile seems closer to the true profile than the rCA and the CA ones. Also, of note is that the rCA profile seems more accurate than CA. Similar results were obtained for all the other synthetic subjects.

3.4.1.1 PERFORMANCE INDEXES RESULTS

To quantitatively compare ReMCoBA, rCA and CA, the four indexes defined in paragraph 3.3.3 have been computed for each of the 30 simulated participants. The mean value of the 30 participants and its standard deviation are reported in Fig. 3.4.2. Channels with full HR (peak amplitude equal to 400 nM) and channels with halved HR (peak amplitude equal to 200 nM) were kept separately. Notably, the best E_{HR} was obtained with ReMCoBA. In the case of entire HR (peak amplitude equal to 400 nM), ReMCoBA reduced the estimation error by 16.14% and by 50.54% for HbO, and 10.92% and 17.10% for HbR relative to rCA and CA, respectively. In the case of halved HR (peak amplitude equal to 200 nM), ReMCoBA reduced the estimation error of 13.20% and 49.44% for HbO and 19.57% and 24.48% for HbR with respect to rCA and CA respectively.

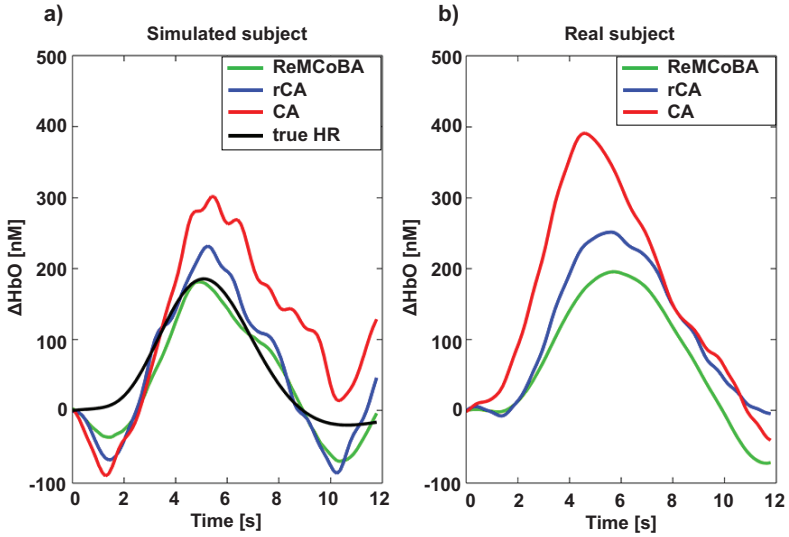

Figure 3.4.1: Representative examples of the estimated mean HRs for a given subject and channel by the proposed method (ReMCoBA) (green), by rCA (blue) and by CA (red), on a) simulated data and b) real data. On simulated data the true HR (black line) is also shown.

Similarly, ReMCoBA reduced E_A, E_L, as well as E_D. The higher values of the error in the HbR case are due to its smaller amplitude compared to HbO (it is reduced to 25%); thus, the HR in the acquired signal has a smaller signal-to-noise ratio (SNR), and its estimation is consequently more difficult compared with the HbO case. For the same reason, error indexes have greater values in the case of halved HR. The best values, for all indexes, obtained by rCA with respect to CA, underline the benefits provided by the use of the SS-channel in HR estimation. Values of each index for both HbO and HbR were submitted to separate repeated measures ANOVAs with method (ReMCoBA, rCA and CA) and amplitude (full vs. halved) as within-subject factors. All ANOVAs revealed a main effect of the method (for details, see Table 3.4.1). The performance of the different methods as measured with the different indexes has been compared with a series of paired t-tests: statistically significant differences are indicated by gray ($p<.05$) and black ($p<.01$) horizontal lines over the corresponding bars in Fig. 3.4.2. Remarkably, the ReMCoBA obtained the best performance for all indexes and conditions, with a significant

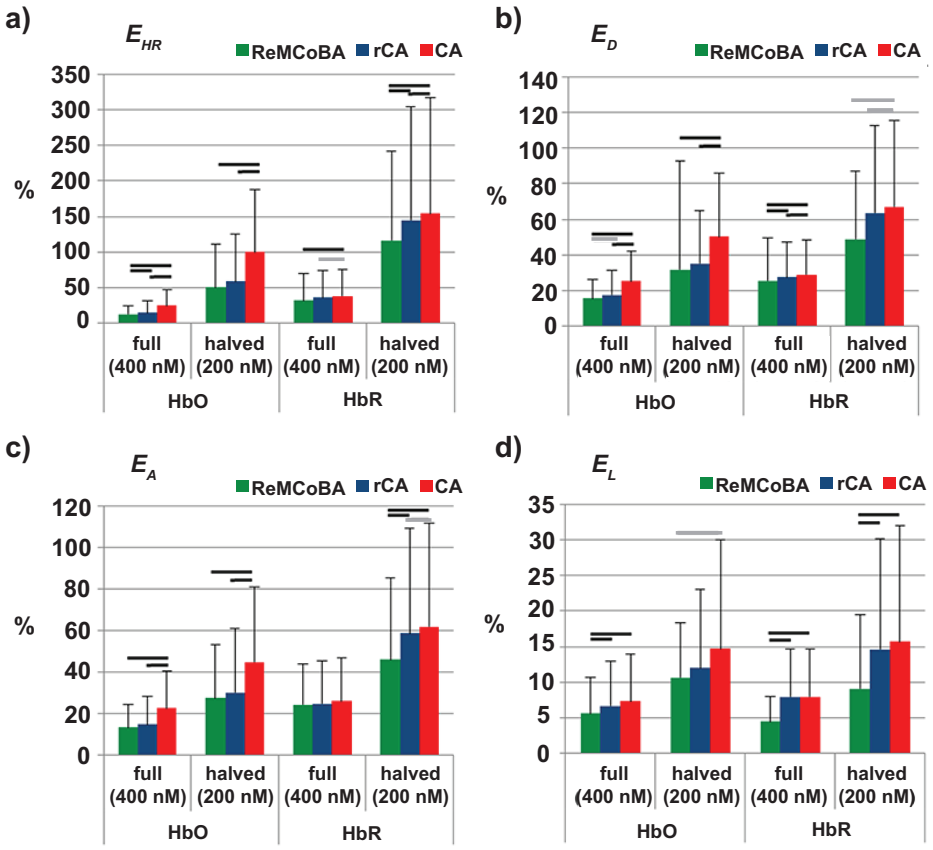

Figure 3.4.2: a) Estimation error (E_{HR}), b) Euclidean distance between estimated and true peak (E_D), c) error on peak amplitude (E_A) and d) error on peak latency (E_L). Means and standard deviations computed across all simulated participants. Statistical differences between the three methods are indicated by a gray ($p<.05$) or black ($p<.01$) horizontal line over the corresponding bars. Evoked hemodynamic responses with peak amplitude equal to 400 nM (full) and 200 nM (halved) are analyzed separately, as well as HbO and HbR responses.

difference in most cases.

	Method				Amplitude				Method*Amplitude			
	HbO		HbR		HbO		HbR		HbO		HbR	
	F(2,58)	p	F(2,58)	p	F(1,29)	p	F(1,29)	p	F(2,58)	p	F(2,58)	p
E_{HR}	54.3	<.001	15.5	<.001	63.8	<.001	74.1	<.001	23.7	<.001	11.5	<.001
E_D	36.9	<.001	19.5	<.001	69.3	<.001	64.3	<.001	7.8	=.001	12.8	<.001
E_A	32.1	<.001	11.4	<.001	50.2	<.001	49.7	<.001	5	=.01	10.8	<.001
E_L	6.4	=.003	26.4	<.001	36	<.001	49.2	<.001	1.9	<.159	3.1	=.053

Table 3.4.1: Results obtained by repeated measures ANOVAs on simulated data, considering method (ReMCoBA, rCA and CA) and amplitude (full vs. halved) as within-subject factors, for estimation error (E_{HR}), Euclidean distance between estimated and true peak (E_D), error on peak amplitude (E_A), error on peak latency (E_L).

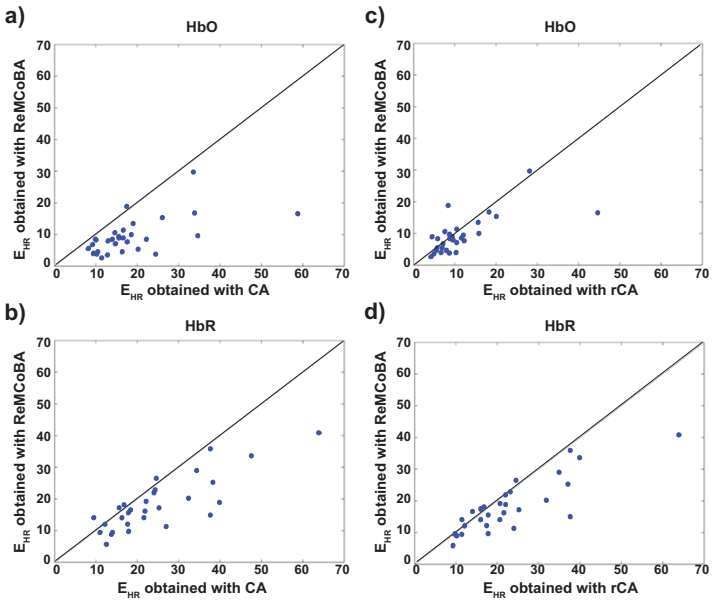

Figure 3.4.3: a) and b) Estimation errors (E_{HR}) obtained with CA (horizontal axis) and ReMCoBA (vertical axis), for HbO and HbR, respectively. c) and d) Estimation errors (E_{HR}) obtained with rCA (horizontal axis) and ReMCoBA (vertical axis), for HbO and HbR, respectively. Each dot is the mean E_{HR} obtained from channels relative to the same simulated subject.

Additional analyses for the simulated data were performed to quantitatively compare the performance of ReMCoBA with the other two meth-

ods (CA and rCA). The estimation error (E_{HR}), the most important index among those presented above, since it considers the difference in the whole profile between true and estimated HR, was used to objectively compare the methods on a single channel basis. With respect to CA, ReMCoBA improved E_{HR} in 84% of the simulated channels for HbO, and 70% for HbR. With respect to rCA, ReMCoBA improved E_{HR} in 58% of the simulated channels for HbO, and 61% for HbR. Results are reported in Fig. 3.4.3: 300 points should be displayed (30 subjects each for 10 channels) but for the sake of clarity each subject is represented by one dot, where this dot is the mean E_{HR} of all his channels. While the performances of ReMCoBA and CA are markedly different, with a significant reduction of E_{HR} obtained by ReMCoBA, the improvement obtained by ReMCoBA with respect to rCA is clear but less apparent, in line with results shown in Fig. 3.4.2 a).

Fig. 3.4.4, instead, demonstrates the importance of the selection of the SS-channel in order to correctly estimate the HR. It shows the percentage difference of the estimation error obtained with and without the use of the SS-channel in relation to the Pearson's correlation coefficient during the resting period. In agreement with Zhang et al. (2009), data in Fig. 3.4.4 suggest a correlation coefficient threshold of approximately 0.6: when the correlation coefficient is lower than 0.6, the obtained estimation error increases in 50% of channels and in some cases it drastically increases (three and even four times) with respect to the estimation error obtained without the use of the SS-channel.

3.4.1.2 ROC ANALYSES

A ROC analysis was performed to test the performance of the methods considered in the present context following the systematic variation of SNR values (Machado et al., 2011). HRs from all simulated subjects were split in order to obtain a subset of active HRs with a full HR amplitude (~400 nM) and a subset of non-active HRs with HR true amplitude equal to 0. For HbO, HRs derived by channels 1, 4, 5 in Condition 1 and chan-

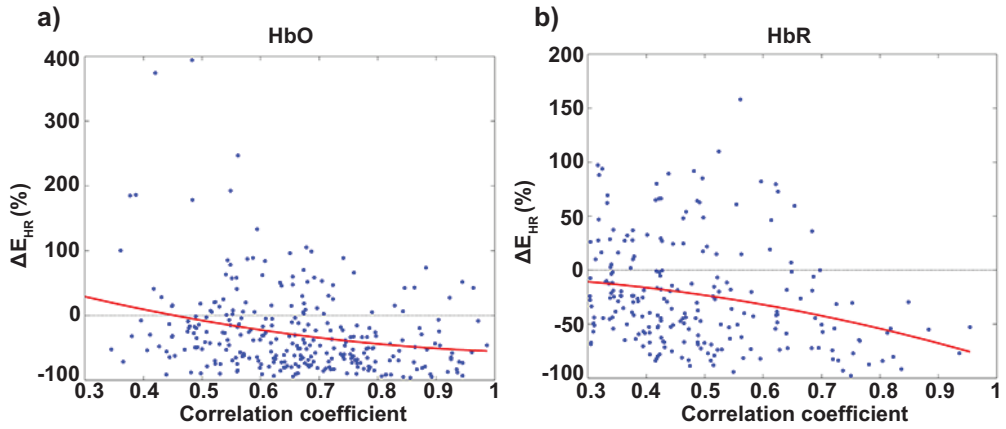

Figure 3.4.4: Percentage difference of the estimation error obtained with and without the use of the SS-channel ($\Delta E_{HR} = 100*(E_{HRwith} - E_{HRwithout})/(E_{HRwithout})$) in relation to the Pearson's correlation coefficient during the resting period (from 0.3 to 1), for a) HbO and b) HbR. Red lines represent the second order polynomial fit.

nels 6, 9, 10 in Condition 2 were treated as active HRs, whereas HRs derived by channels 6, 9, 10 in Condition 1 and channels 1, 4, 5 in Condition 2 were treated as non-active HRs. An analogous subdivision was applied on channels with halved HR (~200 nM). In this latter case, for HbO, HRs derived by channels 2 and 3 for Condition 1 and channels 7 and 8 for Condition 2 were treated as active HRs, and HRs derived by channels 7 and 8 in Condition 1 and channels 2 and 3 in Condition 2 were treated as non-active HRs. HbR underwent the same procedure. Full and halved HRs led to two different SNRs, whose values were -17 dB (full HR) and -23 dB (halved HR) for HbO, and -20 dB (full HR) and -26 dB (halved HR) for HbR.

	HbO		HbR	
	Full HR	Halved HR	Full HR	Halved HR
ReMCoBA	.9777	.8535	.9272	.7780
rCA	.9679	.8621	.9052	.7689
CA	.9390	.7847	.8934	.7556

Table 3.4.2: Area under curve (AUC) obtained by each method (ReMCoBA, rCA and CA) in the ROC analysis in case of full HR (~400 nM) and halved HR (~200 nM), for HbO and HbR.

In order to provide parameters reflecting a substantial portion of the HR function, and not only of the peak amplitude, an area subtended by the HR curve in a 4 s interval centered at the peak's latency was considered. A threshold was set on the value of the 4 s area to enable the separation of true from false positive rates. The threshold value was then varied from the greatest area, where neither true nor false positives were found, to the lowest area, where the concentration of true and false positives was assumed to be maximal. A total of four cases were generated for the analyses, each contributing 200 points. Table 3.4.2 reports the values of the area under the curve (AUC) estimated using the present ROC approach. The results of the ROC analyses are illustrated in Figs. 3.4.5. The results from the different methods were compared via a series of paired two-tailed t-tests on the individual AUC values. Significant differences were found in HbO (full HR) between ReMCoBA and CA ($t(29) = 2.041$, $p = .05$), in HbO (halved HR) between rCA and CA ($t(29) = 2.371$, $p<.05$), and between both ReMCoBA and rCA ($t(29) = 2.948$, $p<.05$) and ReMCoBA and CA ($t(29) = 2.916$, $p<.05$) in HbR (full HR). No other significant difference was detected in the comparison. In line with the results described in the foregoing sections, the ROC analyses corroborated the remarkable superior performance of ReMCoBA relative to CA. Albeit with slightly less power, the results of the ROC analyses - and the particularly clear pattern visible in Fig. 3.4.5 - allows to argue that ReMCoBA performed better than rCA (and particularly so in the case of HbR, full HR), given the highest AUC value obtained by ReMCoBA vs. rCA in three out of the four tests.

3.4.1.3 Precision of ReMCoBA HR estimation

Additional analyses were performed on the precision of the HR estimates provided by ReMCoBA. The number of parameters used by the proposed method ranges between 10 and 16 (depending on M), if the SS-channel is used, while it is 5 otherwise. This number is of the same order of that of previously published methods, e.g. at least 6 parameters in Prince et al.

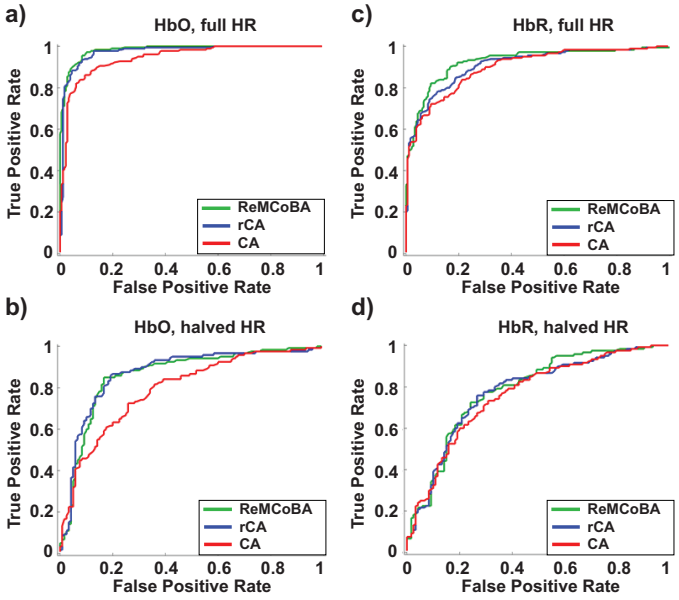

Figure 3.4.5: ROC curves obtained by ReMCoBA (green), rCA (blue) and CA (red) in the case of a) HbO, full HR, b) HbO, halved HR, c) HbR, full HR and d) HbR, halved HR. Full HR (∼400 nM) and halved HR (∼200 nM) denote two different SNRs, about -17 dB and -23 dB respectively for HbO, and -20 dB and -26 dB for HbR.

(2003), 8 parameters in Abdelnour and Huppert (2009), 16 parameters in Gagnon et al. (2011). A lower number of parameters would not be able to describe the complexity of the fNIRS signal shown by the data, resulting in a biased description of noise and in suboptimal HR estimates. Indeed, the presented procedure tries to minimize model complexity by letting the data indicate the most suited model order. For instance, M in equation 3.4 can be 1, 2 or 3, depending on the data, while in other methods (e.g. (Prince et al., 2003)) M is identically equal to 3 for all the trials (with consequent risk of overfitting). Similarly, the order 4 for the auto-regressive model was determined by AIC. In general, an aspect of strength of ReMCoBA is that the values of all the employed parameters are computed by objective and reproducible (even if, sometimes, empirical to some extent) procedures, the aim being to reduce possible user's subjectivity as much as possible.

In order to have a quantification of the precision of the HR estimates

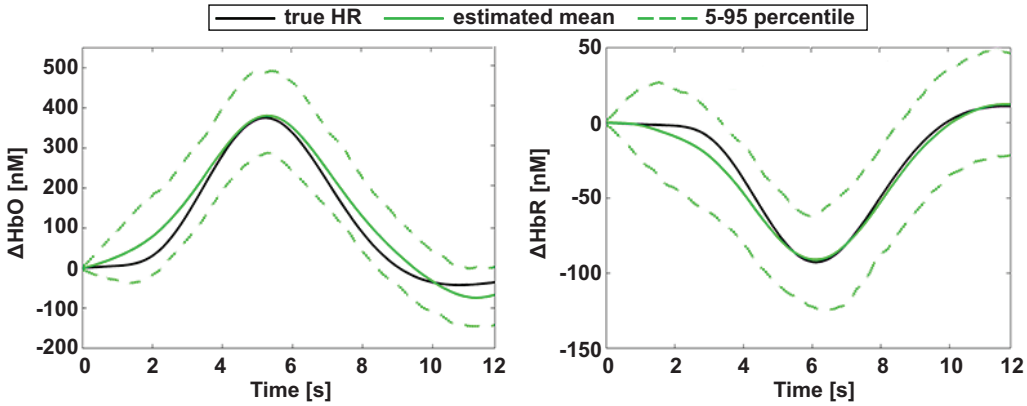

Figure 3.4.6: Monte Carlo estimates: true HR (black line), estimated mean (green line) obtained by 200 realizations of a channel with different random noise, 5th and 95th percentiles (dotted green line), for HbO (left) and HbR (right).

obtained by ReMCoBA, a Monte Carlo simulation was performed. For each simulated subject, 200 realizations of the same channel were created, each with a different random noise sequence ($\eta(t)$ in equation 3.12). From each of these 200 realizations, the HR was estimated. From the sample distribution of the estimates, the average and the 5th and 95th percentile variability bands were finally computed. As shown in Fig. 3.4.6, the bias was very small. The fact that the variability band was narrow indicates that the procedure was not overly sensitive to noise, as it would happen if models were overfitting the data. In particular, the mean variance of E_{HR} was equal to 2.3% for HbO and 5.1% for HbR, denoting the good precision of the estimates obtained by ReMCoBA.

3.4.2 Real data

A representative example of the HR obtained in a real subject is reported in Fig. 3.4.1 b). On this particular dataset, all methods achieved a reasonable HR estimation. However, differences in peak amplitude and latency were apparent. Obviously, in the real data case a quantitative/objective assessment of the three HR estimation algorithms was more difficult to be done than in the simulated data case. The following strategy has been considered. First, samples of each estimated HR were fitted by the

canonic mathematical model of the HR, equation 3.13, by a nonlinear least squares algorithm (initial values of the parameters, i.e., $\alpha = 1202$, $\varphi_1 = 0.5$, $\varphi_2 = 3.5$, $\tau_1 = \tau_2 = 0.8$ and $\beta = 0.6$, were derived by an overall average of all real participants and channels). The fit was then computed on each estimated HR with lower and upper constraints on the model's parameters ($0 \leqslant \alpha < inf$, $-1.5 < \varphi_1 < 1.5$, $2.5 < \varphi_2 < 5.5$, $0.5 < \tau_i < 0.9$ and $0 < \beta < 0.7$). The constraints on amplitude (α) and time delay (φ_i) were set to take into account the possible variability between participants and channels, and in order to obtain a good fit only if the estimated HR had a reasonable physiological shape (Fig. 3.4.7). Stringent constraints were set, instead, to the parameters (τ_i) which tuned the shape of the HR and to the amplitude of the undershoot (β). The coefficients of the fit (R^2, $rmse$) were used to have a grasp of the "likelihood" of the estimated HR.

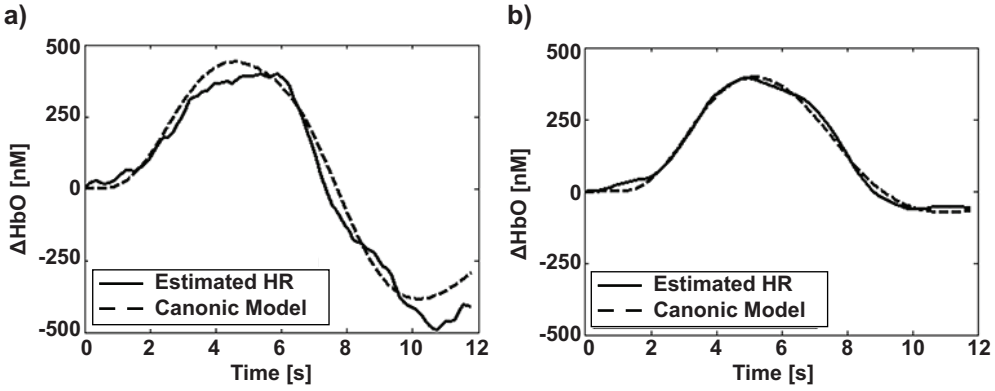

Figure 3.4.7: Representative examples of canonic mathematical model of the hemodynamic response (dashed line) fitted to real data estimated HR (solid line). a) The model cannot properly fit the estimated HR because of the presence of an unrealistic undershoot, whose amplitude is greater than that of the peak, probably due to the presence of physiological noise not yet removed by the signal processing method ($R^2 = .96$, $rmse = 44$). b) The estimated HR has a reasonable physiological shape and it is well described by the canonic model ($R^2 = .99$, $rmse = 15$).

For each index, a mean value was obtained by each of the 10 real participants. For each method, the mean value of the 10 participants and its standard deviation are reported in Fig. 3.4.8. All methods achieved good results on the Pearson's correlation coefficient (R^2), ∼.9 and ∼.8 for HbO

and HbR respectively. Values were submitted to a repeated measures ANOVA, considering method as within-subject factor, for both HbO and HbR. ANOVAs revealed a significant effect of the method (Table 3.4.3). Hence, a paired t-test was conducted between methods. Statistical differences between the three methods are indicated by gray ($p<.05$) and black ($p<.01$) horizontal lines over the corresponding bars in Fig. 3.4.8. The proposed method achieved the best R^2, with a significant difference with respect to CA for HbO, and to rCA and CA for HbR. The same analyses were conducted on the root mean square error ($rmse$) and the new methodology achieved the lowest $rmse$, with a significant difference ($p<.05$) with respect to rCA and CA, for both HbO and HbR. Again, the best values, for both R^2 and $rmse$, obtained by rCA with respect to that obtained by CA, underline the benefits provided by the use of the SS channel in HR estimation.

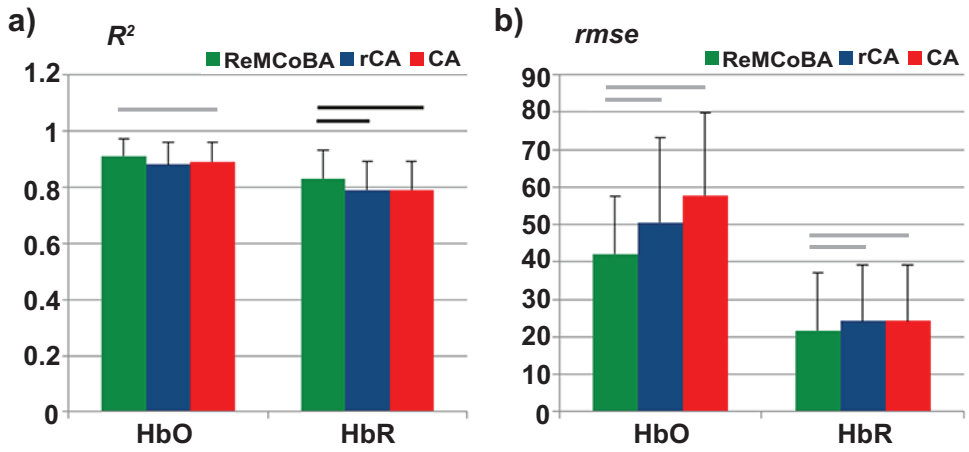

Figure 3.4.8: a) Pearson's correlation coefficients (R^2) and b) root mean square errors ($rmse$) between estimated hemodynamic responses and the canonic model of the hemodynamic response. Means and standard deviations are computed across all real participants. Statistical differences between the three methods are indicated by a gray ($p<.05$) or black ($p<.01$) horizontal line over the corresponding bars.

	HbO		HbR	
	F(2,18)	p	F(2,18)	p
R^2	4.0	= .036	14.5	< .001
rmse	5.9	= .011	6.6	= .007

Table 3.4.3: Results obtained by repeated measures ANOVAs, considering method (ReMCoBA, rCA and CA) as within-subject factor, for the Pearson's correlation coefficients (R^2) and the root mean square errors ($rmse$) between estimated real data hemodynamic responses and the canonic model of the hemodynamic response.

3.4.3 Investigation of differences between hemispheres and conditions

In order to demonstrate the effectiveness of the applied methodologies, hemodynamic responses estimated by the proposed method (ReMCoBA) and by the methods used for comparison (rCA and CA) were analyzed to confirm previous findings known by literature regarding finger-tapping tasks. The standard investigation of fNIRS data consists in the analysis of HR's peak amplitudes. Note that, on simulated data, the whole HRs and in particular their peak amplitudes and peak latencies were created according to information known by literature. Since we were not interested in the HR obtained by each single channel but in differences between conditions and hemispheres, all channels of the same hemisphere were grouped, while the two conditions have been kept separated. Then, peak amplitudes of each channel in both conditions have been analyzed in order to find significant differences between hemispheres and conditions. The mean peak amplitude of every participant obtained grouping channels by hemisphere and condition (e.g. mean value of the channels of the right hemisphere in Condition 1) was considered. The values obtained with the three methods (reported in Fig. 3.4.9 for both real and simulated data scenario) have been separately submitted to a repeated measures ANOVA, with condition (right- vs. left-hand tapping) and hemisphere (left vs. right) as within-subject factors.

Although all the ANOVAs revealed a significant interaction between hemisphere and condition for all methods in the simulated data scenario

	Hemisphere				Condition				Hemisphere*Condition			
	HbO		HbR		HbO		HbR		HbO		HbR	
	F(1,29)	p	F(1,29)	p	F(1,29)	p	F(1,29)	p	F(1,29)	p	FF(1,29)	p
ReMCoBA	16.3	<.001	10.2	=.003	2.6	=.115	.712	=.406	3155.6	<.001	841.8	<.001
rCA	15.2	=.001	11.2	=.002	3.7	=.065	4.1	=.053	1914.6	<.001	892.0	<.001
CA	9.7	=.004	10.7	=.003	1.5	=.234	4.8	<.036	1039.3	<.001	818.8	<.001

Table 3.4.4: Simulated data scenario. Results obtained by repeated measures ANOVAs, with condition (right- vs. left-hand tapping) and hemisphere (left vs. right) as within-subjects factors, for ReMCoBA, rCA and CA. The mean peak amplitude of every participant obtained grouping channels by hemisphere and condition was considered.

(Table 3.4.4), the HRs estimated with the proposed method were the closest to the real values (336 nM for Condition 1 in the left hemisphere and 288 nM for Condition 2 in the right hemisphere for HbO, and -88 nM for Condition 1 in the left hemisphere and -72 nM for Condition 2 in the right hemisphere for HbR). Also in the real data case, for each method, ANOVAs revealed a significant interaction between hemisphere and condition (Table 3.4.5). In real data, hemodynamic activity was observed both contralaterally and ipsilaterally to the moved forefinger. Anyway, as expected, the amplitude of the HRs was greater in the contralateral hemisphere, without reaching significance, though. Instead, a significant difference between hemispheres was found on simulated data, but (unlike real data) HR was added contralaterally only. Equivalent outcomes are found for HbR. All the results obtained in real data are in line with previous findings concerning finger tapping protocols (Franceschini et al., 2006; Holper et al., 2009; Leff et al., 2011; Lutz et al., 2005; Sato et al., 2007).

3.5 Considerations and conclusive remarks

In the present chapter, a methodology to improve the estimation of HR from fNIRS signals has been presented. The new algorithm is a two-step method with no assumption on HR shape, duration, amplitude and latency, or on the kind of experiment and stimulus. In the first step,

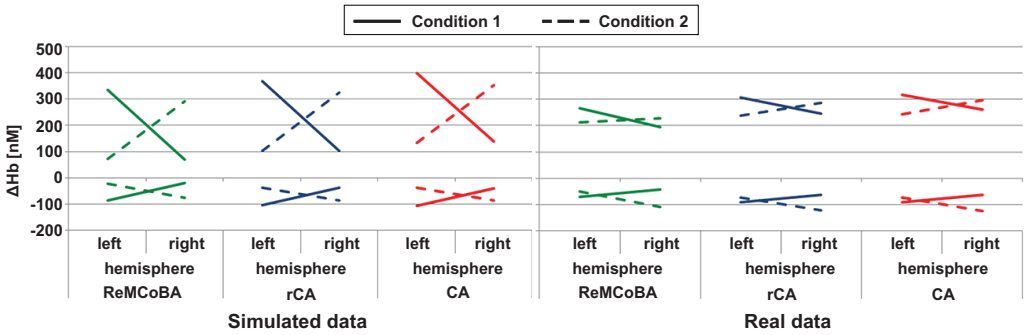

Figure 3.4.9: Mean values of the peak amplitude (for both HbO and HbR) obtained for each condition (movement of the right or left forefinger for Condition 1 and Condition 2 respectively) and hemisphere (left or right) by the three methods (Condition 1 is represented by a solid line, Condition 2 is represented by a dashed line). Mean values are computed across all participants. On the left, simulated data scenario while on the right real data scenario.

	Hemisphere				Condition				Hemisphere*Condition			
	HbO		HbR		HbO		HbR		HbO		HbR	
	F(1,29)	p	F(1,29)	p	F(1,29)	p	F(1,29)	p	F(1,29)	p	FF(1,29)	p
ReMCoBA	.804	=.393	2.6	=.142	.194	=.67	7.2	=.025	6.3	=.033	12.0	=.007
rCA	.033	=.86	1.4	=.269	.289	=.604	6.2	=.035	16.5	=.003	14.0	=.005
CA	.003	=.955	2.0	=.194	.584	=.464	6.9	=.028	16.8	=.003	13.7	=.005

Table 3.4.5: Real data scenario. Results obtained by repeated measures ANOVAs, with condition (right- vs. left-hand tapping) and hemisphere (left vs. right) as within-subjects factors, for the proposed method (ReMCoBA), rCA and CA. The mean peak amplitude of every participant obtained grouping channels by hemisphere and condition was considered.

ReMCoBA takes advantage from the availability of noise-only data, acquired with a short-separation channel, which allows a massive reduction of physiological noise (due to respiration, vasomotor waves, etc.) disturbing HR estimation from standard channels. To perform Step 1, a good correlation between SS and standard channel is necessary, otherwise physiological noise may be amplified instead of reduced (Fig. 3.4.4). Step 2 embeds a non-parametric (i.e., no assumptions on shape, amplitude and latency) Bayesian approach, which is able to individuate, on a trial-by-trial basis, a suitable compromise between measured noisy data and a priori expectations on HR smoothness. Step 1 and 2 take into account the complexity of fNIRS signal, letting the data indicate the most

suited model order and parameter values.

The comparison of ReMCoBA and rCA reveals a significant improvement in HR estimation (with a statistically significant difference for all accuracy indexes detectable in simulated data). The fact that CA leads to the worst HR estimates supports the importance of the SS-channel. The superior performance of ReMCoBA over the other two methods has been confirmed by the results of ROC analyses considering full and halved HRs in both conditions and for each subject estimated based on both HbO and HbR concentration indices. Notably, as regards real data, a finger-tapping task has been used, instead of using a more sophisticated paradigm, so that to obtain a known HR. In this way, an ideal platform to compare the performance of the three methods straightforwardly has been provided.

Given that the total number of channels available in NIRS devices is typically limited, the use of only two SS-channels for hemisphere is an important achievement of the proposed method. There is ample evidence in the literature that low frequency physiological fluctuations are highly correlated across space, with some relatively constant time delay across time (Cooper et al., 2012a; Frederick et al., 2012; Tong and Frederick, 2010; Tong et al., 2011). To note, however, that other studies found instead a spatial inhomogeneity of physiological noise (Gagnon et al., 2012a). Even if the Pearson's correlation coefficient between SS and standard channel is generally greater if they are close to each other ($<$2 cm) (Gagnon et al., 2012a), a good correlation ($>$0.6) also between distant channels has been found, even from those located in different hemispheres: the model of physiological components is derived by the SS-channel with the greatest correlation coefficient with the considered standard channel, and 45% of the selected SS-channels were located in the opposite hemisphere. However, just because their number is limited, it is important to maximize the SNR of the signal acquired by SS-channels, so special attention must be paid on their location (in order to minimize the distance from standard channels) and on a perfect contact between optic fibers and the participant's skin. Furthermore, the distance between source and detector of

each SS-channel must be less than 1 cm, in order to measure the signal relative to scalp and skull only. If the distance is greater than 1 cm, part of the acquired signal is relative to the cerebral cortex and may contain the stimulus-evoked hemodynamic response.

Simulated and real data, on which the new method has been tested on, comprised two conditions, each consisting in the repetition of an identical stimulus. In order to find out the minimum number of repetitions (trials) needed to obtain a good HR, the HR using 30, 40 (so far discussed), 50 trials was estimated and the corresponding estimation error on simulated data was evaluated. No significant difference was found in the estimation of the event-related hemodynamic response between 40 and 50 trials (for HbO, E_{HR} was equal to 12.2% and 10.2% respectively; for HbR, E_{HR} was equal to 31.9% and 21.7% respectively), but a significantly greater estimation error was found in the 30 trials case (E_{HR} was equal to 18.6% for HbO and 43.8% for HbR). Thus, when the signal is dominated by physiological components, a minimum number of 40 trials seems to be mandatory for a correct estimation of HR in an event-related design.

In conclusion, the proposed method based on a model derived by the SS-channel provides a valuable estimation of the stimulus-evoked hemodynamic response, without a priori information about its shape, duration, amplitude, latency and no model of the unknown hemodynamic response is required. These features make the proposed method a general and flexible way to correctly estimate the evoked hemodynamic response.

4

Algorithms for motion correction in fNIRS data: A new strategy for their quantitative assessment on real data

4.1 Motion artifacts in fNIRS signals

Motion artifacts are a significant source of noise in many fNIRS experiments (Fig. 4.1.1). In order to properly estimate the HR, motion artifacts should be detected and removed. Despite this, there is no well-established method for their removal. Instead, functional trials of fNIRS data containing a motion artifact are often rejected completely. However, in most experimental circumstances the number of trials is limited, and multiple motion artifacts are rather frequent, particularly in challenging

populations, such as stroke patients and infants. Recently, many methods have been proposed to correct for motion artifacts, including principle component analysis (Zhang et al., 2005b), spline interpolation (Scholkmann et al., 2010), Kalman filtering (Izzetoglu et al., 2010), wavelet filtering (Molavi and Dumont, 2012) and correlation-based signal improvement (Cui et al., 2010). These techniques will be briefly reviewed in section 4.3.

The performance of literature motion correction techniques has been often compared in simulations, but only rarely on real data. In this chapter, we perform this comparison on real fNIRS data acquired during a cognitive task, which required the participant to speak aloud, leading to a low-frequency, low-amplitude motion artifact that is correlated with the hemodynamic response. These characteristics make artifact detection and correction especially challenging. In most cases to date, motion correction techniques have been tested, with great success, on high frequency spike artifacts occurring randomly throughout the data-series, but their ability to isolate and correct artifacts which more closely resemble normal physiological fNIRS signals has not been assessed. To compare the efficacy of these methods, objective metrics related to the physiology of the hemodynamic response have been derived. The analyses performed in this chapter can serve as a guide for others to objectively test the impact of different motion correction algorithms and therefore select the most appropriate for the analysis of their own fNIRS experiment (Brigadoi et al., 2014). Most of the analysis presented in this chapter has been performed using functions implemented in the Homer2 NIRS Processing package (Huppert et al., 2009), which is freely available on line to all users. Furthermore, all the techniques for motion correction presented here have been implemented into this package, and are thus available to all users.

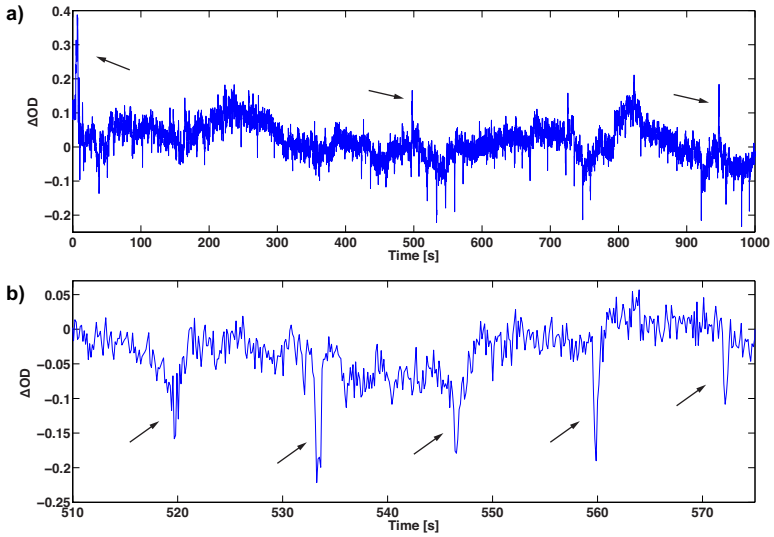

Figure 4.1.1: Example of time series corrupted by motion artifacts. a) Total time series and b) a zoom of the time series in a) in the 510-575 s time window. In a) high frequency artifacts are easily noted (black arrows) while in b) slower and more difficult to detect artifacts can be appreciated (black arrows). Note how slower and lower amplitude artifacts seen in b) are difficulty seen in a).

4.2 Classification of approaches to deal with motion artifacts

Motion artifacts can have different shapes, frequency content and timing. They can be high amplitude, high frequency spikes, easily detectable in the data-series or they can have lower frequency content and be harder to distinguish from normal hemodynamic fNIRS signals (Fig. 4.1.1). Motion artifacts can be generally classified into three categories, spikes, baseline shifts and low-frequency variations. They can be isolated events or they can be temporally correlated with the HR. Therefore, it is likely that the efficacy of each motion artifact correction technique will vary with the type of motion artifact and that the best technique to apply is data-dependent.

As previously stated, there are two different ways to solve the issue of motion artifacts, to reject them or to correct for them.

4.2.1 Correction vs. rejection

A common and simple way to solve the issue of motion artifacts is, therefore, to reject all trials where a motion artifact has been detected. However, this approach is only suitable if the number of motion artifacts detected is low and the number of trials is high, otherwise the risk is that too few trials will be accepted, resulting in a very noisy hemodynamic response. fNIRS is particularly suited for examining challenging populations (e.g. infants, clinical patients, children) who might not be easily investigated with fMRI. However, in these populations the number of functional trials is almost always strictly limited, and therefore trial rejection might not be feasible.

Several methods have thus been proposed to solve this issue correcting for motion artifacts instead of rejecting them. Some methods require a complementary measure of the motion artifact to aid in its removal, e.g. with a short-separation fNIRS channel (Robertson et al., 2010), or with an accelerometer (Virtanen et al., 2011). Others rely on the inherent changes in the amplitude and frequency of the data due to the artifact and act as post-processing techniques. The latter group does not require a complementary measure and thus can be used with every experimental paradigm, making it the most general solution. Hence, the techniques chosen for the proposed comparison fall inside this latter group, in order to allow every set of data to be submitted to the proposed objective approach for motion correction technique selection.

Hence, even if rejection is surely the simplest technique able to deal with motion artifacts and probably the most used one, many times it is impossible to apply it, because of the high presence of artifacts and the restricted number of trials. On the contrary, motion correction techniques do not suffer from these limitations, but have other disadvantages, e.g. they are somehow changing the signal under examination. Therefore, motion correction techniques should also be compared with the rejection technique and with the results obtained by simply including all trials and ignoring the motion artifact altogether, to see whether correcting for mo-

tion artifacts improves or not the quality of the signal in comparison with standard approaches that do not modify the signal.

4.2.2 Assessment of the performance of motion-correction algorithms

One way to estimate the performance of a motion correction technique or to compare different techniques is to simulate motion artifacts (Scholkmann et al., 2010) or to ask participants to move their head purposely to create a motion artifact (Izzetoglu et al., 2010; Robertson et al., 2010). However, real motion artifacts are complex and variable, and thus difficult to simulate. Furthermore, motion artifacts are not only due to the movement of the head, but also due to the movement of the eyebrows or the jaw, for example. The most suitable approach to quantifying the performance of different motion artifact correction techniques is to use real, resting-state fNIRS data, which are contaminated with real motion artifacts, and add a simulated HR to these data (Cooper et al., 2012c). Knowing the true hemodynamic response, it is possible to compute the MSE (Mean-Squared Error) and the Pearson's Correlation Coefficient (R^2) between the simulated and the recovered HR, and hence to have a quantitative measure to compare the different performances.

The next step towards establishing a standard approach for the correction of motion artifacts in fNIRS data is to compare the performance of multiple motion correction approaches on real cognitive data.

4.3 Literature algorithms for motion artifact correction

A brief description of the techniques that do not require complementary measures and have thus been selected for this comparison work is presented in the following paragraphs.

4.3.1 Spline interpolation

The spline interpolation method employed here is a channel-by-channel approach, based on that proposed by Scholkmann et al. (2010). It acts only on motion artifacts detected, leaving the remaining part of the signal unmodified. Motion artifact segments are automatically identified on a channel-by-channel basis (using the function hmrMotionArtifactByChannel from the Homer2 NIRS Processing package (Huppert et al., 2009), as detailed below in Section 4.5). The period of motion artifact is then modeled via a cubic spline interpolation. The resulting spline interpolation is then subtracted from the original signal, to correct for the motion artifact. The time series must then be reconstructed as the spline subtraction creates different signal levels for the corrected signal compared to the original signal. Every segment is shifted by a value given by the combination of the mean value of the segment and the mean value of the previous segment to ensure a continuous signal.

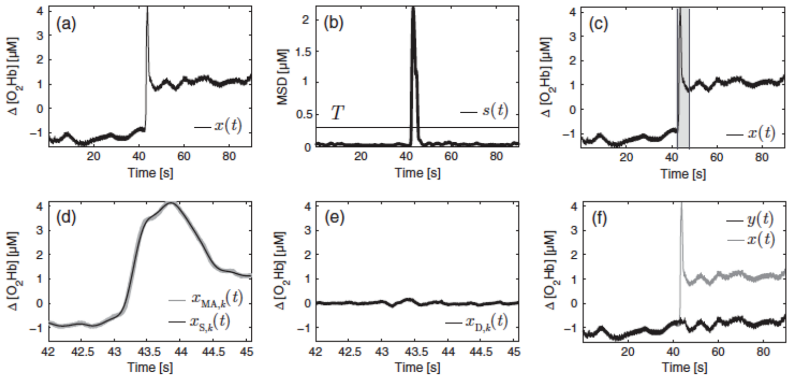

Figure 4.3.1: Spline motion correction algorithm steps. a) Original signal $x(t)$ containing a motion artifact. b) Method used to detect motion artifacts: $s(t)$ is the moving standard deviation and T the threshold used to detect motion artifacts. c) Original signal $x(t)$ with marked motion artifact. d) Zoomed plot of the segment $x_{MA}(t)$ of $x(t)$ which contains the motion artifact, and superposed spline interpolation function $x_S(t)$. e) Residual signal obtained subtracting the spline interpolation from the original signal containing the motion artifact: $x_D(t) = x_{MA}(t) - x_S(t)$. f) Original signal $x(t)$ and denoised signal $y(t)$ after applying the spline motion correction algorithm to $x(t)$. (Taken from Scholkmann et al. (2010)).

In Fig. 4.3.1 are reported and displayed all the steps described above. The spline interpolation depends on a parameter, p, which determines the degree of the spline function. If p=0, the interpolation will be a straight line, while if p=1, it will be a cubic interpolation. In this thesis the parameter p was set to 0.99, the same value used by both Scholkmann et al. (2010) and Cooper et al. (2012c).

A drawback of the spline approach is that it needs to be preceded by a reliable technique that identifies the motion artifacts. If the artifacts are difficult to detect, spline interpolation will not be applied appropriately and thus the technique will not improve the signal. However, an advantage of the spline approach is the ability to remove baseline shifts.

4.3.2 KALMAN FILTERING

The discrete Kalman filtering proposed by Izzetoglu et al. (2010) is also a channel-by-channel approach. The Kalman filter acts on a state-space representation of a dynamic system to provide, recursively, a solution to the linear optimal filtering problem:

$$\begin{cases} x_k = Ax_{k-1} + w_k \\ z_k = Hx_k + v_k \end{cases} \tag{4.1}$$

where x_k is the state at time=t_k, z_k is the measurement at time=t_k (i.e. a sample of the fNIRS signal), A the transition matrix, H the output matrix and w and v are the process and measurement noise respectively. The Kalman filter is a two-step filter: firstly, at time=t_{k-1}, a prediction of the state x at time=t_k and of its uncertainty is computed, using knowledge on prior states. Then, when the measured signal at time=t_k comes, it is used to update and correct the predicted state x_k, which is then used again in the prediction of the next state (Grewal and Andrews, 2001; Haykin, 2001).

To use the Kalman filter for motion correction, the transition matrix A, which uses prior knowledge on the states to predict the future one, has been chosen, in this thesis, as an autoregressive model of order $M = 4$

(Cooper et al., 2012c; Izzetoglu et al., 2010). The coefficients of the model are determined using the Yule-Walker equations, computing the correlation between the longest motion-free period of the signal and itself translated by between 1 to M data-points. A model order higher than $M = 4$ tends to render the algorithm unstable. In order to model the signal over the frequency range of interest (i.e. less than 1 Hz), these 4 datapoints must cover a longer period of data than is covered by 4 datapoints at the sampling frequency of 7.8 Hz. It is therefore necessary to downsample the data as part of the Kalman filter correction procedure. The output measurement of the Kalman filter z_k has been assumed as the motion-corrupted signal, while the state x as the motion-free one and the measurement noise as the motion artifact. The covariance of the measurement noise has been computed as the variance of the whole data-series, while the covariance of the process noise as the variance of the motion-free segments. Motion-free segments were identified as parts of the signal where the Homer2 function hmrMotionArtifact did not find any artifacts.

4.3.3 Principal Component Analysis

Principal component analysis (PCA) applies an orthogonal transformation to the original data set composed of N measurements to produce N uncorrelated components. The order of these components is related to the variance of the original data that the component accounts for. Thus, the first component will account for the largest proportion of the variance of the data. Since motion artifacts are often much larger in amplitude that normal physiological fNIRS signals, they should constitute a large proportion of the variance of the data; thus, it is supposed that the first M components will represent the variance caused by the motion artifacts. Hence, removing the first M components from the signal should correct for the motion artifacts (Zhang et al., 2005b).

The performance of PCA is directly dependent on the number of measurements available (N) and the number of components removed (M). In this thesis N was equal to 40, the number of channels. The number M

is a free parameter of PCA analysis. A way to automatically adjust this value on a subject-by-subject basis is to set the amount of variance to be removed from the data. The sensitivity analysis performed by Cooper et al. (2012c) suggested that 97% of the total variance should be removed to optimize the performance of PCA. This value was obtained for 20 data sets in which the motion artifacts had generally a larger amplitude compared to the evoked hemodynamic response. Since in the data set used in this thesis motion artifacts have an amplitude similar to the cerebral signal, it is likely that removing 97% of the total variance will remove also part of the evoked response. Therefore, in this thesis the PCA was performed with two different values of threshold on the variance: 97% (which will be referred as PCA_97) and 80% (referred as PCA_80). The value of 80% was chosen to be more conservative and remove only the variance supposed to account for the motion artifacts and it is very close to the value already used by Wilcox et al. (2005). The choice to run PCA with both values is motivated by the possibility of showing the importance of properly choosing the value of M for each data group.

4.3.4 Wavelet filtering

The wavelet-based motion artifact removal proposed by Molavi and Dumont (2012) is a channel-by-channel approach designed to correct for motion artifacts. It works in the time-frequency domain, differently from all other approaches that are working in the time domain only. The Wavelab 850 toolbox (`http://statweb.stanford.edu/~wavelab`) for MATLAB was used here to perform the wavelet analysis. The Daubechies 5 (db5) wavelet was chosen, the same used by Molavi and Dumont (2012). The discrete wavelet transform is applied to every channel data series for a number of levels of decomposition, L, given by the duration of the time series. For every level a series of detail and approximation coefficients are obtained (Fig. 4.3.2). Assuming that the measured signal is a linear combination of the physiological signal of interest and the artifacts, that the detail wavelet coefficients have a Gaussian probability distribution

and that the hemodynamic response is smoother and slower than motion artifacts, the expectation is that the coefficients accounting for the evoked response will be centered around zero and with low variance, while the outliers of the Gaussian distribution are the coefficients accounting for the motion artifacts. Therefore, setting these outlying coefficients to zero before reconstructing the signal with the inverse discrete wavelet transform should remove the corresponding motion artifacts in the temporal time-series. Outliers are detected using a probability threshold α: if the probability of a given wavelet detail coefficient is less than α, then this coefficient is assumed to not belong to the Gaussian distribution and it is hence considered an outlier and set to zero.

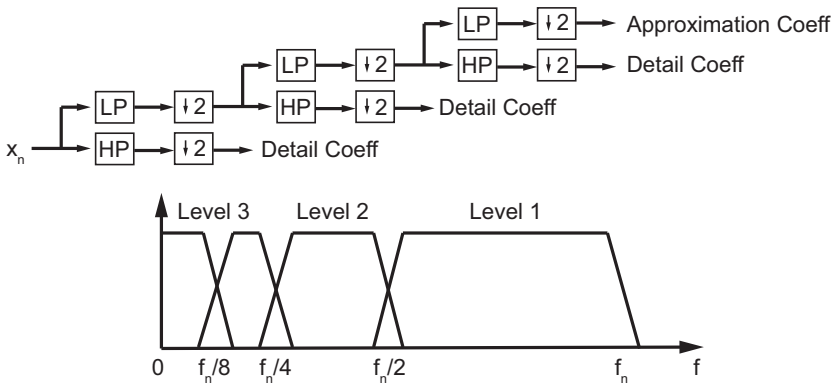

Figure 4.3.2: Rappresentative scheme of wavelet decomposition into L levels. The original signal $x(t)$ undergoes the first level of decomposition. A high-pass filter (HP) is applied with cut-off frequency equal to half of the maximum frequency found in $x(t)$ (f_n) and the detail coefficients of the first level of decomposition are computed after a downsampling procedure. A low-pass filter (LP) with the same cut-off frequency $f_n/2$ is applied to $x(t)$ and the approximation coefficients of the first level of decomposition are computed after the same downsampling procedure. The approximation coefficients obtained after the first level of decomposition undergo the same procedure described above for $x(t)$, with a low- and high-pass filtering with cut-off frequency equal to half of that present in the current data set, i.e. $f_n/4$, computing thus the detail and approximation coefficients for the second level of decomposition. The same identical procedure is performed until the last level of decomposition L, in this case 3. To note, the process is reversible, i.e. knowing the last approximation coefficients and the detail coefficients of all levels, the signal $x(t)$ can be reconstructed.

The parameter α is the tuning parameter of wavelet filtering. In this thesis it was set to 0.1, the same value used by Cooper et al. (2012c) and by Molavi and Dumont (2012).

4.3.5 Correlation-Based Signal Improvement

The correlation-based signal improvement (CBSI) is a channel-by-channel approach developed by Cui et al. (2010) to reduce motion artifacts caused by the movement of the head. It is based on the hypothesis that HbO and HbR should be negatively correlated during functional activation but they become more positively correlated when a motion artifact occurs. The measured HbO and HbR signal, x and y respectively, can be described as:

$$\begin{cases} x = x_0 + \alpha F + Noise \\ y = y_0 + F + Noise \end{cases} \tag{4.2}$$

where x_0 and y_0 are the true HbO and HbR signal to be estimated, F is the motion artifact, with identical effects on both chromophores (but for a constant weighting α), and $Noise$ is the remaining high frequency white noise, easily removed with a low-pass filter. To compute x_0 and y_0, two assumptions are required: the correlation between x_0 and y_0 should be close to -1 and the correlation between the artifact F and the true signal x_0 should be close to 0. This leads to the following equations for the computation of the true HbO and HbR signal:

$$\begin{cases} x_0 = (x - \alpha y)/2 \\ y_0 = -x_0/\alpha \end{cases} \tag{4.3}$$

with

$$\alpha = \frac{std(x)}{std(y)} \tag{4.4}$$

where $std(x)$ is the standard deviation of x. The approach taken by Cui et al. (2010), also assumes that the ratio between HbO and HbR when no

artifact is present is the same as when an artifact occurs.

4.4 DATA

Twenty-two students of the University of Padova (10 males, mean age 25.54 $\pm$ 3.14) took part in the experiment, after providing written informed consent. The data of one participant was discarded because she was unable to correctly perform the task, while the data of three others was discarded because of poor SNR in every channel (likely due to a large mass of hair). Therefore, the total number of participants considered in the following analysis is 18. Each participant was comfortably seated in front of an LCD computer monitor at a viewing distance of approximately 60 cm in a dimly lit room. The paradigm consisted of a color-naming of a non-color word task; the participant was asked to say aloud the color of the text of a word appearing on the screen. The study consisted of 4 different stimulus conditions, with 40 trials per condition presented to the participants, leading to a total of 160 trials, divided into two sets of 80. Each word was presented on the screen until the subject started to pronounce the color of the word (~850 ms). The inter-stimulus interval varied among 10, 11 or 12 seconds. The experiment was approved by the ethical committee of the University of Padova.

The fNIRS data was acquired with a multi-channel, frequency-domain NIR spectrometer (ISS ImagentTM, Champaign, Illinois) equipped with 32 laser diodes (16 emitting light at 690 nm and 16 at 830 nm) and 4 photo-multiplier tubes. Source and detector fibers were positioned on the participants' head using a probe-placement method based on a physical model of the head surface (Cutini et al., 2011b) so that frontal and premotor areas were sampled (Fig.4.4.1 a)) (Cutini et al., 2008)). Each source fiber carried light at both of the two different wavelengths; five source fibers were placed around each detector fiber, at a distance of 3 cm. Therefore, a total of 20 channels per wavelength (10 per hemisphere) were measured for each participant. Note that in this experiment there was no short-separation channel (see chapter 3). Indeed, its utilization

would have meant the sacrifice of 5 channels per hemisphere. Here, instead, the interest was more, both for a cognitive point of view, and for the comparison between motion correction techniques, to gain information on more brain areas as possible. Of course, if more sources and detectors had been available, the use of the short-separation channel would have been recommended. The sampling frequency was set to approximately 7.8 Hz.

The data acquired during this experiment contained a particular type of motion artifact, which was caused by the participants' jaw movement induced by the vocal response. The opening and closing of the mouth caused an abrupt displacement of the sources and detectors positioned on the participant's head, thus producing a motion artifact in the data series that was correlated with the evoked cerebral response (present in the first 1-2 seconds after stimulus onset). The shape and duration of this artifact (Fig.4.4.1 b)) differs from the more common spike-like artifacts because it is slower and correlated with the hemodynamic response. Given that its amplitude is comparable to the hemodynamic response elicited by cortical activity, the artifact is more difficult to detect.

It is also important to note that not all participants and all channels presented this type of artifact; participants with less hair tended to have the fiber holder placed more tightly to the head and hence this type of artifact was less common. The artifact was also channel-specific, appearing more commonly in the most anterior channels (see Fig. 4.4.1 a)). The fact that the motion artifact is not observed on all channels simultaneously is likely to affect the performance of the motion artifact correction, since some methods inherently require unwanted signal components to be apparent in multiple channels. While this hypothesis may be reasonable in many cases, as motion artifacts are often due to movement of the whole head, this is not the case for this data series. Therefore, it is likely that the correction methods which work on a channel-by-channel basis will perform better than those that work on all channels all together.

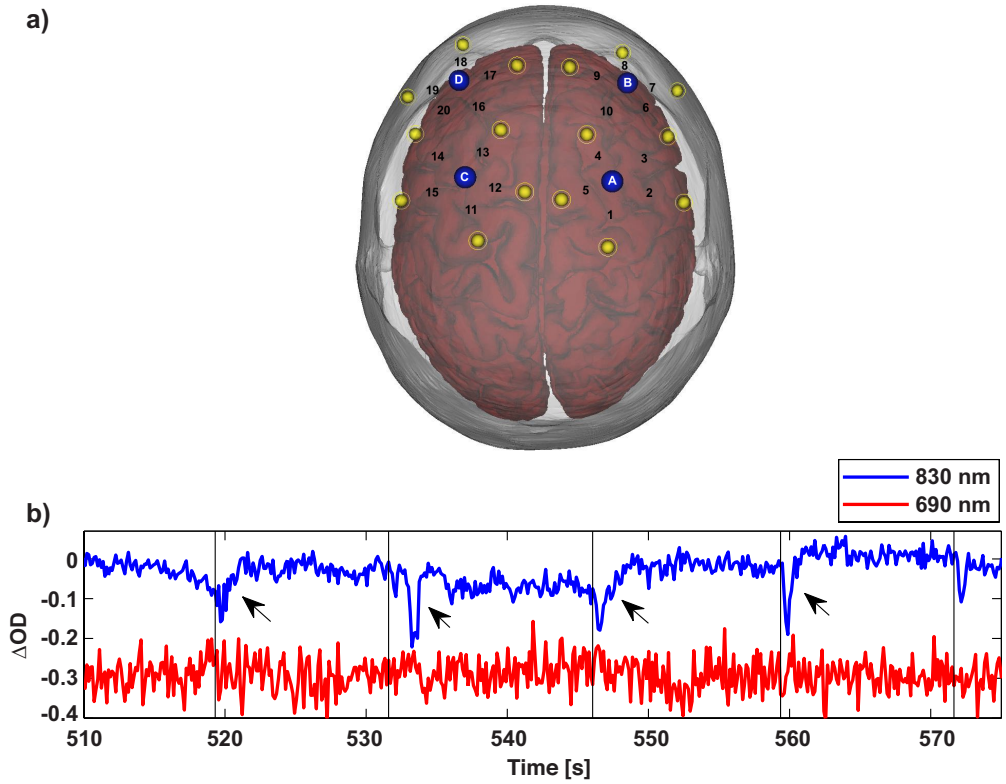

Figure 4.4.1: a) Probe placement: detectors in blue and sources in yellow. Numbers represent the channels. b) Example of motion artifacts present in the time-series of one participant. The blue line shows the 830 nm wavelength time-series, the red line the 690 nm wavelength time-series. The 690 nm time-series has been shifted by -0.3 for visualization purposes. Vertical lines indicate when the stimulus is presented to the participant. Note how the motion artifact is correlated to the task.

4.5 DATA PROCESSING

The data processing was performed, as stated before, using some of the Homer2 NIRS processing package functions (Huppert et al., 2009) based in MATLAB (Mathworks, MA USA). A flow-chart depicting the signal processing steps is presented in Fig. 4.5.1. For every subject, the raw optical intensity data series were converted into changes in optical density (OD). Channels with a very low optical intensity where discarded from the analysis using the function enPruneChannels. All trials where the participant gave a wrong response to the stimulus were also discarded from the analysis. Then the motion detection algorithm hmrMotionArtifact was applied to the OD time-series to identify motion artifacts. This algorithm finds the data-points exceeding a threshold in change of amplitude ($AMPthresh$) and a threshold in change of standard deviation ($SDThresh$) within a given period of time ($tMotion$) and then marks those points from the beginning of the window to $tMask$ seconds later as motion. Both the thresholds, the window length and tMask, are set by the user. In this study, $AMPThresh = 0.4$, $SDThresh = 50$, $tMotion = 1$ and $tMask = 1$, which provided a compromise between the number of motion artifacts identified in noisier data series and the number identified in less noisy data series. The function hmrMotionArtifact assumes that when an artifact is identified in one channel, that period of data should be removed from all channels and hence, the output of this algorithm is not channel specific. Thus, for the spline technique, the function used to detect motion artifacts was instead hmrMotionArtifactByChannel, which works exactly the same way as hmrMotionArtifact but on a channel-by-channel basis.

After motion artifact identification, 8 different processing streams were performed. Six of these processing streams included a motion correction method, one applied the trial rejection technique and one recovered the evoked response without removing or correcting the motion artifacts.

Of the 6 processing streams including a motion correction method, 5

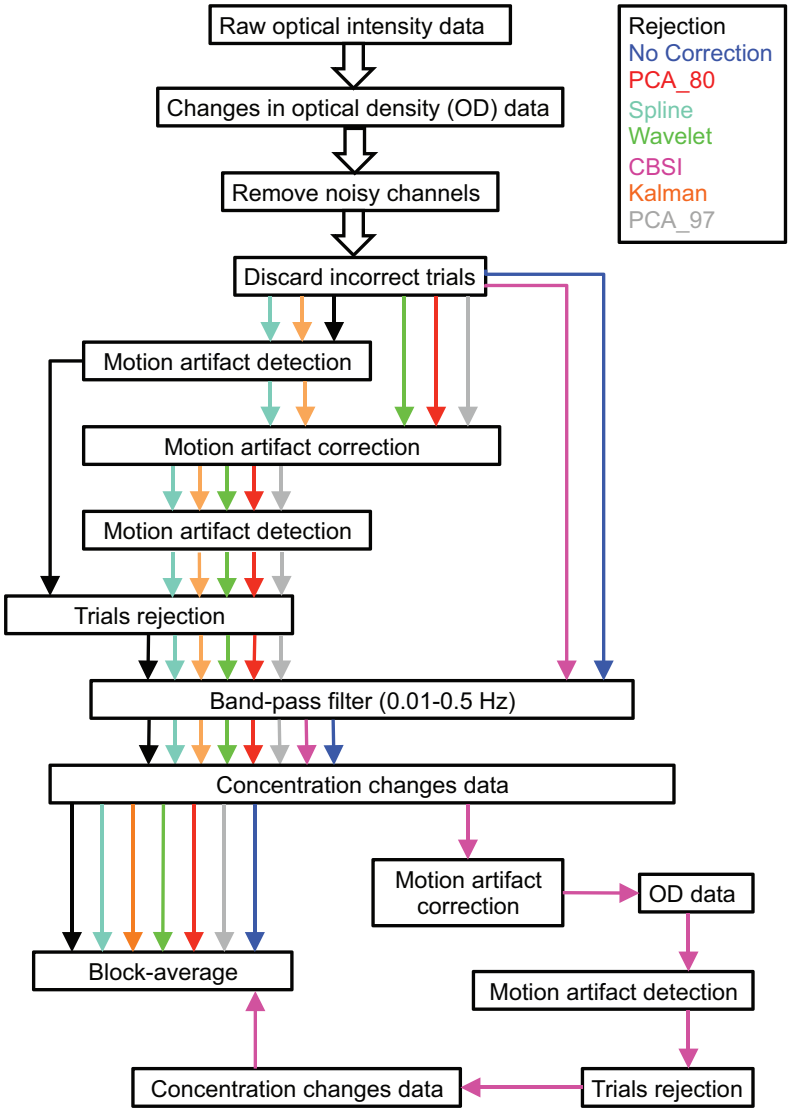

Figure 4.5.1: Signal processing steps for all techniques. The processing streams for every technique are represented by colored arrows: black for rejection, blue for no motion correction, red for PCA_80, cyan for Spline, green for Wavelet, magenta for CBSI, orange for Kalman filter and gray for PCA_97.

(PCA_80, PCA_97, Spline, Wavelet, Kalman filter) started with the application of the motion correction technique on the OD data. hmrMotionArtifact was run again on the corrected OD time series and the trials where a motion artifact was still present were rejected.

A band-pass filter (third order Butterworth filter) with cut-off frequencies of 0.01-0.5 Hz was then applied to the data in order to reduce very slow drifts and high frequency noise. The OD data were then converted into concentration changes using the modified Beer-Lambert law (Cope and Delpy, 1988; Delpy et al., 1988). Finally, to recover the mean hemodynamic response, all remaining trials related to the same stimulus type were block-averaged. This produced four mean HRs, one per stimulus type, for each channel and each participant.

The 6th processing stream was different, since the CBSI method works on concentration changes and not on OD data. Therefore, the same band-pass filter was applied to the OD data series, which were then converted into concentration changes. The CBSI method was then applied and the mean HR was recovered via block-averaging the motion corrected trials. Before block-averaging, trials still contaminated by a motion artifact were rejected, using the hmrMotionArtifact on the OD time-series after the CBSI correction.

In the processing streams for the rejection method and the no motion correction method, the same band-pass filter was applied to the OD data, which were then converted into concentration changes. For the no motion correction method the mean HR was recovered by block-averaging the trials related to the same stimulus type, while for the rejection method, before computing the mean HR, all trials where a motion artifact was detected were rejected.

4.6 Metrics for comparison

In order to compare quantitatively the performance of the different motion correction techniques, five metrics were defined. Since the true hemodynamic response is unknown, these metrics were chosen in order to pro-

vide measures of how physiologically plausible the HRs are. The hemodynamic response observed by fNIRS is relatively well understood and well documented (Huppert et al., 2006; Plichta et al., 2007). Although its scale and duration are variable, certain features of the HR are essentially stable. For instance, the increase in localized cerebral blood flow that gives rise to the HR is known to take 1-2 seconds to become apparent after the onset of stimulation.

Because in this particular data series the most common motion artifact was present in the first two seconds after the presentation of the stimulus, the first defined metric is the area under the curve computed on the mean HR for the first two seconds after stimulus onset (AUC_{0-2}) (see Fig. 4.6.1 a)). The lower this index, the better the correction of the artifact.

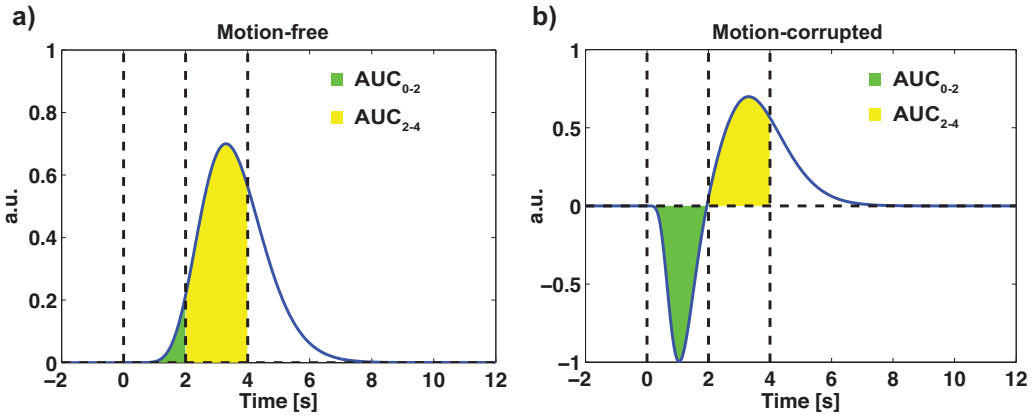

Figure 4.6.1: Examples of AUC_{0-2} and AUC_{2-4} computation on synthetic HR created for illustration purposes. a) Motion-free HR and b) motion-corrupted HR, with a motion artifact predominantly appearing in the first couple of seconds after stimulus onset. In green the AUC_{0-2} metric is displayed while in yellow the AUC_{2-4} one. Note how AUC_{0-2} is expected to be smaller in the motion-free HR, while *AUC ratio*, computed as the ratio between AUC_{2-4} and AUC_{0-2}, is expected to be larger in the motion-free HR.

The second computed metric is the ratio between the area under the curve (*AUC ratio*) of the mean hemodynamic response between 2 and 4 seconds (AUC_{2-4}) and AUC_{0-2} (see Fig. 4.6.1 b)). This assumes that the hemodynamic response will reach its maximum between 2 and 4 seconds

after the onset of the stimulus.

The third defined metric is the mean of the standard deviation of the single-trial (i.e. un-averaged) hemodynamic responses used in the computation of the mean hemodynamic response. It will be referred as the *within-subject standard deviation (SD)*, and it should take into account the variability present in every subject. This assumes, as a first approximation, that the variability between hemodynamic responses is predominantly due to motion artifacts, while the physiological variability between them plays a minor role (and should be ideally constant among the techniques). The current dataset provides 1440 values (18 subjects, 20 channels, 4 conditions) of each of these three metrics (AUC_{0-2}, *AUC ratio* and *within-subject SD*).

The fourth computed metric is the standard deviation between subjects for a given channel and condition, referred to as *between-subject SD*. This index considers the variability present between subjects. The total number of values obtained is 80 (20 channels and 4 conditions).

Finally, the fifth metric is the number of trials averaged for every subject and condition in order to compute the mean HR. Every channel has the same number of trials block-averaged, because, after correction, when a motion artifact was identified, the trials related were removed from every channel. For this last metric a total of 72 values was obtained (18 subjects and 4 conditions).

In the results that follow, all motion correction techniques were compared to the no motion correction approach and to each other using these 5 metrics.

4.7 Results

A summary of the results of the metrics AUC_{0-2}, *AUC ratio* and *within-subject SD* computed for all techniques, for both HbO and HbR, are reported in Fig. 4.7.1. Fig. 4.7.2 shows the mean number of trials averaged to obtain the final HR with every technique, normalized to the mean number of trials averaged with the no motion correction technique. A

repeated measure ANOVA with technique as a within-subject factor has been computed for all these metrics. Every subject was represented by a unique value for every technique, obtained by averaging all values of the subject across channels and conditions. A main effect of technique has been found for all the metrics (all $p<.01$). Two-tail paired t-tests were then performed to compare all the techniques to each other using these metrics. Results are reported in Fig. 4.7.1 and Fig. 4.7.2.

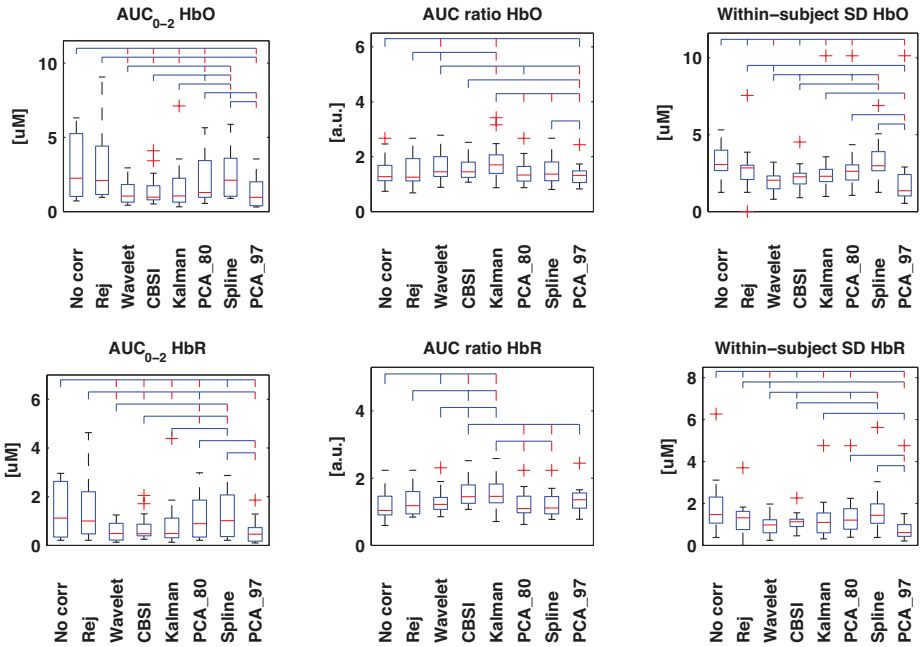

Figure 4.7.1: Box plots of the AUC_{0-2}, *AUC ratio* and *within-subject SD* computed for all techniques and for both HbO (upper row) and HbR (bottom row). The red line in the box plot indicates the median, while the two extremities of the box plot represent the first and third quartile. Red crosses indicate outliers. The lines above linking the different techniques represent the significant statistical difference ($p<.05$ if the line is blue, $p<.01$ if the line is red).

The pattern of results for HbO and HbR are consistent. For AUC_{0-2}, no correction, rejection and spline interpolation present the highest values and the highest standard deviations; the other techniques present lower values, with Wavelet, CBSI, Kalman and PCA_97 showing less variability.

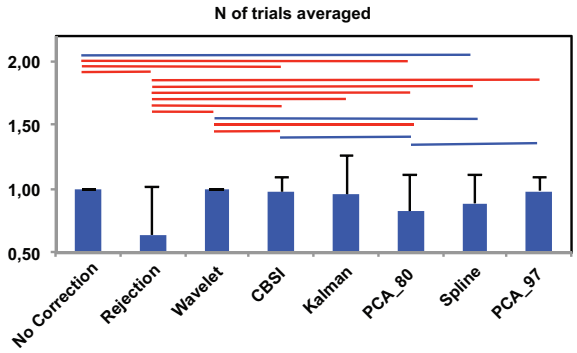

Figure 4.7.2: Bar plots with the mean number of trials averaged for each technique normalized to the mean number of trials averaged with the no motion correction technique; the error bars represent the standard deviation. The lines above indicate whether the techniques that they link together differ significantly from each other ($p<.05$ if blue, $p<.01$ if red).

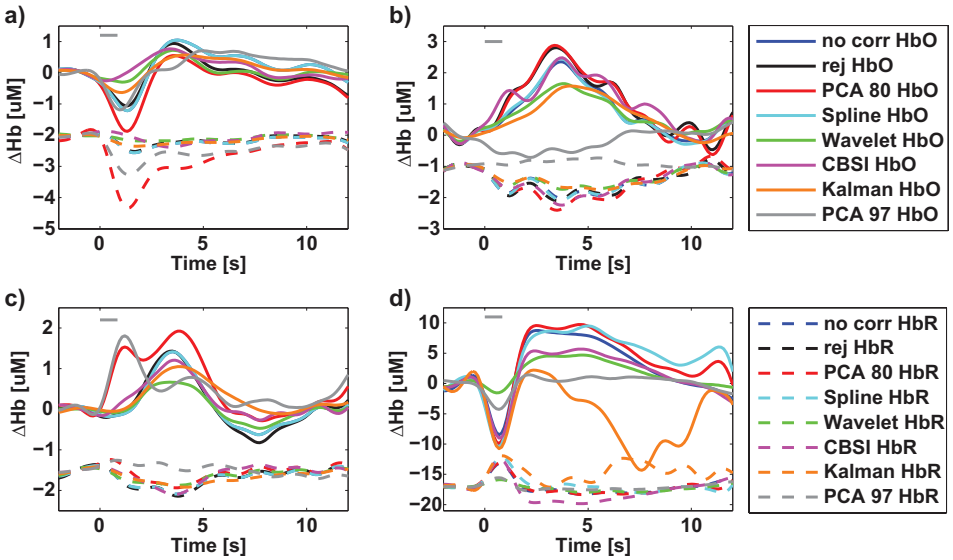

Figure 4.7.3: Examples of recovered mean HRs for four selected subjects, channels and tasks for every technique for both HbO (solid line) and HbR (dashed line). HbR HRs have been shifted in baseline towards negative values for visualization purposes only. In a) Wavelet and CBSI provide some minimization of the motion artifact, while PCA_80 increases it. In b) all techniques but PCA_97 are able to recover physiological HRs, no motion correction included; PCA_97 highly underestimates the HR. c) is an example of PCA_80 and PCA_97 adding a motion artifact in a motion-free channel and d) is an example of a channel in one subject where the Kalman filter is unstable. Gray line represents the actual task duration, 850 ms, which is the grand average of the reaction times, i.e. the time needed by participants between the appearance of the word and the color being pronounced.

The CBSI and Kalman techniques produce the highest *AUC ratio*, followed by Wavelet. For this metric, no correction and rejection exhibit the worst performance.

Wavelet and PCA_97 perform very well in reducing the *within-subject SD*, while no correction and Spline yield the highest standard deviation.

Wavelet is the only technique able to recover all trials (Fig. 4.7.2). The worst performing technique for this metric is obviously rejection; about 40% of the trials have been rejected due to motion artifacts.

In Fig. 4.7.3 four examples of the recovered HR for all techniques are displayed.

4.7.1 REJECTION VS. NO-MOTION CORRECTION

Scatter plots of the AUC_{0-2} computed on the mean HRs recovered via rejection (y axis) and no motion correction (x axis) are shown in Fig. 4.7.4 a) and b) for both HbO and HbR. Performance of no correction and trial rejection are comparable for both HbO and HbR. In one third of cases, trial rejection decreases AUC_{0-2}, suggesting that it is at least partially successful in removing the motion artifact. In another ~third of cases however, rejection increases AUC_{0-2}, compared to not rejecting the trials. In the final third of cases no motion artifacts have been identified and therefore the two techniques give the same results. No statistically significant differences have been found between the two techniques for this metric (paired t-tests: p=.475 for HbO and p=.358 for HbR).

The same conclusions can be drawn for the *AUC ratio* metric (data not shown). No statistically significant differences have been found between the two techniques (paired t-test: p=.487 for HbO and marginally significant p=.072 for HbR) for this metric. It is clear how rejecting trials is characterized by a variable efficacy.

For the *between-subject SD* metric, the rejection method performs worse than the no motion correction one, increasing the standard deviation among the subjects' mean HR (65% of the time for HbO and 60% for

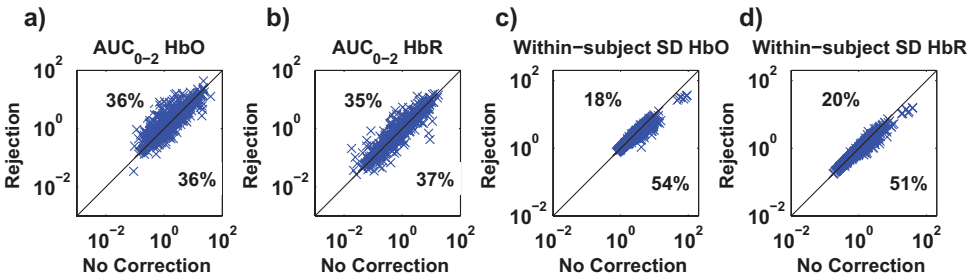

Figure 4.7.4: a) and b) Scatter plots of the AUC_{0-2} metric computed with the rejection technique (y axis) vs. that computed with no motion correction technique (x axis) for both a) HbO and b) HbR. Trial rejection decreases AUC_{0-2} 36% of the time for HbO and 37% for HbR, but increases it in almost the same percentage of cases. 28% of the times the AUC_{0-2} value is identical for both techniques. c) and d) Scatter plots of the *within-subject SD* metric computed with the rejection technique (y axis) vs. that computed with no motion correction technique (x axis) for both c) HbO and d) HbR. Trial rejection decreases the standard deviation 54% of the time for HbO and 51% for HbR compared to no motion correction.

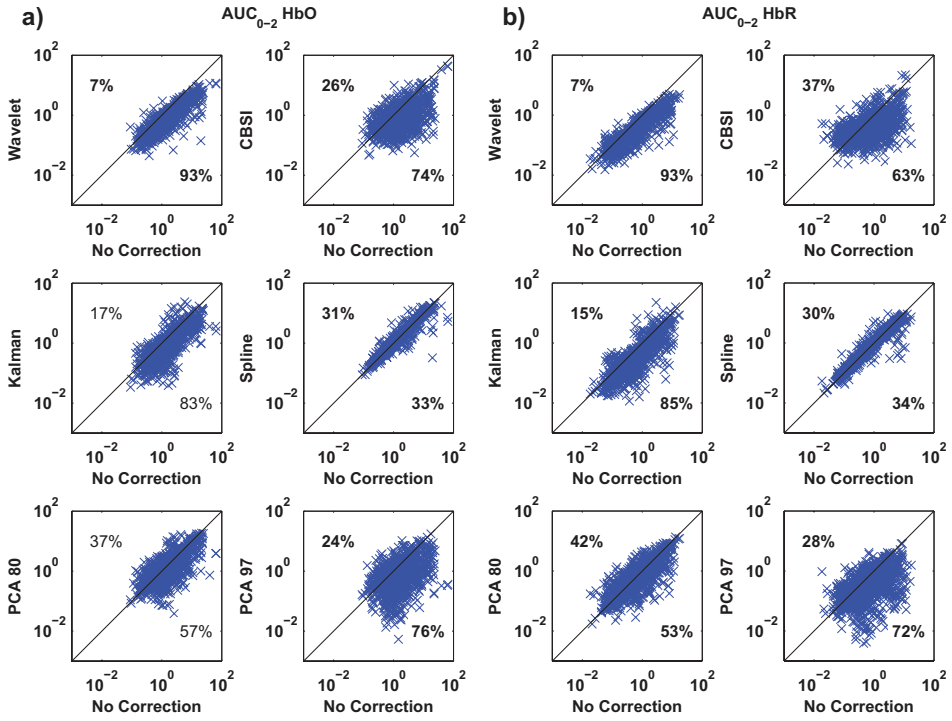

Figure 4.7.5: Scatter-plots of the AUC_{0-2} metric for both a) HbO and b) HbR: no-motion correction (x axis) vs. Wavelet, CBSI, Kalman, Spline, PCA_80 and PCA_97 (y axis).

HbR). This is probably due to the very noisy mean HRs obtained from those subjects where many trials have been rejected.

The rejection method, instead, performs better than the no motion correction technique in the *within-subject SD* metric (Fig. 4.7.4 c) and d)). Statistically significant differences have been found between the two techniques (paired t-tests: $p<.05$ for both HbO and HbR). Indeed, the cases where a lot of trials have been rejected have very low influence on the performance of this index. It shows how rejecting trials where a motion artifact had been detected is effective in reducing the standard deviation between trials in the same subject.

4.7.2 Motion correction techniques vs. no-motion correction

Scatter plots of AUC_{0-2}, *between-subject SD* and *within-subject SD* values computed on the mean HRs recovered via the no motion correction method (x axis) and all the other techniques (y axis) are shown in Fig. 4.7.5, Fig. 4.7.6, Fig. 4.7.7 for both HbO and HbR.

The wavelet technique is the most effective at reducing AUC_{0-2} (Fig. 4.7.5), with a tendency to have a slightly detrimental effect (7% of the times) when the value of AUC_{0-2} is already low when no motion correction technique is applied. Kalman, CBSI and PCA_97 also perform well, reducing AUC_{0-2} compared to the no motion correction method (83, 74, 76% of the cases for HbO and 85, 63 and 72% for HbR), although the variability is higher compared to Wavelet. The PCA_80 approach performs slightly worse, increasing the area under the curve in 37% and 42% of cases for HbO and HbR, respectively. All these changes achieve statistical significance (all $p<.01$). The spline technique has little effect; marginally significant differences have been found between Spline and no motion correction for HbO, while significant differences have been found for HbR (paired t-tests: $p=.091$ for HbO while $p<.05$ for HbR).

The Kalman filter is the most efficient technique in increasing the *AUC*

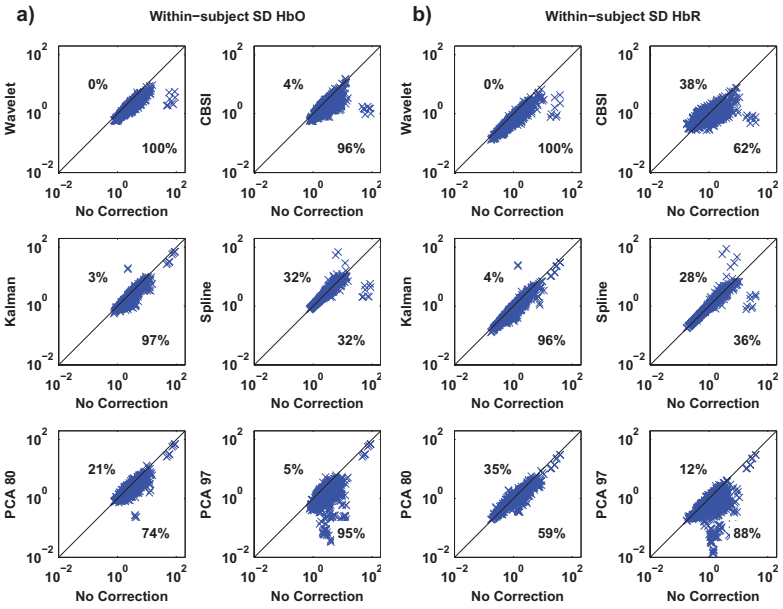

Figure 4.7.6: Scatter-plots of the *within-subject SD* metric for both a) HbO and b) HbR: no-motion correction (x axis) vs. Wavelet, CBSI, Kalman, Spline, PCA_80 and PCA_97 (y axis).

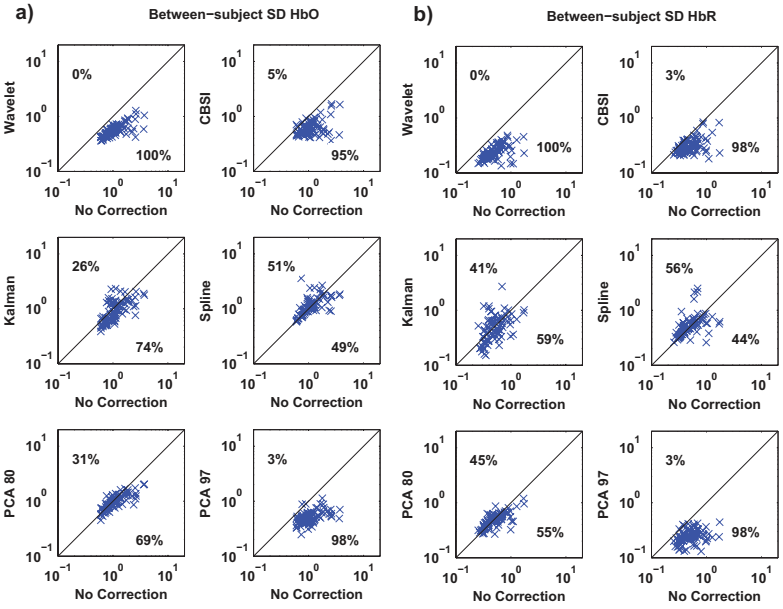

Figure 4.7.7: Scatter-plots of the *between-subject SD* metric for both a) HbO and b) HbR: no-motion correction (x axis) vs. Wavelet, CBSI, Kalman, Spline, PCA_80 and PCA_97 (y axis).

ratio, followed by Wavelet and CBSI (statistically significant differences, all $p<.05$, but CBSI in the HbO case $p=.162$). There is a high percentage of cases where these techniques decrease the *AUC ratio*, compared to no motion correction. Possibly, the amplitude of the HR in the 2-4 seconds window is driven by the motion artifact leading to a bigger *AUC ratio* than when the artifact is removed. Both Spline and PCA_80 have no statistically significant differences with the no motion correction technique (paired t-tests: $p=.510$ and $p=.307$ for PCA_80 HbO and HbR respectively, $p=.434$ and $p=.247$ for Spline HbO and HbR respectively). PCA_97 obtains the worst result, performing significantly worse than the no motion correction technique in the HbO case (paired t-test: $p<.05$), while marginally significant differences have been found for HbR (paired t-test: $p=.069$).

Except Spline, all techniques significantly reduce the *within-subject SD* (Fig. 4.7.6) (paired t-tests: all $p<.05$, Spline: $p=.372$ for HbO and $p=.720$ for HbR,). Crucially, the wavelet technique is able to reduce the standard deviation in 100% of cases.

The *between-subject SD* metric (Fig. 4.7.7) shows the same pattern of results as the previously described metric, with Wavelet outperforming the other techniques and Spline performing poorly.

4.8 Conclusive considerations and remarks

Several comparisons of motion correction techniques have been performed using simulated data, but little is known about their performance on real data. It is thus important to study their behavior in a real situation. The metrics used here for comparative purposes aim to quantify whether the technique is able to recover physiological hemodynamic responses. The AUC_{0-2} and *AUC ratio* metrics are very specific to this set of data, but since the aim of the study is to compare the techniques in their ability to correct for this particular type of low-frequency, task-related motion artifact, these metrics are believed to be the most informative.

4.8.1 Rejection vs no-motion correction

The first result of note relates to the use of trial rejection. Data shows that the rejection technique will sometimes provide an improvement compared to no correction for motion artifacts, although it might sometime deteriorate the results. The no motion correction technique and the rejection technique are highly dependent on the number of motion artifacts present in the data and on the number of trials available for averaging. If few motion artifacts are present in the data and the related trials are removed, the rejection technique can improve the recovery of the HR. For instance, the cases where the AUC_{0-2} metric is increased to a very high value compared to no motion correction are cases where a large proportion of trials had been removed. The number of trials rejected is subject-dependent: there are some subjects where no trials were discarded and others where almost all have been rejected. The mean number of trials removed per subject is about 40% the number of total trials (160).

Furthermore, the number of trials containing motion artifacts is suspected to be even higher, since due to its particular shape and frequency, the artifact present in this data-series was not always properly detected.

An efficient motion correction technique should be applicable in cases where the number of motion artifacts is high and in cases where it is low. The good results achieved by the rejection technique in the *within-subject SD* metric are probably due to the fact that the cases where most of the trials are discarded have less influence on this parameter. This is mirrored in the *between-subject SD* metric, where rejection performs worse than no correction: in this case, the noisier mean HRs recovered with very few trials have greater influence on the total result. In conclusion, the rejection approach is not appropriate for this data set. It can only be used with good results when the number of artifacts is small compared to the number of trials.

4.8.2 MOTION-CORRECTION TECHNIQUES VS NO-MOTION CORRECTION

Spline interpolation has been shown to achieve very good results in previous publications (Cooper et al., 2012c; Scholkmann et al., 2010). However, this is not the case for this study. It shows little improvement compared to the no motion correction technique, both in the metrics we define and in the shape of the recovered hemodynamic response. The reason why Spline is not working well on this data set is due to its dependence on the method of artifact detection. As previously stated, the main motion artifact present in this data-set is difficult to detect because it has an amplitude and frequency content that are not dissimilar from physiologically components present in the fNIRS signals. As a result, there are likely to be many occasions where spline interpolation is not applied when it should be, leading to the same results as the no motion correction technique. It is likely that spline interpolation would have achieved better results if this motion artifact could have been more easily identified or a new and more efficient motion detection technique had been implemented.

Cooper et al. (2012c) showed that PCA performed better than no motion correction, but at the same time, it was outperformed by the other techniques. The same result is apparent here. In this study, PCA was run with two different targets for the percentage of variance to be removed: 80% and 97%.

Although all metrics but one suggest that PCA_97 is successful in removing motion artifacts, the mean HRs themselves show that PCA_97 is simply removing the HR itself. In this data-set not every subject exhibited motion artifacts and not every motion artifact was present in every channel. PCA orders components by how well they explain the data; hence, if there are a lot of large amplitude artifacts, the first principal components will account for those artifacts. In the data studied here, removing 97% of the variance means removing not only motion artifacts but also part of the recovered HRs and other physiological aspects of the signal. PCA run with 80% of the variance removed (PCA_80), instead, achieves the

same pattern of results that Cooper et al. (2012c) found in their paper: it is able to recover a significant number of trials and to significantly reduce AUC_{0-2} and the standard deviation metrics compared to no motion correction. However, the improvements are negligible compared to those of the other techniques.

An important problem with PCA is that it is a multi-channel approach: it requires that an artifact is present in multiple channels. Clearly this is not always true, particularly for artifacts arising from movement of the facial muscles, which can be quite localized. This is likely the cause of its poor performance. Another problem with PCA applied to this data set is that its most basic assumption (that the components of the signal are independent) is likely to be violated. The motion artifact present in this data is temporally correlated with the HR, and therefore clearly not independent. The violation of this assumption may also contribute to the poor performance of PCA.

The different results achieved with the two different percentages of variance removed highlight the importance of choosing the correct value for this parameter. The ideal value is clearly data-dependent. An objective method to estimate the best percentage of variance to choose could potentially be developed and would make PCA much more applicable across a variety of data sets. PCA seems indeed more suited for eliminating systemic oscillations (Cutini et al., 2012b; Virtanen et al., 2009).

The discrete Kalman filtering approach is the best performing technique in the *AUC ratio* metric and performs very well in the AUC_{0-2} and the *within-subject SD*. However, from Fig. 4.7.1, it can be noted that the variability in the AUC_{0-2} metric, for example, is very large. This is reflected in the fact that the poorest performance of the Kalman filter compared to the other techniques is in the *between-subject SD* metric (Fig. 4.7.7). By inspecting the recovered HRs, it is clear that the Kalman filter is able to recover physiologically plausible hemodynamic responses in most of the subjects. However, in about 5 subjects out of 18, the filter is unstable and the corrected signal is corrupted by noise (Fig. 4.7.3 d)). It is worth re-stating that the Kalman filter requires, as does Spline,

the identification of artifacts prior to its application, which may also limit its success. However, it is clear that the stability of the Kalman filter approach has to be improved in order for it to become an accepted motion correction technique.

Wavelet filtering is the only technique able to recover all possible trials. It is the best performing technique in the reduction of both the standard deviation metrics, reducing it in 100% of cases compared to that of no motion correction. It is the best performing approach also in the AUC_{0-2} metric, reducing it in 93% of cases. Wavelet filtering does not rely on any motion detection algorithm and it performs the best for almost every metric computed. This result is significant because the wavelet approach was designed and (to date) mostly applied to correct for high frequency spike-like artifacts, while the motion artifact present in this data-set is of a completely different form. Our results therefore suggest that the wavelet approach can work very well with different forms of motion artifacts, even those that are relatively subtle. The main drawback of the wavelet approach is its high computational cost and the possibility that it underestimates the HR. It is likely that some wavelet coefficients associated with the HR are set to 0, because, being that the motion artifact has a frequency near that of the hemodynamic response, the coefficients belonging to the two entities are not clearly distinct. Nevertheless, improvements in the probabilistic method used to detect wavelet coefficients related to the motion artifacts might be a suitable way to further improve this technique and bypass such drawback.

The correlation-based signal improvement technique shows a good performance in all metrics, reducing both the standard deviations and the AUC_{0-2} parameter. However, it relies on some assumptions that are not always met. Most importantly, it assumes that HbO and HbR are always positively correlated during an artifact and that the ratio of HbO to HbR is constant, maintaining the same value also when the artifact occurs. A failure to meet these hypotheses is likely to detrimentally affect the performance of the CBSI method. A further drawback of the CBSI technique is the fact that it recovers the HbR HR signal from that of the HbO HR

signal, such that they differ only by a constant negative value. This implies that the HbR hemodynamic response recovered is not linked to the real data acquired and there are many cases, particularly in the study of cerebral pathology, where such a rigid relation is likely to be breached (Obrig and Steinbrink, 2011).

4.8.3 Final remarks

For the type of motion artifact studied here, most of the tested correction techniques achieve good results, even if they are outperformed by wavelet filtering. Previous studies have also shown that while wavelet filtering is, on average, the best technique for motion artifact correction (Cooper et al., 2012c; Molavi and Dumont, 2012), other techniques can perform better for particular fNIRS datasets (Izzetoglu et al., 2010; Scholkmann et al., 2010). Until a single, universally effective motion artifact correction method is finalized, the best approach for fNIRS analysis may be to use an objective approach to select the most appropriate technique specifically for each set of data. This can be performed using the methods outlined in this chapter. The two standard deviation metrics proposed, as well as the final number of trials recovered, can be used as objective metrics to test the performance of different motion correction approaches on different groups of data and thus select the most appropriate technique for its analysis. It is only after many different data-sets with different types of motion artifacts have been analyzed and compared using different motion correction techniques, that a universal approach can be identified and accepted.

In conclusion, motion artifact correction is an essential step in the fNIRS data processing pipeline. All tested techniques produce an improvement in the metrics computed compared to not correcting for motion artifacts. However, the performance of spline interpolation and of PCA seems to be variable depending on the data set used. The recommendation is to use them only when motion artifacts can be easily detected for the former and when motion artifacts are the principal source of variance for

the latter. The CBSI method is able to reduce the type of artifact observed here, but it relies on stringent assumptions on the relation between HbO and HbR that are not always met. The Kalman filter is able to reduce motion artifacts, but can be unstable. The wavelet filter is the most effective method of removing the low-frequency, low-amplitude, HR-correlated artifacts present in these data. Given this result and that of previous studies, wavelet filtering is believed, with some improvements, to have the potential to become a standard method for correction of motion artifacts in fNIRS data.

5

Neonatal optical head models for DOT image reconstruction

5.1 Preterm to term neonates and DOT

Thanks to steady advances in perinatal medicine, the survival rate for preterm infants has considerably increased in the last 3 decades. According to the report of the European Foundation for the Care of Newborn Infants (EFCNI) most European countries have preterm birth rates of 7% or above. Although the mortality of preterm babies is decreasing, long-term complications due to prematurity are still a significant challenge (Costeloe et al., 2012). The increasing accuracy and applicability of functional imaging technologies, including diffuse optical tomography are likely to play an increasingly significant role in the monitoring of preterm development.

As seen in section 2.3, diffuse optical tomography is most accurate

when an individual's MRI data can be used as a spatial prior for image reconstruction and for visualization of the resulting images of changes in oxy- and deoxy-hemoglobin concentration. As this necessitates an MRI scan to be performed for each study, which undermines many of the advantages of diffuse optical methods, the use of registered atlases to model the individual's anatomy is becoming commonplace. While several adult's head models have been proposed, there are only a limited number of studies that have attempted to produce accurate infant's head models. Indeed, there are more difficulties in dealing with infants' MRIs than with adults'. Furthermore, infant studies require carefully age-matched atlases because of the rapid growth and maturation of the infant brain. Therefore, the creation of a 4D neonatal head model is a very promising topic of research in the optic field.

In this chapter, a novel 4D neonatal head model is presented which, for each week from 29 to 44 weeks post-menstrual age, includes:

1. A multi-layered tissue mask which identifies extra-cerebral layers, cerebrospinal fluid, grey matter, white matter, cerebellum and brainstem
2. A high-density volumetric multi-layered tetrahedral head mesh
3. Surface meshes for the scalp, grey-matter and white matter layers
4. Cranial landmarks and 10-5 locations on the scalp surface

This package, freely available online at www.ucl.ac.uk/medphys/research/4dneonatalmodel can be applied by users of near-infrared spectroscopy and diffuse optical tomography to optimize probe locations, optimize image reconstruction, register data to cortical locations and ultimately improve the accuracy and interpretation of diffuse optical techniques in newborn populations.

5.2 Optical head models

As stated in paragraph 2.3.2.2, infants' head models proposed until now are all single-age head models. Although these single-age atlases have many applications, the ideal neonatal atlas should be built from MRI data obtained over a wide pre-term to term age range, and would ideally include enough data at each age to allow an atlas to be dynamically produced for any arbitrary age within that range. As seen in paragraph 2.3.2.2 the atlas proposed by Kuklisova-Murga sova et al. (2011) does just that and the volumes are publicly available for 29 to 44 weeks PMA in one week intervals (www.brain-development.org). However, the lack of the extra-cerebral tissue layers prevents the use of these currently available volumes. Indeed, DOT requires a forward model to be computed based on the scalp locations of each source and detector; therefore, a model of the extra-cerebral tissues is essential.

In the following paragraphs, a description of each step of the construction of the optical head models is presented, including a description of the first step, the generation of the MRI atlas with the extra-cerebral tissue layers. MRI data were made available by dr. Paul Aljabar (King's College, London, U.K.), who also built the new MRI atlas used for the creation of the optical head model.

5.2.1 Data

The MRI atlas on which the head models are based was built using 324 (160 female) T2-weighted fast-spin echo images acquired on 3T Philips Intera system with MR sequence parameter TR = 1712 ms, TE = 160 ms, flip angle 90° and voxel size 0.86 x 0.86 x 1 mm. The original atlas (Kuklisova-Murga sova et al., 2011) was built using 142 T2-weighted images; new images have been acquired since its release and have been added to the average volumes on which the presented head models are based. The age range of the newborns at the time of scanning was 26.7 to 47.1 weeks PMA.

5.2.2 MRI Atlas pre-processing

Because of the necessity of including scalp and skull information in the final atlas, the same process of affine registration to an average reference space and voxel-wised weighted intensity averaging, with weights obtained with a Gaussian kernel regression, described in Kuklisova-Murgasova et al. (2011), was performed on all 324 T2-weighted images, without removing the extra-cerebral layers. An averaged T2-weighted image including the extra cerebral tissues was therefore obtained for each week from 29 to 44 weeks PMA yielding a total of 16 volumes, a subset of which are shown in Fig. 5.2.1.

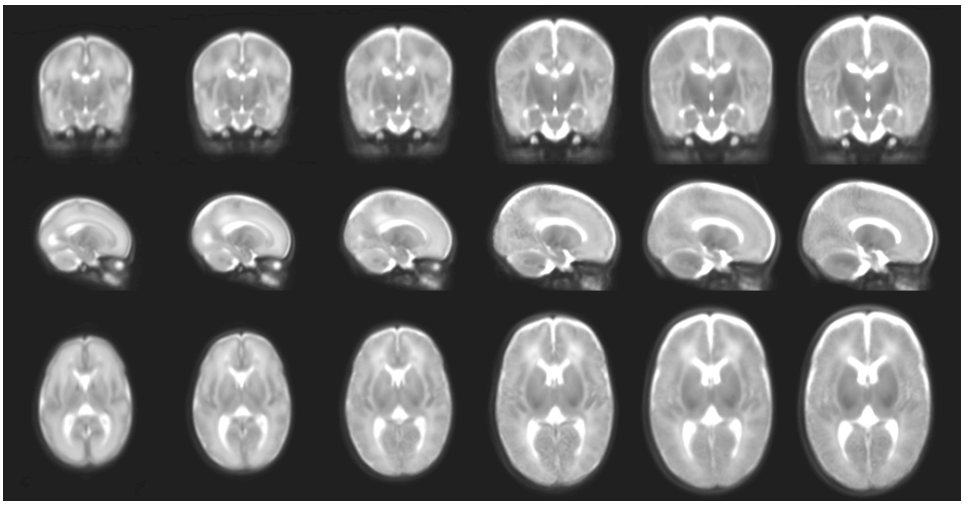

Figure 5.2.1: T2-weighted average MRIs for example ages (29, 32, 35, 38, 41 and 44 weeks PMA). In the first row a coronal view of the MRI volume is shown, the second row shows a sagittal view and the third row shows an axial view. Note the presence of the extra-cerebral tissues.

As part of the pre-processing of the MRI volumes, a structural segmentation of the different brain tissues into 87 regions was performed. This segmentation was carried out using the approach of Ledig et al. (2012). The method employs a set of MRI atlases and corresponding manual segmentations for all 87 structures. For each target image, all atlas MRI images are registered to the target using a non-rigid registration. This

results in a set of deformations that can be used to map the atlas structures onto the target's native space. For each structure, a voxel-wise spatial prior probability map is estimated by averaging the corresponding masks of that structure for all the mapped atlases. The spatial priors are then used in conjunction with the target images' intensity information to optimize the segmentation of all 87 structures.

Each brain-extracted individual MR scan was thus segmented in its native space. The resulting segmented images underwent an affine transformation to the average T2 age-matched image. The final structural segmentation mask for each age was then obtained by assigning each voxel to the region that it is most commonly defined as in the individual segmentations.

5.2.3 Multi-layer tissue mask

To produce a head model of fundamental tissue types, for which the optical properties of absorption coefficient and scattering coefficient are available, the 87 identified brain regions were divided into 5 tissues: cerebrospinal fluid (CSF), grey matter (GM), white matter (WM), as well as cerebellum and brainstem.

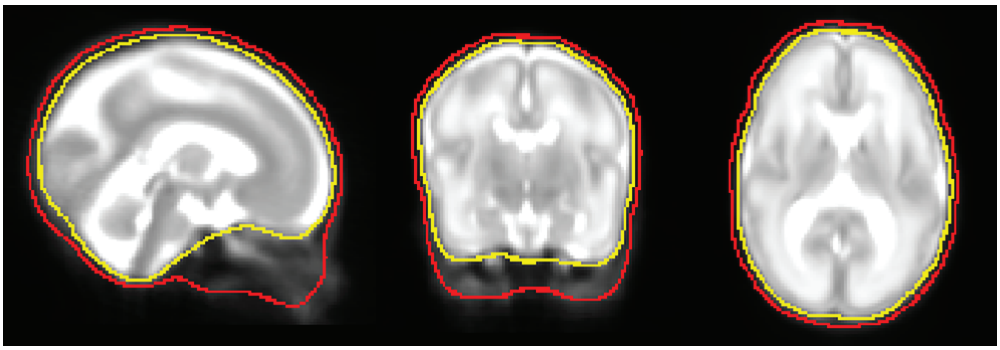

Figure 5.2.2: T2-weighted average MRI for example age (29 weeks PMA) overlaid with the borders of the outer scalp (in red) and inner skull (in yellow) masks obtained in FSL. Sagittal, coronal and axial view are displayed.

The segmentation of the scalp and skull was performed with FSL (http://fsl.fmrib.ox.ac.uk/fsl/fslwiki/) on the average T2 image for each

age. The BET (Brain Extraction Tool) routine was used, including the function BET2, which isolates the brain, and the function BETSURF, which separates the outer scalp and inner skull surfaces (Jenkinson et al., 2005) (Fig. 5.2.2). Since the scalp and skull in neonates are very thin and are difficult to distinguish in T2 images, the scalp and skull tissues were merged into a single extra-cerebral tissue layer (ECT). These segmentation processes identified the brain and the inner skull surface. The extra-cerebral CSF layer was defined by the gap between the outer grey matter and the inner skull surfaces. Voxels between these two structures were labeled as CSF.

The final multi-layer tissue masks (consisting of extra-cerebral, CSF, GM, WM, cerebellum and brainstem tissues) are displayed in Fig. 5.2.3 for a sub-set of ages. All multi-layered tissue masks were inspected by a clinical neonatologist in order to prevent major segmentation errors and insure the development of the brain is accurate.

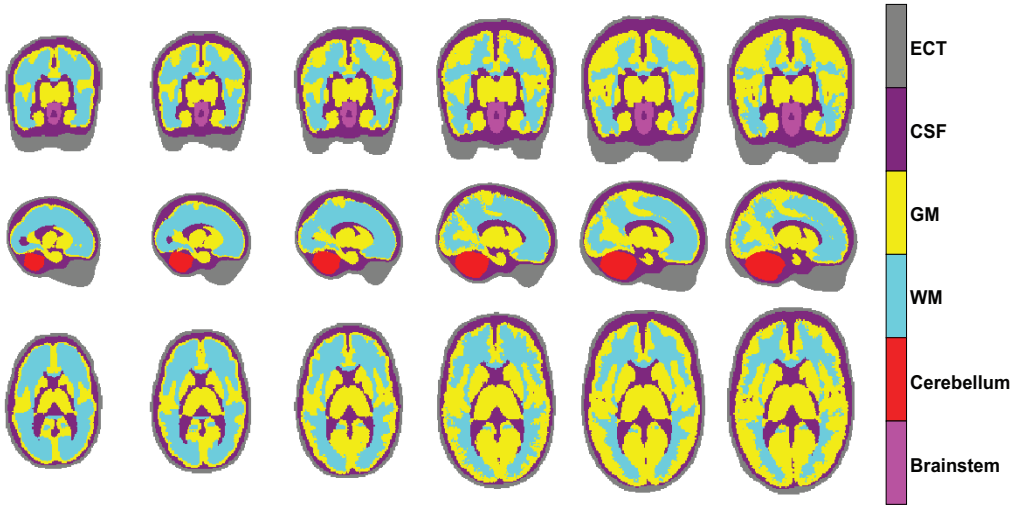

Figure 5.2.3: Multi-layered tissue masks for example ages (29, 32, 35, 38, 41 and 44 weeks PMA). The first row shows a coronal view of the mask, the second row shows a sagittal view and the third an axial view. In grey is displayed the extra-cerebral tissue (ECT), in purple the CSF, in yellow the GM, in cyan the WM, in violet the brainstem and in red the cerebellum.

5.2.4 VOLUMETRIC TETRAHEDRAL MESH CONSTRUCTION

A high-density, volumetric, tetrahedral multi-layered mesh was created for each of the 16 ages using the multi-layered tissue mask described above. This was performed using the iso2mesh toolbox (Fang and Boas, 2009b), with the CGAL mesher option (http://www.cgal.org), which involves using the Computational Geometry Algorithms Library for direct mesh generation. This is a C++ library that allows fast creation of a complex mesh from a multi-region volume. The maximum element volume size was set to 1 mm^3 and the maximum radius of the Delaunay sphere was set to 1 mm. The tetrahedral meshes for a subset of ages are shown in Fig. 5.2.4.

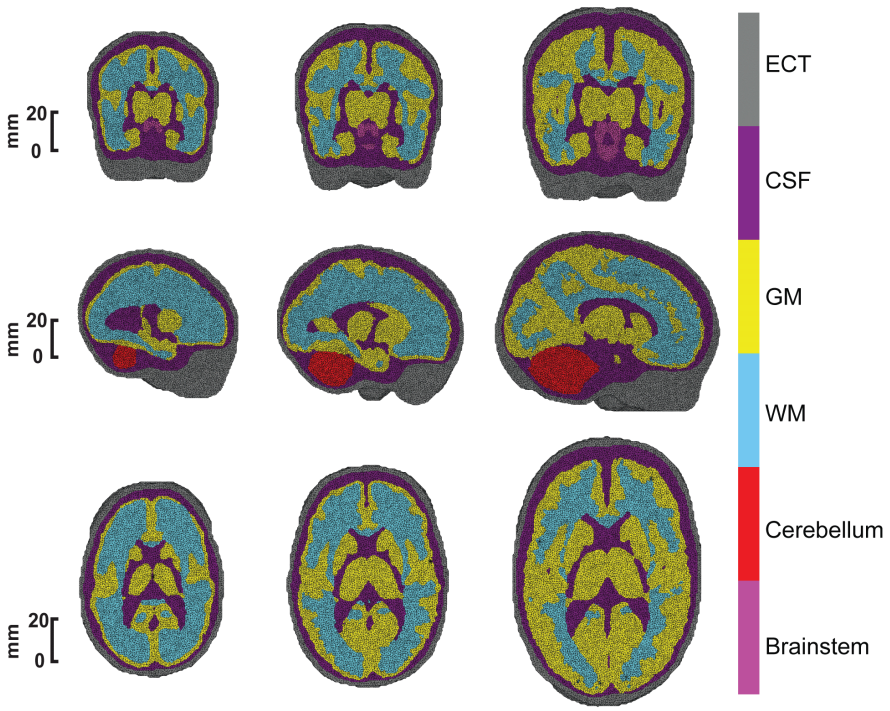

Figure 5.2.4: Multi-layered volumetric tetrahedral meshes for example ages (29, 35, and 44 weeks PMA). The first row shows a coronal view of the mesh, the second row shows a sagittal view and the third show an axial view. In grey is displayed the extra-cerebral tissue (ECT), in purple the CSF, in yellow the GM, in cyan the WM, in violet the brainstem and in red the cerebellum.

In order to assess the quality of the created volumetric meshes, the Joe-Liu quality index was computed for every tetrahedron for all ages (Liu and Joe, 1994):

$$q_{vol} = \frac{12 \cdot (3 \cdot vol)^{\frac{2}{3}}}{\sum\limits_{0 \leqslant i < j \leqslant 3} l_{i,j}^2} \tag{5.1}$$

where vol is the tetrahedral volume and $l_{i,j}$ are the lengths of the edges of the tetrahedron. This metric is equal to 1 for equilateral tetrahedra and tends to 0 for degenerated tetrahedra. A high quality mesh is expected to score high q_{vol} values.

5.2.5 GM, WM AND SCALP SURFACE MESH CONSTRUCTION

A surface mesh for each of the GM, WM and scalp layers was created for each age of the atlas using the iso2mesh toolbox. High-density GM and scalp surface meshes were created from the tissue masks using the CGAL meshing procedure. In order to preserve the finer details of the WM layer, particularly the corpus callosum, it was necessary to first produce a high-density volumetric mesh of the WM tissue. The WM surface mesh was then extracted by selecting only the external nodes of the volumetric mesh.

In order to obtain surface meshes with a density low enough to make their use computationally straightforward, but high enough to maintain the anatomical details of the tissues, a down-sampling procedure was performed; only 30% of the initial nodes were kept. A low-pass filter, which Bade et al. (2006) have shown to be the best volume preserving smoothing algorithm, was also applied to smooth the surface. This process better preserves anatomical details than the direct production of a lower-density surface mesh. The mean face area of each mesh before and after the down-sampling and smoothing procedure was computed, as was the mean Hausdorff distance across ages between the high-density mesh and the down-sampled and smoothed mesh. The results confirmed that the macrostructure of each mesh was preserved by the down-sam-

pling and smoothing procedure. The mean increase in face area was < 1 mm^2, and the mean Hausdorff distance across ages between the meshes was less than 2 mm for the scalp and GM meshes and less than 2.6 mm for the WM mesh. An example of the surface mesh for all three layers is shown in Fig. 5.2.5 for selected ages.

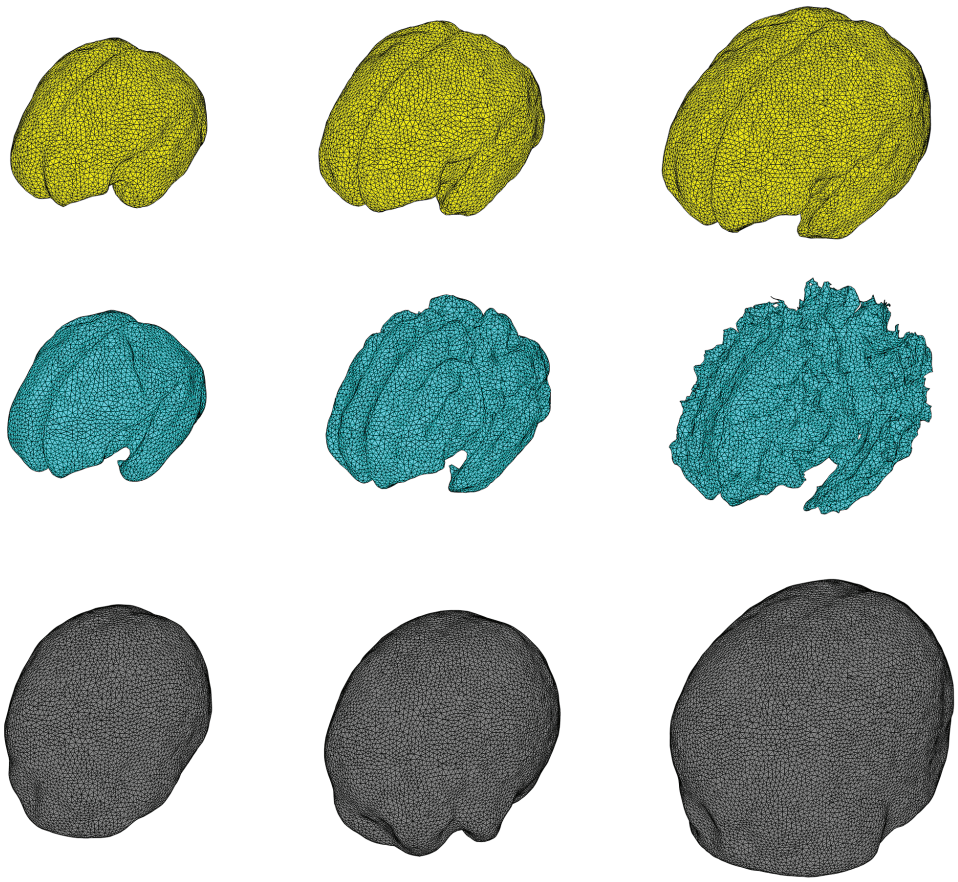

Figure 5.2.5: Surface meshes for GM, WM, and scalp for example ages (29, 35 and 44 weeks PMA). In the first row the GM surface mesh is displayed for each age. In the second row, the WM surface mesh is displayed for the three selected ages. In the third row, the scalp surface mesh is shown for the three ages. Note the increasing convolution of the WM surface, and to a lesser extent the GM surface, with age.

The quality of the surface meshes was assessed by computing for every

triangle of each mesh the following quality index (Field, 2000):

$$q_{surf} = \frac{4 \cdot \sqrt{3} \cdot A}{l_1^2 + l_2^2 + l_3^2} \tag{5.2}$$

where A is the area of the triangle and $l_{1,2,3}$ are the lengths of its sides. As for the volumetric mesh case, this quality metric equals 1 when the triangle is equilateral, and tends to 0 for a degenerated triangle. A high quality mesh should give a high q_{surf} values.

5.2.6 Cranial landmarks and 10-5 positions

For every age, the coordinates of cranial landmarks corresponding to the inion (Iz), nasion (Nz) and left and right pre-auricular points (ALAl and ARAr) were manually determined using FreeSurfer (http://surfer.nmr.mgh.harvard.edu/) to visualize the surface. The 3D rendering tool creates a 3D rendering of the scalp surface starting from the average T2 MRI volume, which allows the ears and the nose of the average MRI volume to be identified. The landmark coordinates derived from the T2 image are then transferred to the volumetric head mesh; the coordinates of the nearest node of the mesh are assigned as the final landmarks' coordinates.

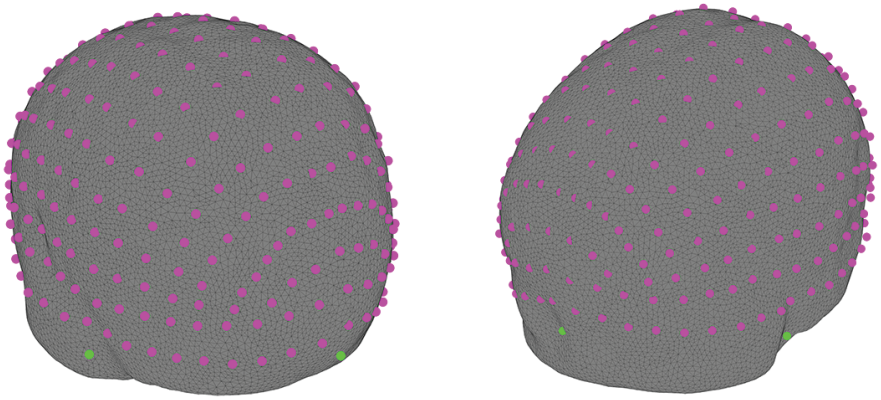

Figure 5.2.6: Cranial landmarks (in green) and 10-5 positions (in magenta) superposed on the 44-weeks baby scalp mesh. In the left figure, Al, and inion can be observed, while nasion is visible in the right figure.

The 10-5 system is an EEG-based convention for electrode positioning (Oostenveld and Praamstra, 2001). It is a high-density system, which comprises 345 scalp locations. Since many researchers in the DOT community use the 10-5 system or lower density versions (10-10 or 10-20) to position their optodes (Jurcak et al., 2007), the coordinates of the corresponding 10-5 locations have been calculated for every age. Given three points on the mesh surface (for example Al, Ar and the vertex, Cz), a plane can be created and the intersection between the plane and the outer surface of the volumetric mesh (plus or minus some threshold width α) defines a curve along the scalp surface (in this example, the curve from Al to Ar via Cz). Each curve was smoothed using a 3D spline interpolation using only 1 in 4 of the surface nodes, which intersect the plane. The 10-5 locations along that curve can then be calculated by dividing the total length of the curve into 5% intervals.

An example of the 10-5 locations and the cranial landmarks positioning on a head model for a single age are shown in Fig. 5.2.6.

5.3 Demonstration of the head models in use

As a demonstration of the application of the proposed head models to diffuse optical imaging, three different methods of modeling photon transport and solving the forward problem were employed. In the tetrahedral meshes, both a Monte Carlo approach (using the MMC package (http://mcx.sourceforge.net)) and the Finite Element Method (using TOAST (http://web4.cs.ucl.ac.uk/research/vis/toast)) were applied. A voxel-based Monte Carlo method (using the MCX package (http://mcx.sourceforge.net)) to model photon transport and solve the forward problem in the multi-layer tissue mask rather than in tetrahedral mesh was also applied. A simulated set of sources and detectors were placed on the Al-Ar line (sources at C5, C1, C2 and C6 and detectors at T7, C3, C4 and T8), to provide a total of 4 channels with same source-detector separation (every detector was measuring light coming from a single source). Optical properties were assigned to every tissue

layer as follows (absorption coefficient (mm^{-1}), reduced scattering coefficient (mm^{-1}) and refractive index, respectively): 0.017, 1.75, 1.3 for the scalp layer, 0.0041, 0.032, 1.3 for the CSF layer, 0.048, 0.5, 1.3 for the GM layer, and 0.037, 1, 1.3 for the WM, cerebellum and brainstem layers (Dehaes et al., 2013).

5.4 RESULTS

Age (week)	**N nodes**	**N faces**	**N elements**	**Mean Voronoi volume ± std (mm^3)**	**Mean q_{vol} ± std**
29	382625	491958	2284103	0.836 ± 0.256	0.830 ± 0.104
30	385532	495868	2300908	0.837 ± 0.255	0.831 ± 0.103
31	401735	531426	2400077	0.835 ± 0.253	0.830 ± 0.104
32	423051	560160	2528645	0.835 ± 0.254	0.830 ± 0.104
33	442782	591316	2647723	0.836 ± 0.253	0.830 ± 0.104
34	481464	634968	2882826	0.836 ± 0.253	0.830 ± 0.104
35	512514	689286	3072358	0.835 ± 0.254	0.828 ± 0.105
36	566593	761656	3401223	0.836 ± 0.254	0.828 ± 0.105
37	636061	862276	3824980	0.833 ± 0.256	0.827 ± 0.107
38	716509	962526	4314759	0.831 ± 0.259	0.826 ± 0.107
39	784391	949436	4726239	0.839 ± 0.255	0.829 ± 0.106
40	805537	933424	4852397	0.844 ± 0.251	0.830 ± 0.104
41	833782	951462	5025079	0.844 ± 0.253	0.830 ± 0.105
42	866808	970150	5227709	0.846 ± 0.251	0.831 ± 0.104
43	889455	1006512	5366655	0.843 ± 0.255	0.829 ± 0.106
44	906023	1055900	5469235	0.840 ± 0.256	0.828 ± 0.107

Table 5.4.1: For every age, the properties of the volumetric mesh (number of nodes, faces, elements and the Voronoi volume) are reported. In the last column, the Joe-Liu quality index is also shown.

In table 5.4.1 a summary of the properties and quality indices of the computed volumetric meshes is reported for each age. The total number of nodes, faces and elements is also reported. As expected, the number of nodes, faces and elements increases with age. In the 5th column of the table the mean Voronoi volume (across all nodes) with its standard deviation is shown. For all ages, the volume is lower than 1 mm^3, confirming

the high density of the mesh. In the last column the mean Joe-Lui quality index q_{vol} (computed across all tetrahedrons) is reported with its standard deviation. All meshes achieve a high quality score. The lowest q_{vol} index observed in any of the meshes is 0.1. The vast majority of elements are close to equilateral (88.4% of the q_{vol} indices are higher than 0.7) and no elements are completely degenerated.

A summary of the properties of the GM, WM and scalp surface meshes is reported in table 5.4.2. The number of nodes and faces, as well as the mean area of the triangles with its standard deviation, is shown for every age. As in the volumetric case, the number of nodes and faces generally increases with age.

	GM Surface Mesh			WM Surface Mesh			Scalp Surface Mesh		
Age (week)	**N nodes**	**N faces**	**Mean area ± std (mm^2)**	**N nodes**	**N faces**	**Mean area ± std (mm^2)**	**N nodes**	**N faces**	**Mean area ± std (mm^2)**
29	6037	12078	1.335 ± 0.406	8794	17584	1.283 ± 0.385	7916	15828	1.456 ± 0.424
30	5820	11640	1.404 ± 0.424	8950	17906	1.293 ± 0.378	8199	16394	1.411 ± 0.411
31	6413	12830	1.370 ± 0.422	9951	19904	1.272 ± 0.387	8217	16430	1.447 ± 0.420
32	6773	13570	1.378 ± 0.422	10723	21442	1.256 ± 0.382	8613	17222	1.434 ± 0.410
33	7471	14946	1.347 ± 0.409	11520	23056	1.231 ± 0.389	8980	17956	1.430 ± 0.413
34	8017	16050	1.329 ± 0.419	12636	25294	1.211 ± 0.386	9549	19094	1.420 ± 0.413
35	8577	17162	1.376 ± 0.414	13949	27910	1.181 ± 0.393	9927	19850	1.431 ± 0.413
36	10457	20926	1.248 ± 0.382	16002	31997	1.150 ± 0.396	10469	20934	1.450 ± 0.424
37	10831	21678	1.310 ± 0.404	18350	36711	1.113 ± 0.406	11344	22684	1.447 ± 0.418
38	11285	22574	1.355 ± 0.430	21040	42205	1.073 ± 0.411	12274	24544	1.453 ± 0.413
39	11480	22956	1.393 ± 0.424	19678	39424	1.125 ± 0.405	13090	26176	1.452 ± 0.417
40	11813	23626	1.389 ± 0.421	18983	37992	1.163 ± 0.404	13453	26902	1.448 ± 0.417
41	11885	23766	1.396 ± 0.419	18794	37630	1.163 ± 0.405	13721	27438	1.447 ± 0.416
42	12195	24394	1.390 ± 0.420	19189	38448	1.149 ± 0.406	13933	27862	1.459 ± 0.423
43	12444	24888	1.383 ± 0.422	19825	39745	1.114 ± 0.413	13938	27872	1.480 ± 0.432
44	12916	25836	1.356 ± 0.421	21440	43001	1.073 ± 0.424	14306	28608	1.462 ± 0.424

Table 5.4.2: Number of nodes and faces, as well as mean area of the triangles and its standard deviation, for all ages for the GM, WM and scalp surface meshes.

The results achieved by the GM, WM and scalp surface meshes for the quality index q_{surf} are reported in table 5.4.3. All the surface meshes are of a very high quality. The lowest q_{surf} index observed in any of the surface meshes is 0.02. The vast majority of faces are equilateral (97.9% of the q_{surf} indices are higher than 0.7) and no faces are completely degenerated.

	GM Surface Mesh	WM Surface Mesh	Scalp Surface Mesh
Age (week)	**Mean** q_{surf} **± std**	**Mean** q_{surf} **± std**	**Mean** q_{surf} **± std**
29	0.928 ± 0.078	0.928 ± 0.076	0.931 ± 0.070
30	0.929 ± 0.073	0.931 ± 0.073	0.931 ± 0.071
31	0.927 ± 0.077	0.928 ± 0.073	0.931 ± 0.071
32	0.928 ± 0.075	0.929 ± 0.072	0.933 ± 0.069
33	0.928 ± 0.075	0.925 ± 0.078	0.932 ± 0.068
34	0.925 ± 0.080	0.926 ± 0.079	0.931 ± 0.070
35	0.928 ± 0.075	0.921 ± 0.083	0.933 ± 0.069
36	0.927 ± 0.074	0.919 ± 0.090	0.931 ± 0.070
37	0.927 ± 0.077	0.911 ± 0.099	0.932 ± 0.069
38	0.924 ± 0.080	0.905 ± 0.107	0.933 ± 0.069
39	0.927 ± 0.075	0.913 ± 0.096	0.932 ± 0.069
40	0.928 ± 0.074	0.918 ± 0.092	0.932 ± 0.070
41	0.928 ± 0.075	0.917 ± 0.093	0.934 ± 0.068
42	0.928 ± 0.076	0.916 ± 0.093	0.932 ± 0.070
43	0.927 ± 0.076	0.909 ± 0.103	0.932 ± 0.070
44	0.926 ± 0.078	0.902 ± 0.113	0.932 ± 0.070

Table 5.4.3: For every age the mean value of q_{surf} and its standard deviation are displayed for GM, WM and scalp surface meshes.

In Fig. 5.4.1 the results achieved with both MMC (a)), TOAST (b)) and MCX (c)) are displayed for a representative age, in the form of the sensitivity distribution of the 4 channels of our simulated optode array. The three forward models are comparable, with a high sensitivity observed near the location of each optode and a decreasing sensitivity with depth. Note the characteristic shape of the photon measurement density function. Such forward solutions can be inverted and used to reconstruct images of optical data acquired with the corresponding optode configuration.

5.5 Conclusive considerations and remarks

The creation of the 4D optical head model described here is an important step in the development of DOT in neonatal imaging. It allows researchers to choose, for every newborn measured with DOT, an accurate, age-matched head model and perform the image reconstruction process

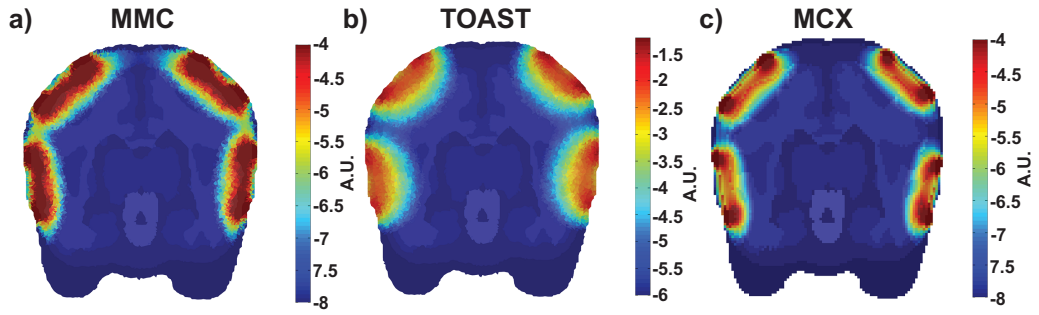

Figure 5.4.1: a) MMC, b) TOAST and c) MCX simulation results. A mesh cut at the Al-Ar plane of the 35 week baby is shown. The log of the sensitivity is displayed for the 4 channels in each case. High sensitivity indicates that a high number of photons pass through that element on their way to a detector. Note how the sensitivity decreases with increasing depth.

using an anatomy that is as close as currently possible to that of the studied infant. This constitutes the current best-practice approach to diffuse optical image reconstruction for the neonatal population when individual MRI data is not available.

Image reconstruction for diffuse optical techniques requires an accurate forward model, which, by modeling photon migration through the tissues from the array of sources predicts how the DOT data will change given a change in tissue optical properties. The more realistic the head model, the more accurate the forward model and the more accurate the resulting DOT images. The proposed 4D head model provides a realistic, high quality volumetric head mesh for every age from 29 weeks PMA to 44 weeks PMA, at one-week intervals (Fig. 5.2.4).

5.5.1 From baby's cranial landmarks to atlas registration to forward problem solutions

The process of applying this optical head model first requires knowledge of the locations of the cranial landmarks and the source and detector fibers on the scalp of the infant under examination. These positions can be measured using an electromagnetic tracking system or via photogrammetry. As an alternative to measuring each fiber position individually,

which can be time consuming, it is possible to position the fibers relative the subject's 10-5 locations. As these positions are provided directly for each age of the presented 4D head model, the position of each source and detector fiber on the mesh can be easily determined.

Once the cranial landmarks have been measured, the age-matched head model must be registered to the individual baby's head size and shape. The simplest approach to this registration is to define an affine transformation matrix between the baby's measured cranial landmarks and the equivalent locations provided for each age of the head model (Singh et al., 2005; Tsuzuki et al., 2012).

Once the age-matched head mesh has been registered to the subject, and the source and detector locations on the mesh have been determined, relevant optical properties can be assigned to the tissues composing the volumetric head mesh, to take into account the different absorption and scattering coefficients of the different tissue types. It is known that adult and neonatal tissues have different optical properties (Fukui et al., 2003). Selecting accurate optical properties is important, but the availability of neonatal optical properties is still very limited. A sensitivity analysis to quantify the errors introduced by the use of incorrect optical properties using the head models presented here would be beneficial, as would thorough measurement of the optical properties of neonatal tissues across the NIR spectrum.

A Monte Carlo simulation (performed using, for example, the MMC package (Fang and Kaeli, 2012; Fang, 2010) or the finite element method FEM (performed using, for example, the TOAST package (Arridge et al., 1993; Schweiger et al., 1995), can be used to model photon migration in the volumetric head model mesh and to produce a forward model (Arridge, 2011; Gibson et al., 2005) (Fig. 5.4.1).

Alternatively, the forward model can be solved, in a computationally efficient and accurate way using the Boundary Element Method (BEM) (Elisee et al., 2011). BEM solves the differential equations of the forward problem using Green's theorem to transform them into a set of integral equations defined only on the surfaces of layers within a volume. Us-

ing this approach, the matrix dimensionality of the forward problem is considerably reduced. This method assumes that the volume between two surfaces is a piece-wise constant domain and therefore BEM does not require a volumetric mesh but only surface meshes. This is one further reason why the package described here includes scalp, GM and WM surface meshes.

Another alternative for the forward model solution is to use a voxel-based Monte Carlo approach (performed using the MCX package for example (Fang and Boas, 2009a)) (Fig. 5.4.1). This is one reason why the package described here includes the multi-layer tissue mask, which can easily be used to run the voxel-based Monte Carlo simulation.

The package proposed here, therefore, allows the user to choose their preferred method of solving the forward problem. As shown by Fig. 5.4.1, the forward solutions produced by FEM and Monte Carlo approaches will be different, simply because these algorithms are based on fundamentally different models. The difference between the results obtained using MMC and MCX, is likely due to an inaccurate geometric representation of the head tissues in the voxel space, which may negatively impact the accuracy of the solution (Fang, 2010). The strength of mesh-based approaches is the ability to model continuously varying complex media.

5.5.2 Neonatal brain development in MRIs and meshes

The neonatal brain develops extremely quickly. In Fig. 5.2.1 it is evident how the brain and head of the newborn is not only increasing in size going from 29 weeks PMA to 44 weeks PMA, but also the shape and contrast between different tissues are changing rapidly. It is clear in Fig. 5.2.1 that the T2 image of a term baby (39-41 weeks PMA) exhibits higher contrast between GM and WM compared to the T2 image of a preterm newborn (29 weeks PMA), where the high water content produces long T1 and T2 times and thus a low signal in the WM part of the image.

The development of the brain is even more evident in the GM and WM

surface meshes shown in Figure 5.2.5. The cortical surface of a 29 week PMA infant is relatively smooth (Battin and Rutherford, 2002) but cortical folds rapidly develop between 39 and 40 weeks PMA. The cortical folding apparent in the GM surface meshes is noticeably less than that of individual infant MRIs of ~ 35-44 weeks PMA. This detail is likely to have been lost in the averaging process used to obtain the atlas because of the large variability between different infants. However, the GM surface meshes do show the cortical folding increasing with age. The GM surface mesh for the 29 week baby is very smooth, while the GM surface mesh for a term baby (39-41 weeks PMA) clearly shows some of the main sulci in the parietal cortex and evidence of the central gyrus.

Although the average cortical meshes do not exhibit the sulci and gyri as clearly as an individual MRI of that age, the smoothing of these features due to the spatial averaging of T2 images is representative of the anatomical variation across infants at that age. While it would be possible to base each mesh on an individual (non-averaged) MRI that would maintain denser cortical folding, to reconstruct DOT images using such a mesh and present those images on those cortical folds would bias those images, and would ultimately be misleading.

The WM surface mesh displays a clear development from preterm to term neonates. The WM appears as a smooth surface in the extreme preterm baby, and this smoothness is likely due to both the underdevelopment of the WM and of the cortical GM, where folding has yet to take place. In the term baby, the GM folding has already started and consequently the boundary between the WM and GM becomes more complex, exhibiting higher curvature.

It is therefore clear the importance of using an anatomically age-matched head model to accurately perform DOT in the neonatal population.

5.5.3 Head models' limitations

The FSL approach used to isolate the scalp and skull has been validated in adults but has also been used previously with infants (Sanchez et al., 2012). Tissue contrasts in infant T2 MRI images are markedly different from those of the adult, and T2 images do not produce high contrast for extra-cerebral tissues. The BETSURF tool works preferentially with T1 images, and its performance is improved using both T1s and T2s. In the present case, only T2 images were available; T2 contrast images are the most commonly applied to neonates in clinical circumstances. As a result it is possible that the BETSURF procedure overestimates or (more likely) underestimates the thickness of the extra-cerebral layer. The segmented tissue mask for each age was checked for consistency and precision by superposing it on the original T2 atlas image, and the results appeared accurate. If both T1 and T2 images were available, the segmentation of the extra-cerebral tissues would likely be more accurate and it may even be possible to separate the scalp and skull layers. In the future it may be possible to improve the identification of extra-cerebral tissues by designing an MRI sequence that is specifically tuned to the problem of seeking accurate optical head models.

The T2 images from individual infants were brain co-aligned in order to obtain an average T2 image for each age. As a result, there is greater spatial variability in structures which are distant from the brain. This particularly affects the lower regions of the head, which exhibit poor contrast in the average T2 images. As a result, the shape of the external surface of the extra-cerebral tissue layer on the under-side of the head is not reliable. However, this inaccuracy will have no impact on optical brain imaging applications.

Dehaes et al. (2011) have shown the importance of including the temporal fontanel in the model of the newborn skull by assigning it the optical properties of cartilage instead of bone. In order to distinguish the fontanel from the skull a CT scan (X-Ray Computed Tomography) is necessary, as the two tissues are generally indistinguishable to standard MRI.

Because of the use of ionizing radiation, CT is not usually performed clinically on infants. For this reason, there are few CT volumes available and it has not been possible to account for the fontanels in the proposed model.

5.5.4 Standard coordinate system for neonatal atlases

In studies of the adult brain, a standardized coordinate system, such as the Talairach or MNI systems, can be used to analyze multi-subject data in a common coordinate space (Chau and McIntosh, 2005). Images of an individual are transformed to the common space to allow for inter-subject and inter-study comparisons. A standard newborn MRI atlas, like that built by Kuklisova-Murga sova et al. (2011), should ideally provide the equivalent standardized space for newborns. Unfortunately, there is still debate in the MRI community about which newborn MRI atlas should define the reference space and how these coordinates will be transformed to be universally applied to different ages (Kazemi et al., 2007).

A simpler approach is, of course, to use the adult MNI space for infant studies. By transforming each infant brain to the adult MNI space, a location in the infant brain can be given in adult MNI coordinates, and the anatomy will broadly match. For example, a coordinate which identifies a location on the post-central gyrus in adults will also represent, approximately, a location on the post-central gyrus in infants. However, comparisons of the physiological importance of spatially equivalent brain regions between the infant and adult populations are clearly flawed (Wilke et al., 2003). To transform the proposed models to match adult MNI coordinates would, of course, inflate the infant head models to the size of an adult brain, which is clearly not appropriate for diffuse optical approaches. Instead, the presented 4D infant head model is based on MRI data with the same axis definitions as the MNI coordinate system but without being transformed to match the adult anatomy. A coordinate in the presented meshes will therefore represent a very different physiolog-

ical location than the same coordinate in an MNI-registered adult.

5.5.5 Head models' additional applications

An additional application of the proposed 4D optical head model is related to the important issue of optode positioning. Many applications of diffuse optical techniques target a very particular, and known, location in the brain. In such studies the goal is not to map a functional response, but to examine the response of a certain region to a particular stimulus. As it is common that the number of DOT channels is limited, determining where to place the sources and detectors on the scalp so as to best sample the region of interest is very important. This optical head model can be utilized to optimize probe location. By modeling photon migration for a variety of source and detector arrangements, the optical fiber array that best samples a given brain region can be determined. It is also possible to imagine an approach that takes advantage of the reciprocity of photon migration in tissue to explicitly calculate the best source and detector positions for sampling a given brain coordinate, rather than producing multiple models and choosing the most suitable.

5.5.6 Final remarks

In conclusion, in this chapter a 4D optical head model package for preterm through to term newborns ranging from 29 to 44 weeks PMA, at one week intervals, has been presented. This atlas is freely available online (www.ucl.ac.uk/medphys/research/4dneonatalmodel) and provides, for every age:

1. A multi-layered tissue mask including WM, GM, CSF, cerebellum, brainstem and extra-cerebral tissues
2. A volumetric high-density tetrahedral head mesh
3. GM, WM and scalp surface meshes
4. Cranial landmark coordinates and 10-5 locations.

The package allows researchers to select, for every newborn under examination, an accurate age-matched head model, and thus aged-matched anatomy. This allows for maximally accurate optical image reconstruction and anatomically meaningful, uniform presentation of the resulting images. Ultimately this improves the quality, accuracy and interpretability of DOT images and will aid their application to neonatal medicine.

PART III
Application of the new methodologies and tools to empirical neural activation

6

The role of M1 and SMA in simple motor tasks

Studies employing functional magnetic resonance imaging (fMRI) have highlighted a covariation between the amplitude of hemodynamic responses recorded in motor processing areas and the duration of a motor task. When movement duration exceeds 1s (Glover, 1999), long duration movements are generally associated with hemodynamic responses of larger amplitude relative to movements of short duration. Movement duration, however, appears to modulate differently the hemodynamic response amplitude of two distinct areas underpinning motor action, that is, the primary motor (M1) and supplementary motor (SMA) areas (Miller et al., 2001).

Birn et al. (2001), for instance, monitored the hemodynamic responses of 3 participants performing a bilateral finger tapping task for 4 different durations (i.e., 500, 1000, 2000 and 4000 ms), and found a positive cor-

relation between task duration and hemodynamic response amplitude in M1, while such correlation was nil in SMA. Based on this finding, these authors put forth a serial two-stage functional architecture of the interplay between M1 and SMA ascribing to SMA a first stage of motor planning, and to M1 a subsequent stage of motor execution required by the finger tapping task. Accordingly, neural activity in SMA would be affected by factors underlying task preparation prior to movement initiation, whereas M1 would be affected by factors underlying task execution, such as task duration.

A different account of the interplay between M1 and SMA has been proposed by Kasess et al. (2008), who had participants performing (or imagining to perform) a brief right-hand finger movement at the end of a countdown sequence of numbers while fMRI data were recorded at higher-than-standard rate to monitor subtle changes in cortical hemodynamics. In contrast to Birn et al. (2001)'s proposal, Kasess et al. (2008)' results suggested that M1 and SMA subserve motor task execution interactively, via a closed-loop control circuit composed of basal ganglia-thalamo neurons connecting M1 and SMA. As a result, the activity of SMA and M1 would be temporally intertwined (and not discretely separable) throughout the execution of a movement. Thus, although SMA would be primarily involved in motor planning, its activity would also reflect an active supervising role during motor processing occurring in M1. Therefore, both areas should be concomitantly affected by task duration.

Aim of the present study was to pit these two accounts one against the other using fNIRS and exploiting one of its great advantage compared to fMRI: its higher temporal resolution, which enables a finer-grained monitoring of the temporal characteristics of the hemodynamic response compared to fMRI. Thanks to this and by removing the physiological noise contamination with the application of ReMCoBA, the algorithm proposed in chapter 3, it was possible to detect subtle temporal differences between HRs measured in M1 and SMA, which allowed to corroborate the second of the two accounts (Brigadoi et al., 2012).

6.1 DATA

Seven male students (6 right handed) at the University of Padova (mean age 29.3, range 24-35) participated in the experiment after providing informed consent. To note, the left-handed participant was not excluded from analysis in order to prevent lack of power. Furthermore, when examined in isolation, the pattern of cortical activity exhibited by this left-handed participant was not dissimilar from that observed in right-handed participants. All participants had normal or corrected to-normal vision. None of them reported a history of neurological or psychiatric disorders or was under medication at the time of testing.

Each participant was seated on a comfortable chair in a dimly lit room in front of a LCD monitor placed at a viewing distance of 60 cm. The index and middle fingers of the right hand were placed on the '0' key in the numeric keypad. Each trial began with a central fixation point, which was followed 1 s later by the instruction 'Press 0' at the center of the screen. At that point, participants had to press the '0' key using both fingers as quickly as possible, and to release the key upon the presentation of a 'Stop' signal, which was displayed unpredictably and with equal probability after 1 s on short-duration trials, or after 3 s on long-duration trials (Fig. 6.1.1). Given the somatotopic organization of neurons in the motor areas under examination in the present study, the expedient of asking participants to respond using two fingers was adopted in order to maximize the probability to detect a reliable hemodynamic response from a larger portion of the motor cortex than it would be possible by employing just one finger. An inter-stimulus interval of 15 s followed the key release. Participants performed a single block of 80 experimental trials.

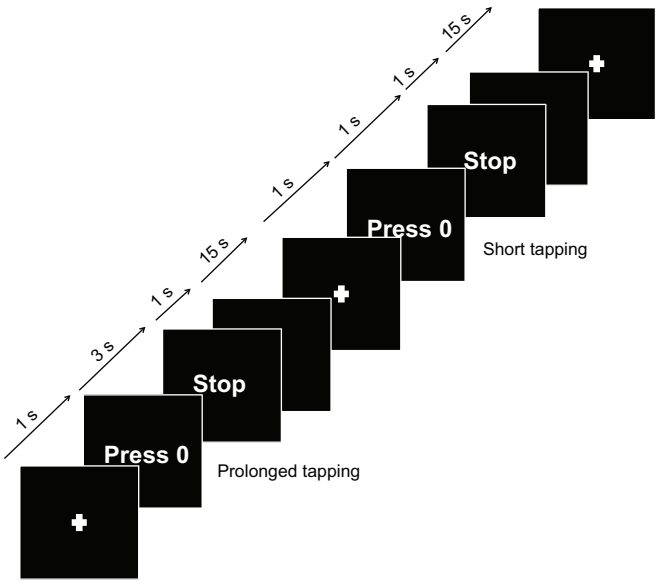

Figure 6.1.1: A schematic representation of the paradigm used.

6.2 Probe placement and fNIRS data acquisition

Hemodynamic activity was recorded with a multi-channel frequency-domain NIR spectrometer (ISS ImagentTM, Champaign, Illinois), equipped with 20 laser diodes (690 nm and 830 nm) modulated at 110.0 MHz and four photomultiplier tubes (PMT) modulated at 110.005 MHz. A recent probe placement method (Cutini et al., 2011b) based on the correspondence between 10-20 points and the underlying cerebral regions was used. Sources (1-5) and detectors (A and B, left and right respectively) are shown in Fig. 6.2.1. In left hemisphere, source 4 was placed about 1 cm behind C1 (right: C2), while sources 5 and 3 were placed as close as possible to the notional line connecting Cz and C3 (right: C4). This created a triple spatial bind allowing the placement of the optodes in a reproducible and reliable way across participants. In particular, channels A-4 and B-4 were placed on M1, while channels A-1 and B-1 were placed on SMA (Sharp et al., 2010). All these channels had a source-detector distance of 3 cm. Sources 6 and detectors C and D, instead, with a source-detector distance of 0.7 cm, had the only task to detect physio-

logical noise oscillations coming from the scalp layer. Channels C-6 and D-6 are, indeed, the SS-channels. The optical signal detected by the PMTs was converted in concentration changes of HbO and HbR through the modified Beer-Lambert Law.

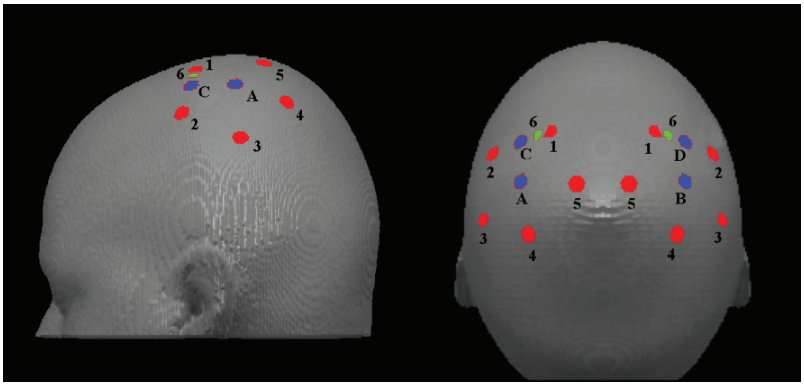

Figure 6.2.1: Sources (red and green) and detectors (blue) overlaid onto the scalp of the ICBM152 MRI template. Channels are located at the cerebral projection of the middle point between each source-detector pair. Channels C-6 and D-6 are the SS-channels, with a source-detector distance of 0.7 cm. All other channels (A-1, A-2, A-3, A-4 A-5 for the left hemisphere and B-1, B-2, B-3, B-4 B-5 for the right hemisphere) are standard channels with source-detector distance of 3 cm.

6.3 Signal processing and data analysis

Individual time-series were zero-mean corrected and band-pass filtered (0.01-3 Hz) in order to remove very slow drifts and high frequency noise. Starting from the 'Press 0' onset, the time-series were divided into segments of 12 s each. ReMCoBA, the algorithm proposed in chapter 3, was applied to minimize the impact of physiological noise oscillations and residual random noise on the optical signal and to recover the mean HRs for every channel and participant.

Peak amplitude and peak latency were computed for each individual mean hemodynamic response in a 2-10 s interval following the onset of 'Press 0'. Peak amplitude values were submitted to analysis of variance (ANOVA) considering task duration (short vs. long), hemisphere (left vs.

right), and channel (1 to 5) as within-subject factors. Peak latency values recorded from the left hemisphere (i.e., contralateral to the fingers used for tapping) were submitted to ANOVA considering task duration (short vs. long) and channel (1 to 5) as within-subject factors. Full Width Half Maximum (FWHM) values were computed for each mean hemodynamic response in the left hemisphere to estimate the difference in the temporal distribution of the hemodynamic activity between short- vs. long-duration trials. FWHM values represent a measure of how prolonged the hemodynamic activity is in each duration condition. Fig. 6.3.1 illustrates graphically how these three parameters (i.e., peak amplitude, peak latency and FWHM) have been computed. FWHM values were submitted to ANOVA considering task duration (short vs. long) and channel (1 to 5) as within-subject factors. A series of one-tailed t-tests was then conducted on the left hemisphere data to compare the two tapping durations based on peak amplitude, latency, and FWHM values recorded from each channel. Since HbR is notoriously characterized by a lower signal-to-noise ratio compared to HbO, the analyses concentrated on HbO data only.

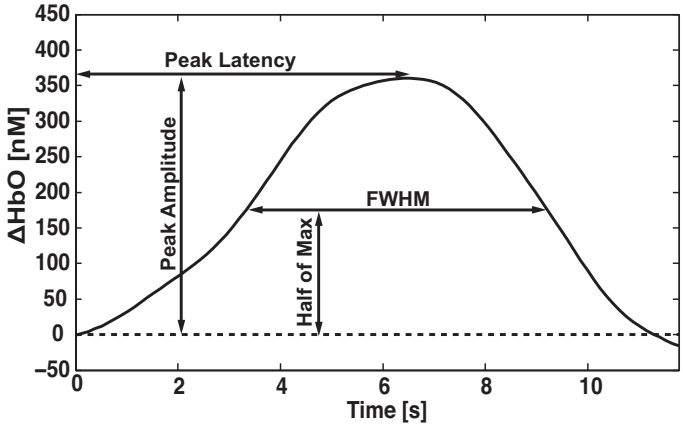

Figure 6.3.1: Sample curve to explain how peak amplitude, peak latency and FWHM were computed.

6.4 RESULTS

The analysis on the peak amplitude revealed a significant effect of task duration ($F(1,6) = 12.716$, $p < .05$) and a significant interaction between task duration and hemisphere ($F(1,6) = 14.337$, $p < .01$). Significant differences between the peak amplitude in the two tapping durations were found for all channels (min $t = 2.095$, max $p < .05$) located in the left hemisphere. The ANOVA on peak latency indicated a significant effect of task duration ($F(1,6) = 7.627$, $p < .05$), which was however confined to M1 (channel A-4: $t = 2.183$, $p < .05$). The analysis on FWHM values indicated a significant effect of task duration ($F(1,6) = 7.355$, $p < .05$), which was confined to M1 and close areas (channel A-4: $t = 1.981$, $p < .05$; channel A-5: $t = 3.996$, $p < .01$; channel A-3: $t = 2.265$, $p < .05$).

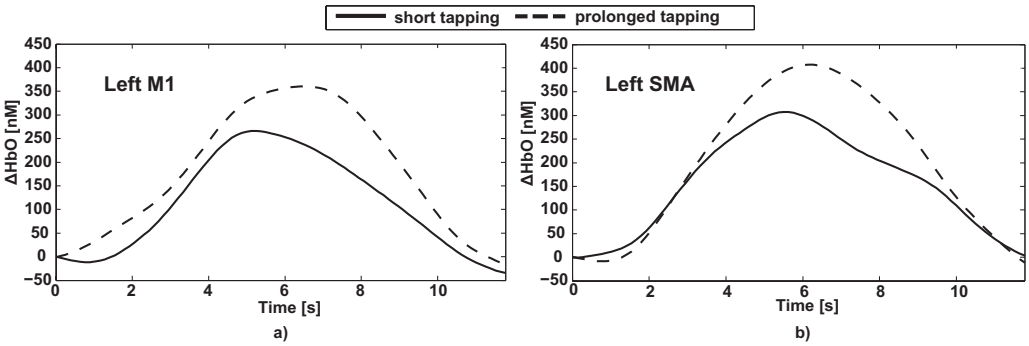

Figure 6.4.1: Mean hemodynamic responses in a) left M1 (channel A-4) and b) left SMA (channel A-1) during short (solid line) and prolonged (dashed-line) tapping.

Fig. 6.4.1 shows the mean hemodynamic responses in left M1 (channel A-4; MNI coordinates: -28, -19, 70, Brodmann Area 4) and left SMA (channel A-1; MNI coordinates: -22, 15, 64, Brodmann Area 6). As visual inspection of Fig. 6.4.1 suggests, and as the analysis on FWHM values supports statistically, M1 activity was temporally more sustained throughout the time-window of analysis on long- than short-duration trials, whereas the temporal profile of SMA activity was unaffected by task duration (t

$= 0.525$, n.s.).

6.5 Discussion

The primary aim of the present study was to investigate the presence of a functional dissociation between M1 and SMA, related to the duration of a simple motor task. Two different models derived from previous fMRI studies (Birn et al., 2001; Kasess et al., 2008) provided different accounts of the interaction between M1 and SMA in a motor task. Birn et al. (2001) proposed a serial, two-stage functional architecture of the interplay between M1 and SMA, with SMA involved in the planning of the movement and M1 in its execution. In this view, only M1 should be modulated by task duration. Kasess et al. (2008), in contrast, hypothesized that M1 and SMA are nodes of an interactive closed-loop control circuit subserving motor task execution, whereby effects of task duration should pervade the entire circuit.

Here, a relation between peak amplitude and task duration in both cortical areas was found, a result that provides direct support for Kasess et al. (2008)'s proposal. Interestingly a different temporal pattern emerged in the two examined cortical regions. While the entire temporal profile of M1 response was influenced by task duration, (i.e., M1 exhibited a more sustained and prolonged cortical activity during long duration than short duration tapping), the temporal profile of hemodynamic responses in SMA was in fact unaffected by task duration, as temporally overlapping responses were observed in SMA during the two tapping conditions (i.e., the initial and final parts of the hemodynamic responses are close to coincident).

In conclusion, a further co-registration study exploiting the spatial resolution of fMRI and the temporal resolution of fNIRS might be the optimal approach to better understand the controversial relation between such cerebral areas.

7

Visual short-term memory: An exploratory study

7.1 Visual short-term memory

Visual short-term memory (VSTM) is one of the three main memory systems, together with iconic memory and long-term memory. While iconic memory lasts a very limited period of time, decaying rapidly, visual short-term memory, instead, allows a non-permanent storage of visual information over an extended period of time, which can last seconds. The main difference between short-term and long-term memory has to be found, instead, in the restricted capacity of the former. Indeed, several behavioral studies have found the VSTM capacity limit to be around 3-4 items (Cowan, 2001; Luck and Vogel, 1997).

Although many neural circuitries, including frontal and prefrontal areas, show sustained activation during VSTM tasks, neurophysiological

studies have shown that the maintenance of information in VSTM and its capacity limit are probably supported by the intra-parietal (IPS) and intra-occipital (IOS) sulci (Cutini et al., 2011a; Robitaille et al., 2010; Todd and Marois, 2004). Indeed, activity in these cerebral regions is proportional to the number of items held in VSTM, up to the VSTM capacity limit, after that, the activity shows a plateau. Moreover, when the items to be maintained are presented in one of the two visual hemifields, the activity elicited in these posterior parts of the cortex is stronger in the region contralateral to the items to be held in memory.

Event-related potentials show a typical pattern of activity during a lateralized VSTM task: there is a larger negativity in the posterior electrodes contralateral to the side of presentation of the item to be memorized compared to the electrodes located ipsilaterally. This ERP response is called sustained posterior contralateral negativity (SPCN) and it is also modulated by the load: it increases in amplitude with the number of items to be held in memory, but only up to a certain limit, coincident with the VSTM capacity limit (Luria et al., 2010; Vogel and Machizawa, 2004). However, the same behavior has not been found in fMRI studies. Here, the BOLD response is stronger in the contralateral hemisphere compared to the ipsilateral one, but it linearly increases also after reaching the VSTM capacity limit, instead of leveling-off (Robitaille et al., 2010). The same findings have been recently corroborated by an fNIRS investigation (Cutini et al., 2011a).

This dissociation between electrical and hemodynamic results may reflect the ability of the two techniques to reveal distinct neural processes underlying VSTM. However, this dissociation could be also due to inherent technical problems: the temporal resolution of fMRI and EEG is, for example, completely different and also the duration of the neural response. While the SPCN is of the order of milliseconds, the BOLD response is of the order of seconds. The paradigm usually applied in these studies is the change detection task: a memory array is briefly shown and after a few seconds, the test array is displayed. Thus, while with EEG the neural response to the memory array is completely dissociated from the

neural response to the test array, for the inherent long duration of the HR, the neural responses to the memory and test arrays are, in hemodynamic studies, overlapping, making their isolation more difficult.

In this chapter, an exploratory study aiming at further exploring the dissociation between ERP and hemodynamic results is carried out. Participants were simultaneously measured using both EEG and fNIRS techniques, in order to acquire electrical and hemodynamic signals at the same time. fNIRS was preferred to the fMRI technique for its higher temporal resolution, which may allow a more detailed representation of the VSTM processes. In this context, physiological noise removal is an important step, in order to prevent a further camouflaging effect due to physiological noise oscillations, other than the test array HR. A variant of the paradigm used by Cutini et al. (2011a) was performed to try to reduce the activation due to the test array.

7.2 Data

Nine students (4 female) at the University of Padova (mean age 26.7, range 23-30) participated in the experiment after providing informed consent. All participants had normal or corrected to-normal vision. None of them reported a history of neurological or psychiatric disorders or was under medication at the time of testing.

Each participant was seated on a comfortable chair in a dimly lit room in front of a LCD monitor placed at a viewing distance of 60 cm. The paradigm used was a variant of the change-detection task. Each trial began with a central plus sign, which was followed 2 s later by a central fixation point, which remained on the screen for the entire duration of the trial. After 600 ms, at the central fixation point was added an arrow, indicating the left or right side of the screen for 400 ms. Afterwards, a blank interval of 300 ms preceded the presentation of the memory array, which remained on the screen for 300 ms. The memory array was composed of 1 or 3 colored squares (yellow, red, blue, green, white, cyan orange or violet) always of different colors and both on the right and left

side of the central fixation point. After a blank interval of 1400-1600 ms elapsed, the test array was presented until a response was detected (Fig. 7.2.1). The test array was composed of a single colored square located in the center of the screen. An inter-stimulus interval of 10-14 s followed the detection of the response. The paradigm was very similar to the one used in Cutini et al. (2011a), it only differed for the presentation of the single centered colored square for the test array. The innovation bound to the introduction of this single centered square has to be found in the attempt to reduce the hemodynamic response elicited by the test array, which, for the slow nature of the HR, overlaps the HR of interest elicited by the memory array.

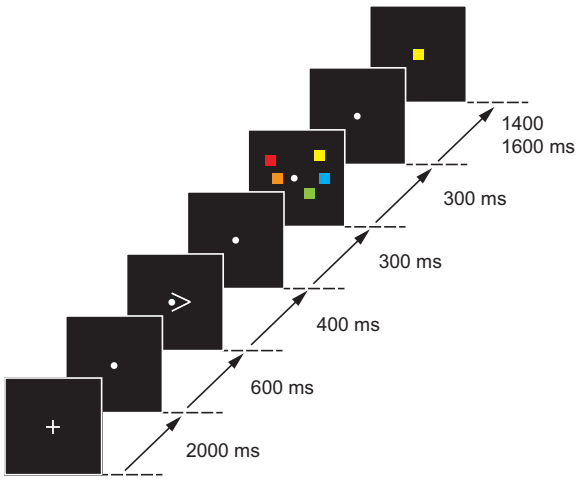

Figure 7.2.1: A schematic representation of the paradigm used.

Participants had to memorize the colors of the squares located on the side indicated by the arrow. After the presentation of the test array, their task was to press one of two previously labeled keys on the keyboard, to indicate whether the color of the square of the test array was present among the colors previously memorized of the memory array or not. Four different memory arrays were possible: 1 colored square to memorize on the left, 1 on the right, 3 on the left and 3 on the right, which can be defined as load and side conditions. Participants were instructed to maintain their gaze at fixation, above all during the presentation of the

memory array. Participants performed 4 blocks of 40 experimental trials and each block contained (randomly presented) the same number of trials for each of the four possible memory array conditions. Moreover, in half of the trials, the color of the square in the test array was the same as one of the squares of the memory array, while in half of the trials it was different.

7.3 Probe Placement and data acquisition

Hemodynamic activity was recorded with a multi-channel frequency-domain NIR spectrometer (ISS ImagentTM, Champaign, Illinois), equipped with 20 laser diodes (690 nm and 830 nm) and four photomultiplier tubes. The electrical data, instead, were recorded with an 8-channels portable EEG system. fNIRS and EEG data were acquired simultaneously.

A probe placement method (Cutini et al., 2011b) based on the correspondence between 10-20 points and the underlying cerebral regions was used to locate optical optodes. A set of sources and detectors was placed in order to sample the occipito-parietal cortices, particularly the IPS and IOS, on a custom-made cap. Five channels per hemisphere were dedicated to this task, and located in order to sample these brain regions (see Cutini et al. (2011a) for a similar probe placement). All these channels had a source-detector distance of 3 cm. The other two detectors, with two nearly located sources, were used to measure the physiological noise oscillations. Therefore, one short-separation channel, with source-detector distance of 0.7 cm, per hemisphere, was available. The optical signal detected by the PMTs was converted into concentration changes of HbO and HbR through the modified Beer-Lambert Law.

Two EEG electrodes were placed to monitor the neural activity of interest, one on the 10/20 position P7 and the other on P8 and were inserted in the custom-made cap created for the fNIRS acquisition. The reference electrode was placed on the left earlobe. Another electrode was placed on the right earlobe. The EEG signal was re-referenced offline to the average

of the left and right earlobes. Three other electrodes were used to monitor the eye-movements: two, located laterally to the left and right external canthi, were assigned for the detection of horizontal eye movements (HEOG), and the other, placed on Fp1, for the vertical ones (VEOG). The electrode impedance was kept less than 5 KΩ.

7.4 Signal processing and data analysis

7.4.1 EEG

EEG, HEOG and VEOG signals were amplified (pass-band 0.1-80Hz) and digitized at a sampling rate of 250 Hz. The baseline for ERP measurements was calculated as the mean voltage of a 200 ms pre-stimulus interval. Trials contaminated by either horizontal or vertical eye movements (exceeding $\pm$60 μV), or other artifacts (exceeding $\pm$80 μV) were excluded from analysis. For each trial, the EEG signal was subdivided in -200/1000 epochs time-locked to the presentation of the memory array. Only correct responses were included in the analysis. All remaining segments were averaged, for each participant, for each of the four conditions (1 left square, 1 right square, 3 left squares and 3 right squares) of the memory array, separately.

The contralateral ERP was computed, separately for the 1 and 3 squares conditions, by averaging the ERPs measured in the hemisphere contralateral to the side of presentation of the memory array (i.e. averaging the activity measured in P7, located in the left hemisphere, when the memory array was displayed on the right side and the activity measured at P8, located in the right hemisphere, when the memory array was displayed on the left side of the screen). Similarly, the ipsilateral ERP was computed averaging the ERPs detected in the hemisphere ipsilateral to the side of presentation of the memory array, for each of the two load conditions. The SPCN is obtained by subtracting the ipsilateral from the contralateral activity. Mean SPCN amplitudes for both load 1 and 3 were measured in a time window of 400-900 ms and submitted to paired-sample t-test.

7.4.2 fNIRS

Individual hemodynamic time-series were zero-mean corrected and band-pass filtered (0.01-3 Hz) in order to remove very slow drifts and high frequency noise. Starting from the onset of the memory array, the time-series were divided into segments of 14 s each. The same trials rejected in the EEG procedure, due to eye-movements, blinks or wrong responses, were removed from the analysis. ReMCoBA, the algorithm proposed in chapter 3, was applied to minimize the impact of physiological noise oscillations and residual random noise on the optical signal and to recover the mean HRs for every channel, participant and condition of the memory array.

Similarly to the ERP procedure, contralateral and ipsilateral hemodynamic responses were computed. For every pair of channels located symmetrically in the two hemispheres, the contralateral HR was computed averaging the HRs measured in channels located in the left hemisphere, when the to be memorized colored squares were displayed on the right side of the screen and the HRs measured in channels located in the right hemisphere, when the colored squares to be memorized were visualized on the left side of the screen. The ipsilateral HR, for every pair of symmetric channels, was computed similarly, averaging the activity measured in channels located ipsilaterally to the side of presentation of the to be memorized colored squares. This procedure was repeated both for the load 1 and load 3 conditions. Therefore, for every channels' pair and participant, four hemodynamic responses were obtained: 1 contralateral square, 1 ipsilateral square, 3 contralateral squares, 3 ipsilateral squares.

For every obtained HR, the mean of the curve between the peak and $\pm$ 2 seconds (mean_peak) was computed and submitted to a repeated measures ANOVA, with load (1 vs. 3), side (contralateral vs. ipsilateral) and channels' pair (1-5) as within-subject factors.

7.5 RESULTS

The mean SPCNs obtained in the load 1 and load 3 conditions are displayed in Fig. 7.5.1. This figure shows how, consistently with literature, the SPCN is more negative when the load increases, going from 1 to 3 squares. The paired-sample t-test revealed significant differences between the two load conditions (t=4.4, p =.002).

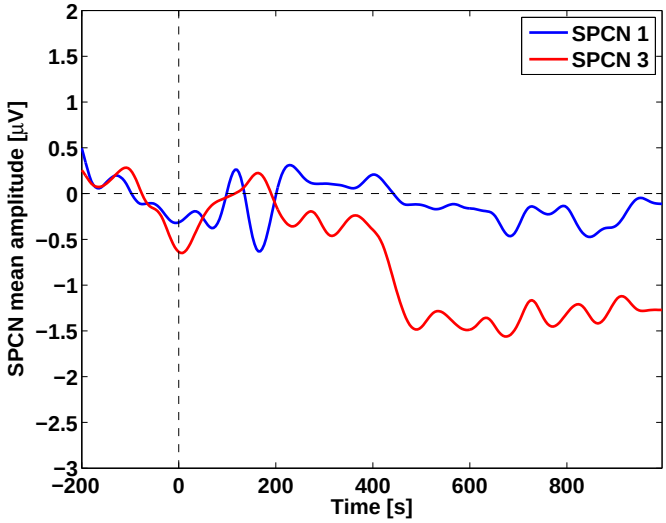

Figure 7.5.1: Mean SPCNs for the load 1 (blue) and load 3 (red) conditions. Note the stronger negativity of the SPCN in the case of load 3 compared to load 1.

The analysis on the mean_peak parameter of the HRs revealed a significant effect only of the side factor ($F(1,8) = 6.5$, $p = 0.034$). However, looking at the mean HRs in the channel located on the IPS/IOS (and roughly near the channel where Cutini et al. (2011a) found both a lateralization and load effects), the effect of the load is apparent. The HR is stronger for the 3 squares condition, in both side conditions, compared to the 1 square condition. It is also evident the stronger activation in the contralateral condition compared to the ipsilateral one (Fig. 7.5.2). The lack of statistical significance for the load condition may be due to the restricted set of available participants. The lack of significance for the interaction load x side, instead, is evident in the figure: the contralateral and ipsilateral

HRs, going from load 1 to load 3, show about the same increase, pointing out the additive nature of this load effect in both side conditions.

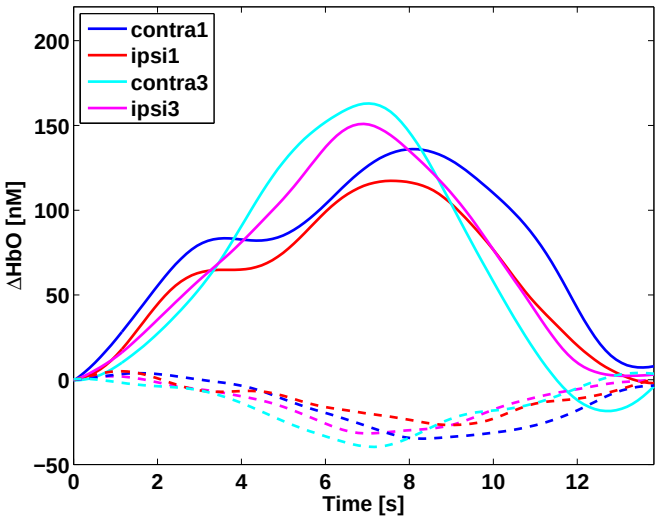

Figure 7.5.2: Mean HRs for contralateral load 1 (blue), contralateral load 3 (cyan), ipsilateral load 1 (red) and ipsilateral load 3 (magenta) conditions in one couple of symmetric channels located on IPS/IOS. Solid line for HbO and dashed line for HbR. Note the higher activity in the load 3 conditions compared to the load 1 conditions and the higher activity in the contralateral conditions compared to the ipsilateral ones. Note also that both in the contralateral and the ipsilateral conditions the increase in activity between load 1 and load 3 is very similar.

7.6 Discussion

The aim of the present study was to further investigate the dissociation between the electrical neural results and the hemodynamic findings in a VSTM paradigm. Electrical neural activity elicits a SPCN response, which is more negative increasing the number of items to be retained in VSTM, but which reaches a plateau when the VSTM capacity limit is met. On the contrary, from previous studies, the hemodynamic activity in the same task has revealed a different behavior, with an increase in activity proportional to the number of items to be memorized, which continues even after the VSTM capacity limit has been reached.

Here, electrical results measured with EEG confirm the expected behavior, with an increase in the negativity of the SPCN from load 1 to load 3. Even if, in this experiment, the number of items to be memorized were below VSTM capacity limit, the interaction between side and load is evident in Fig. 7.5.1.

Hemodynamic results confirmed previous fMRI and fNIRS studies (Cutini et al., 2011a; Robitaille et al., 2010), with an increase in hemodynamic activity from load 1 to 3, in the contralateral compared to the ipsilateral condition and a lack of interaction between side and load factors. Indeed, the increase in activity found for the load condition is the same both in the contralateral and ipsilateral conditions, as it is evident in Fig. 7.5.2. The lack of significance for the load condition, instead, may be due to the restricted number of participants available, since the trend of increasing in hemodynamic activity from load 1 to load 3 is apparent in all channels. Therefore, the expedient of using the single centered colored square for the test array seems still not enough to prevent the HR elicited by the test array from camouflaging the HR of interest elicited by the memory array.

In conclusion, more studies are required to further investigate the dissociation between hemodynamic and electrical results in VSTM paradigm. This possible dissociation may be due to possible different neural processes underlying the hemodynamic and electrical activity involved in VSTM. However, further studies on a paradigm able to prevent the test array to elicit strong HRs and on signal processing methods, with the ability to isolate the memory and test array responses, may reveal that this dissociation was only due to technical issues.

8

Neonatal resting state: Application of the optical head models

fNIRS and DOT are ideal techniques for monitoring cerebral hemodynamics in newborns at the cot-side in the neonatal intensive care unit (Ancora et al., 2013; Lin et al., 2013). Resting state acquisitions can be performed to monitor newborns suffering from many different pathologies (Cooper et al., 2011), including hypoxic-ischemic encephalopathy, which is usually caused by a lack of oxygen supply during birth, and can result in complex brain injury and seizures. Monitoring hemodynamics in such babies can potentially inform the treatment of transient hemodynamic events and seizures, and may also be useful to predict future cognitive or motor impairments. In order to facilitate the interpretability of DOT results by physicians, reconstructing accurate, aged-matched, anatomically registered images of hemodynamic parameters is essential.

One of the problems with resting state acquisitions in infants is the

presence of many motion artifacts. If they are not identified and removed, they can provide false activations. This is particularly important, for example, during resting state acquisitions in newborns suffering from seizures. Motion artifacts due to the seizures may camouflage the actual cerebral hemodynamic changes and provide false activations.

In this chapter, a data set measured in a healthy term-age baby with many motion artifacts is used to prove the importance of correcting for motion artifacts (see chapter 4) before image reconstruction. The age-matched optical head model proposed in chapter 5 is applied to reconstruct images of concentration changes using an anatomy similar to that of the monitored baby.

8.1 Probe placement and DOT data acquisition

Resting state data were acquired from a healthy full term baby (40 weeks PMA) at the Evelyn perinatal imaging center, in Cambridge, U.K. and were provided courtesy of University College London, U.K.. During the acquisition both optical and EEG data were acquired: here I will focus only on the optical measurements.

Hemodynamic activity was recorded with a custom-built continuous-wave NIRS system (NTS5, Biomedical Optics Research Laboratory, University College London), equipped with 16 pairs of laser diodes (at 770 and 850 nm) and 16 detectors, arranged in a purpose built infant head cap which provides a total of 58 channels. Source-detector distances varied between ~2 and 4.5 cm. Data were acquired with a sampling frequency of ~10 Hz.

Probe placement was performed according to the 10-5 international system (see Fig. 8.1.1). The position of the optodes was designed to cover as much of the baby's cortex as possible, including frontal, temporal, parietal and occipital regions (Fig. 8.1.2), while also providing a reasonable channel density. The optical fibers were placed on the infant's

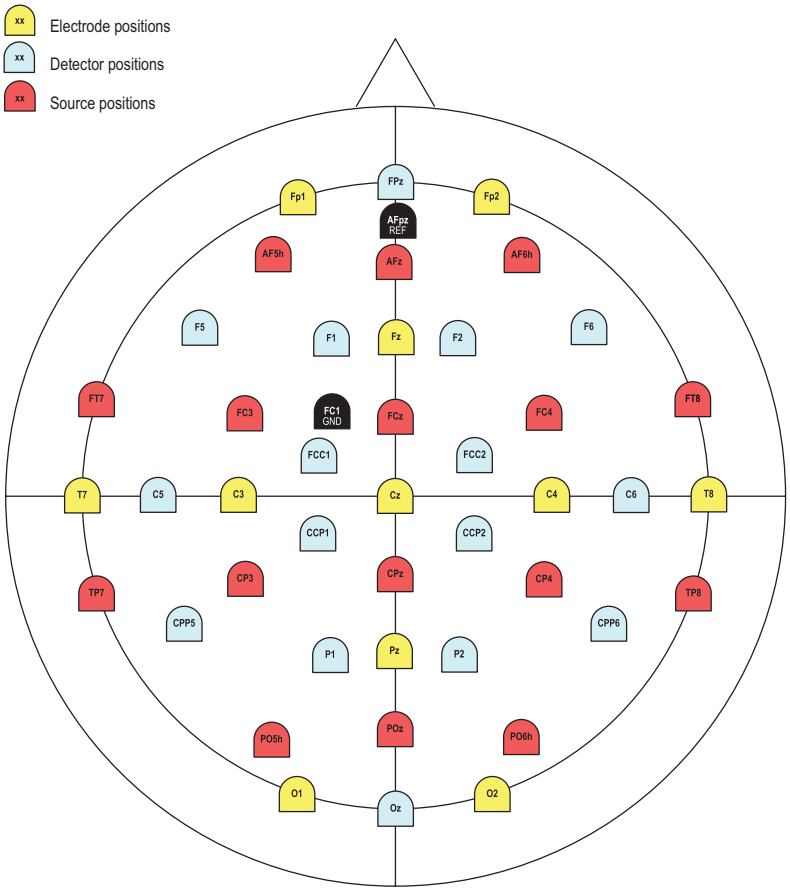

Figure 8.1.1: Probe placement: in light blue are indicated the detectors' positions, in red the sources' positions and in yellow and black the positions for the electrodes. Every optode and electrode is placed on a 10-5 position.

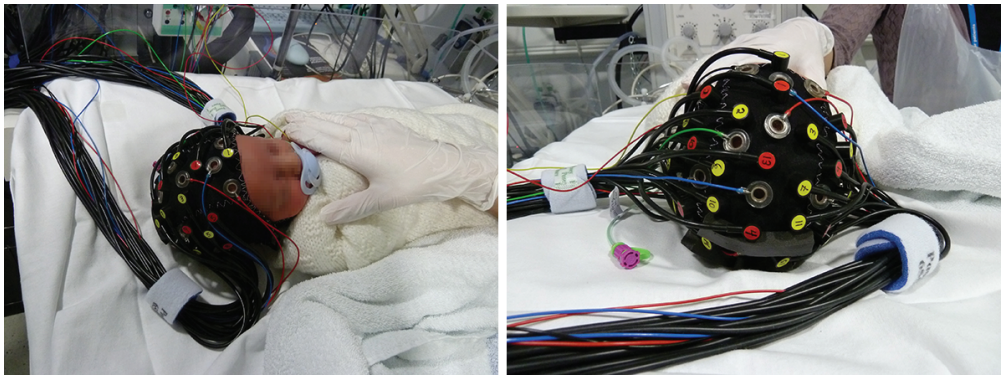

Figure 8.1.2: The EEG-DOT cap placed on a newborn in the cot. The colored fibers are the electrode fibers while the black fibers are the optical fibers. Yellow and red denote sources and detectors position.

head using a soft, skin-compatible cap (EasyCap, Germany), which is easy and fast to place on the infant's head.

8.2 Signal processing and image recontruction

8.2.1 Signal processing

In order to show the importance of motion artifact correction, two processing streams were performed, one in which motion artifacts were identified and corrected, and the other in which they were not corrected. Both processing streams were performed using a number of the Homer2 NIRS processing package functions (Huppert et al., 2009).

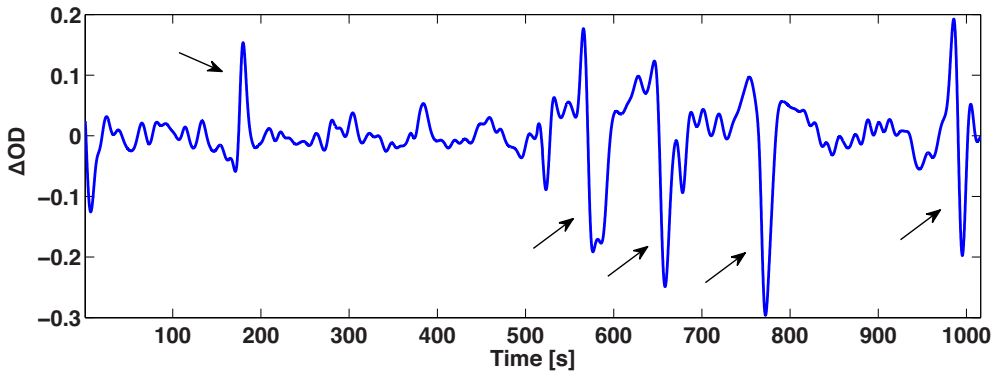

Figure 8.2.1: Example of time series from one of the measured channel. Note how motion artifacts can be easily identified, due to their higher amplitude compared to the measured normal signal.

In both processing streams raw intensity data were converted into optical density data. For the motion correction processing stream, motion artifacts were then identified using the function hmrMotionArtifactByChannel applied to the OD time series, with parameters $AMPThresh = 0.2$, $STDThresh = 50$, $tMotion = 0.5$, and $tMask = 1$. Spline interpolation was then applied to the motion artifacts identified, with parameter $p = 0.99$ (Scholkmann et al., 2010). The spline technique was chosen for two reasons: motion artifacts are easily identified in these data series (Fig.

8.2.1) and spline interpolation does not modify the remaining parts of the signal, allowing the effects of motion artifact correction to image reconstruction to be isolated. Both the motion-corrected OD time series and the OD time series without motion correction were then band-passed filtered (0.009-0.08 Hz), to isolate the low frequency oscillations, which are usually of importance in functional connectivity studies.

8.2.2 IMAGE RECONSTRUCTION

The 40 weeks PMA optical head model proposed in chapter 5 was used to perform image reconstruction. Since the baby's cranial landmarks were not available, it was not possible to register the head model to the baby's head. Therefore, the 40 weeks PMA head model was directly used without any registration process.

Sources and detectors were placed on the head model volumetric mesh, according to Fig. 8.1.1, on the corresponding 10-5 coordinates provided with the head model. A mesh-based Monte Carlo simulation was then performed, with the MMC package (Fang, 2010) for every source and detector of the probe. The output of the Monte Carlo simulation gives, for every node of the mesh, the number of photons which pass through that node. The sensitivity matrix (number of nodes x number of channels) was computed by combining the photon fluences (the outputs of the MC simulation) measured at the source and the detector position which make up a channel.

Since image reconstruction requires the inversion of the Jacobian, to make this process computationally feasible it is important to reduce the dimensionality of the matrix as far as possible. Hence, instead of performing image reconstruction in the volumetric mesh, the lower density GM surface mesh was used. The Jacobian computed on the volumetric mesh was projected onto the GM surface mesh, obtaining a surface Jacobian J_{surf} (number of nodes of the GM surface mesh x number of channels) (Fig. 8.2.2). The concentration changes of HbO and HbR were then reconstructed on the GM surface mesh inverting J_{surf} and multiplying it

by the filtered OD data (number of time points x number of channels) for every time sample.

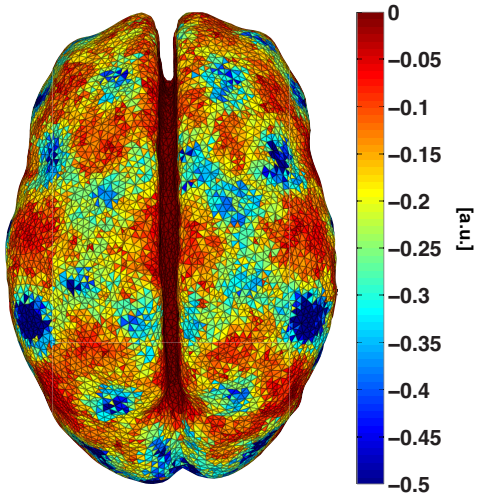

Figure 8.2.2: GM surface mesh sensitivity matrix obtained using the probe placement of Fig. 8.1.1. In red the areas of low sensitivity, in blue of higher sensitivity. The probe placement used allows whole-head coverage, even if, due to the limited number of sources and detectors, some areas of the cortex present lower sensitivity.

Therefore, for every time point, two HbO and HbR image reconstructions were performed, one using the filtered OD data with motion artifact correction and the other using the filtered OD data without motion artifact correction.

8.3 Results

In Fig. 8.3.1 an example of both motion corrected (magenta) and non-motion corrected (blue) OD time-series measured at one of the central channels of the array is displayed. Spline interpolation was successfully able to reduce the motion artifacts and maintain the remaining portion of the signal unchanged. The time window 750-900 seconds was chosen for the image reconstruction process, since it contains a big motion artifact, present in the majority of the channels. A selection of the reconstructed images of HbO concentration changes is displayed in the second

and third row of the figure. In the second row, images were reconstructed using the non-motion corrected OD time series, while in the third row images were reconstructed with the motion corrected OD time series. Images at the same time points are visualized in the two rows of Fig. 8.3.1.

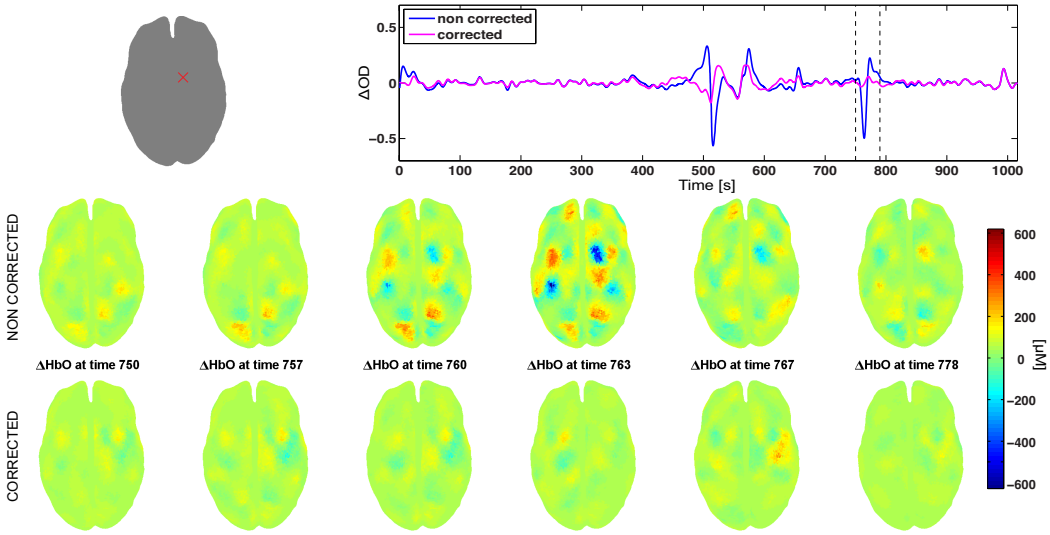

Figure 8.3.1: In the first row of the figure, example of both motion corrected (magenta) and non-motion corrected (blue) OD time-series measured at one of the central channels of the array, whose location is indicated by the red cross on the upper left grey GM surface mesh. The vertical dashed lines indicate the time window chosen for the image reconstruction process. In the second and third row, ΔHbO reconstructed images at selected time points on the 40 weeks PMA GM surface mesh. In the second row, non-motion corrected OD time series are used in the reconstruction process, while in the third row motion-corrected OD time series are used. Red areas indicate an increase in HbO concentration while blue areas a decrease.

Before the motion artifact starts, both motion corrected and non-motion corrected images show homogenous hemoglobin concentration. When the artifact starts, around 760 seconds, the motion corrected images show the same homogeneous pattern of activity, while the non-motion corrected images display an increase or decrease of ΔHbO in several areas of the cortex, correspondent to the channels where the artifact was present. When the artifact ends, the non-motion corrected images again show a homogeneous pattern of hemoglobin concentration.

In Fig. 8.3.2 the reconstructed images using the motion corrected time series displayed in Fig. 8.3.1 are displayed, but with a different color-bar scale. While in Fig. 8.3.1 the color was set to be equal to the color bar of the non-motion corrected images, in Fig. 8.3.2 the color bar is set to take into account the maximum and minimum values of the motion-corrected time-series. Changes in ΔHbO occurring slowly during the acquisition are apparent, which were hidden by the strong motion artifact in the uncorrected data of Fig 8.3.1.

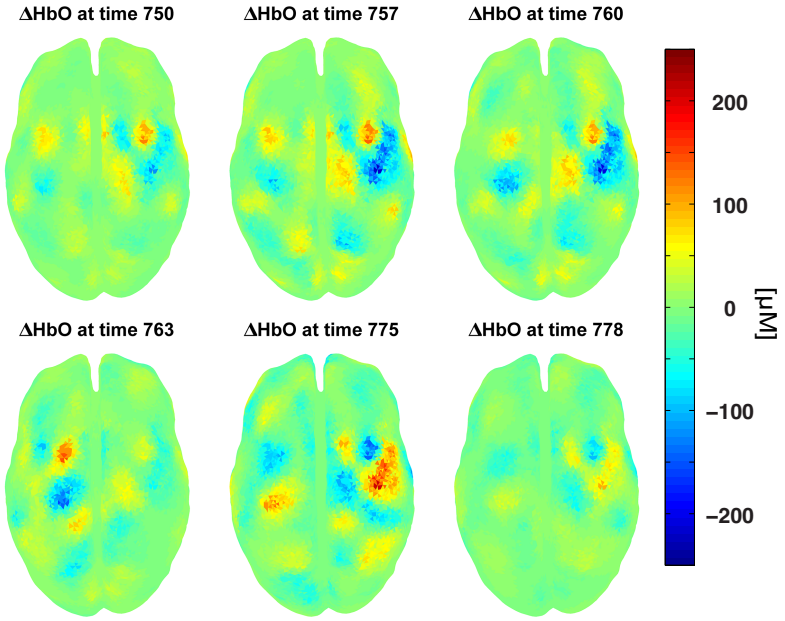

Figure 8.3.2: ΔHbO images reconstructed using the motion corrected time series. The same reconstructed time points displayed in Fig. 8.3.1 are visualized. The different color bar scale, computed using the maximum and minimum values detected in the motion corrected time series, reveals the presence of an ongoing low-frequency brain activity, previously hidden by the strong presence of the artifact.

8.4 Discussion

Motion artifacts are very common in fNIRS and DOT acquisitions in infants. Their presence can camouflage low intensity, ongoing brain ac-

tivity and can be mis-interpreted as real brain activity. It is essential to remove motion artifacts before reconstructing images of hemoglobin concentration changes. However, care should be taken when correcting for motion artifacts in resting state data. Further studies are required to investigate whether motion correction techniques may bias the correlation between signals or their impact on the signals is minimal.

The optical head model presented in chapter 6 was successfully applied to reconstruct images of HbO concentration changes in the infant brain. Both the volumetric mesh and the GM surface mesh were required to perform the Monte Carlo simulations and the reconstruction itself. The 10-5 positions were also used, since the optodes were placed according to this convention. Reconstructing HbO concentration changes using anatomy as close as possible to that of the patient is essential in order to correctly locate the areas of the cortex involved in any hemodynamic change. The age-matched head model described in chapter 6 represents the most accurate approach to infant DOT reconstruction when the patient's MRI is not available. Registering the age-matched head model to the patient's head, which was not performed here due to the non-availability of the baby's cranial landmarks, will further increase the accuracy of the results.

In conclusion, the optical head models proposed in chapter 6 have been shown to be easily applicable in the image reconstruction process. Moreover, care should be taken when reconstructing images: the presence of motion artifacts may lead to biased or incorrect interpretation of the hemodynamic results.

9 Conclusions

FNIRS and DOT are novel non-invasive optical techniques with great potentials in clinical and cognitive investigations. Their fields of application range from healthy adults to newborns to pathological populations, whose cerebral activity can hardly be monitored using different techniques, such as fMRI or EEG. Given however their recent introduction in the neuroscientific field of investigations, the algorithms for optical data treatment still await further and important improvements, some of which have been proposed and described in the present thesis.

As argued in foregoing chapters of this thesis, the issue subtended in the separation of optical signal from physiological noise is pivotal in the fNIRS processing pipeline. In this thesis, a novel method for physiological noise reduction, ReMCoBA, has been presented and validated. The proposed method has also been successfully applied for filtering data acquired during two different cognitive experiments. In the first experiment, we were able to recover subtle temporal differences between hemo-

dynamic responses measured in M1 and SMA during short- vs. long- duration finger tapping. These results dovetailed nicely with previous fMRI investigations on the interplay between M1 and SMA during motor tasks. In the second experiment, a variant of the standard change-detection task and ReMCoBA were applied to try to minimize the impact of physiological noise and the activity elicited by the test array, in a VSTM paradigm. The recovered trends confirmed and extended previous results obtained with both fMRI and fNIRS.

Motion artifacts are also a significant problem in the fNIRS and DOT measured signal and their removal is essential for a correct estimate of the true hemodynamic activity. In this thesis, a general objective approach for the selection of the best motion correction technique for a generic data set has been proposed and validated using a data set full of low frequency motion artifacts, particularly challenging to be detected and removed. The proposed approach is available to users who want to select on a parametric basis the appropriate motion correction technique for the data set under examination.

Age-matched neonatal optical head models are an essential tool for DOT acquisitions and image reconstruction in the field of developmental neuroscience. Due to the rapid growth of the infant's brain, using the correct age-matched anatomy in the image reconstruction process is essential for a correct localization of the neural source of hemodynamic fluctuations. In this thesis, a novel 4D neonatal optical head model has been presented. For each week, from 29 weeks PMA to 44 weeks PMA, this head model provides users with all the tools necessary for image reconstruction following the principle of minimum deviance from the real anatomy. An example of the application of the optical head model for a selected age has also been proposed, using resting state data acquired on a healthy full term baby. In this context, the head model has been easily and successfully applied to obtain images of HbO concentration changes.

References

Abdelnour, A. F. and Huppert, T. Real-time imaging of human brain function by near-infrared spectroscopy using an adaptive general linear model. *NeuroImage*, 46(1):133–43, 2009.

Altaye, M., Holland, S. K., Wilke, M., and Gaser, C. Infant brain probability templates for MRI segmentation and normalization. *NeuroImage*, 43(4):721–30, 2008.

Ancora, G., Maranella, E., Grandi, S., Sbravati, F., Coccolini, E., Savini, S., and Faldella, G. Early predictors of short term neurodevelopmental outcome in asphyxiated cooled infants. A combined brain amplitude integrated electroencephalography and near infrared spectroscopy study. *Brain & development*, 35(1):26–31, 2013.

Arridge, S. R. Optical tomography in medical imaging. *Inverse Problems*, 15(2):R41–R93, 1999.

Arridge, S. R. and Schweiger, M. Image reconstruction in optical tomography. *Philosophical transactions of the Royal Society of London. Series B, Biological sciences*, 352(1354):717–26, 1997.

Arridge, S. R., Schweiger, M., Hiraoka, M., and Delpy, D. T. A finite element approach for modeling photon transport in tissue. *Medical physics*, 20(2 Pt 1):299–309, 1993.

Arridge, S. R., Dehghani, H., Schweiger, M., and Okada, E. The finite element model for the propagation of light in scattering media: a direct method for domains with nonscattering regions. *Medical physics*, 27(1): 252–64, 2000.

Arridge, S. R. Methods in diffuse optical imaging. *Philosophical transactions. Series A, Mathematical, physical, and engineering sciences*, 369(1955): 4558–76, 2011.

Bade, R., Haase, J., and Preim, B. Comparison of fundamental mesh smoothing algorithms for medical surface models. In *SimVis*, volume 6, pages 289–304. Citeseer, 2006.

Bal, G. Transport through diffusive and nondiffusive regions, embedded objects, and clear layers. *SIAM Journal on Applied Mathematics*, 62(5): 1677–1697, 2002.

Bamett, A. H., Culver, J. P., Sorensen, A. G., Dale, A., and Boas, D. A. Robust inference of baseline optical properties of the human head with three-dimensional segmentation from magnetic resonance imaging. *Applied optics*, 42(16):3095–108, 2003.

Bandettini, P. A., Wong, E. C., Hinks, R. S., Tikofsky, R. S., and Hyde, J. S. Time course EPI of human brain function during task activation. *Magnetic resonance in medicine : official journal of the Society of Magnetic Resonance in Medicine / Society of Magnetic Resonance in Medicine*, 25(2): 390–7, 1992.

Battin, M. and Rutherford, M. Magnetic resonance imaging of the brain in preterm infants: 24 weeks gestation to term. In Rutherford, M., editor, *MRI of the neonatal brain*, chapter 3. W.B. Saunders, 2002.

Bauernfeind, G., Scherer, R., Pfurtscheller, G., and Neuper, C. Single-trial classification of antagonistic oxyhemoglobin responses during mental arithmetic. *Medical & biological engineering & computing*, 49(9):979–84, 2011.

Birbaumer, N. and Cohen, L. G. Brain-computer interfaces: communication and restoration of movement in paralysis. *The Journal of physiology*, 579(Pt 3):621–36, 2007.

Birn, R. M., Saad, Z. S., and Bandettini, P. A. Spatial heterogeneity of the nonlinear dynamics in the FMRI BOLD response. *NeuroImage*, 14(4): 817–26, 2001.

Boas, D. A., Gaudette, T., Strangman, G., Cheng, X., Marota, J. J., and Mandeville, J. B. The accuracy of near infrared spectroscopy and imaging during focal changes in cerebral hemodynamics. *NeuroImage*, 13(1): 76–90, 2001.

Boas, D. A., Franceschini, M. A., Dunn, A., and Strangman, G. Noninvasive Imaging of Cerebral Activation with Diffuse Optical Tomography.

In Frostig, R., editor, *In Vivo Optical Imaging of Brain Function*, chapter 14. CRC Press, Boca Raton (FL), 2nd edition, 2009.

Boas, D. A. and Dale, A. M. Simulation study of magnetic resonance imaging-guided cortically constrained diffuse optical tomography of human brain function. *Applied optics*, 44(10):1957–68, 2005.

Boas, D. A., Culver, J., Stott, J., and Dunn, A. Three dimensional Monte Carlo code for photon migration through complex heterogeneous media including the adult human head. *Optics express*, 10(3):159–70, 2002.

Boas, D. A., Dale, A. M., and Franceschini, M. A. Diffuse optical imaging of brain activation: approaches to optimizing image sensitivity, resolution, and accuracy. *NeuroImage*, 23 Suppl 1:S275–88, 2004.

Boas, D. A., Elwell, C. E., Ferrari, M., and Taga, G. Twenty years of functional near-infrared spectroscopy: introduction for the special issue. *NeuroImage*, 85 Pt 1:1–5, 2014.

Brigadoi, S., Cutini, S., Scarpa, F., Scatturin, P., and Dell'Acqua, R. Exploring the role of primary and supplementary motor areas in simple motor tasks with fNIRS. *Cognitive processing*, 13 Suppl 1:S97–101, 2012.

Brigadoi, S., Ceccherini, L., Cutini, S., Scarpa, F., Scatturin, P., Selb, J., Gagnon, L., Boas, D. A., and Cooper, R. J. Motion artifacts in functional near-infrared spectroscopy: A comparison of motion correction techniques applied to real cognitive data. *NeuroImage*, 85 Pt 1:181–91, 2014.

Brown, M. A. and Semelka, R. C. *MRI Basic Principle and Applications*. Wiley-Blackwell, 4th edition, 2010.

Buss, A. T., Fox, N., Boas, D. A., and Spencer, J. P. Probing the early development of visual working memory capacity with functional near-infrared spectroscopy. *NeuroImage*, 85 Pt 1:314–25, 2014.

Buxton, R. B. *Introduction Functional Magnetic Resonance Imaging Principles And Techniques*. Cambridge University Press, 2002.

Calderon-Arnulphi, M., Alaraj, A., and Slavin, K. V. Near infrared technology in neuroscience: past, present and future. *Neurological research*, 31(6):605–14, 2009.

Chance, B., Zhuang, Z., UnAh, C., Alter, C., and Lipton, L. Cognition-activated low-frequency modulation of light absorption in human brain. *Proceedings of the National Academy of Sciences of the United States of America*, 90(8):3770–4, 1993.

Chau, W. and McIntosh, A. R. The Talairach coordinate of a point in the MNI space: how to interpret it. *NeuroImage*, 25(2):408–16, 2005.

Ciftçi, K., Sankur, B., Kahya, Y. P., and Akin, A. Constraining the general linear model for sensible hemodynamic response function waveforms. *Medical & biological engineering & computing*, 46(8):779–87, 2008.

Cohen-Adad, J., Chapuisat, S., Doyon, J., Rossignol, S., Lina, J.-M., Benali, H., and Lesage, F. Activation detection in diffuse optical imaging by means of the general linear model. *Medical image analysis*, 11(6):616–29, 2007.

Collins, D. L., Zijdenbos, A. P., Kollokian, V., Sled, J. G., Kabani, N. J., Holmes, C. J., and Evans, A. C. Design and construction of a realistic digital brain phantom. *IEEE transactions on medical imaging*, 17(3):463–8, 1998.

Cooper, R. J., Hebden, J. C., O'Reilly, H., Mitra, S., Michell, A. W., Everdell, N. L., Gibson, A. P., and Austin, T. Transient haemodynamic events in neurologically compromised infants: a simultaneous EEG and diffuse optical imaging study. *NeuroImage*, 55(4):1610–6, 2011.

Cooper, R. J., Gagnon, L., Goldenholz, D. M., Boas, D. A., and Greve, D. N. The utility of near-infrared spectroscopy in the regression of low-frequency physiological noise from functional magnetic resonance imaging data. *NeuroImage*, 59(4):3128–38, 2012a.

Cooper, R. J., Caffini, M., Dubb, J., Fang, Q., Custo, A., Tsuzuki, D., Fischl, B., Wells, W., Dan, I., and Boas, D. A. Validating atlas-guided DOT: a comparison of diffuse optical tomography informed by atlas and subject-specific anatomies. *NeuroImage*, 62(3):1999–2006, 2012b.

Cooper, R. J., Selb, J., Gagnon, L., Phillip, D., Schytz, H. W., Iversen, H. K., Ashina, M., and Boas, D. A. A systematic comparison of motion artifact correction techniques for functional near-infrared spectroscopy. *Frontiers in neuroscience*, 6:147, 2012c.

Cope, M. and Delpy, D. T. System for long-term measurement of cerebral blood and tissue oxygenation on newborn infants by near infrared transillumination. *Medical & biological engineering & computing*, 26 (3):289–94, 1988.

Costeloe, K., Hennessy, E., Haider, S., Stacey, F., Marlow, N., and Draper, E. Short term outcomes after extreme preterm birth in England: comparison of two birth cohorts in 1995 and 2006 (the EPICure studies). *BMJ (Clinical research ed.)*, 345:e7976, 2012.

Cowan, N. The magical number 4 in short-term memory: a reconsideration of mental storage capacity. *The Behavioral and brain sciences*, 24(1): 87–114; discussion 114–85, 2001.

Cristia, A., Dupoux, E., Hakuno, Y., Lloyd-Fox, S., Schuetze, M., Kivits, J., Bergvelt, T., van Gelder, M., Filippin, L., Charron, S., and Minagawa-Kawai, Y. An online database of infant functional near infrared spectroscopy studies: a community-augmented systematic review. *PloS one*, 8(3):e58906, 2013.

Cui, X., Bray, S., and Reiss, A. L. Functional near infrared spectroscopy (NIRS) signal improvement based on negative correlation between oxygenated and deoxygenated hemoglobin dynamics. *NeuroImage*, 49 (4):3039–46, 2010.

Custo, A., Boas, D. A., Tsuzuki, D., Dan, I., Mesquita, R., Fischl, B., Grimson, W. E. L., and Wells, W. Anatomical atlas-guided diffuse optical tomography of brain activation. *NeuroImage*, 49(1):561–7, 2010.

Cutini, S., Scatturin, P., Menon, E., Bisiacchi, P. S., Gamberini, L., Zorzi, M., and Dell'Acqua, R. Selective activation of the superior frontal gyrus in task-switching: an event-related fNIRS study. *NeuroImage*, 42(2):945–55, 2008.

Cutini, S., Scarpa, F., Scatturin, P., Jolicœur, P., Pluchino, P., Zorzi, M., and Dell'Acqua, R. A hemodynamic correlate of lateralized visual short-term memories. *Neuropsychologia*, 49(6):1611–21, 2011a.

Cutini, S., Scatturin, P., and Zorzi, M. A new method based on ICBM152 head surface for probe placement in multichannel fNIRS. *NeuroImage*, 54(2):919–27, 2011b.

Cutini, S., Moro, S., and Bisconti, S. Review: Functional near infrared optical imaging in cognitive neuroscience: an introductory review. *Journal of Near Infrared Spectroscopy*, 20:75, 2012a.

Cutini, S., Scarpa, F., Scatturin, P., Dell'acqua, R., and Zorzi, M. Number-Space Interactions in the Human Parietal Cortex: Enlightening the SNARC Effect with Functional Near-Infrared Spectroscopy. *Cerebral cortex*, 2012b.

Cutini, S., Scatturin, P., Basso Moro, S., and Zorzi, M. Are the neural correlates of subitizing and estimation dissociable? An fNIRS investigation. *NeuroImage*, 85 Pt 1:391–9, 2014.

Dehaes, M., Gagnon, L., Lesage, F., Pélégrini-Issac, M., Vignaud, A., Valabrègue, R., Grebe, R., Wallois, F., and Benali, H. Quantitative investigation of the effect of the extra-cerebral vasculature in diffuse optical imaging: a simulation study. *Biomedical optics express*, 2(3):680–95, 2011.

Dehaes, M., Kazemi, K., Pélégrini-Issac, M., Grebe, R., Benali, H., and Wallois, F. Quantitative effect of the neonatal fontanel on synthetic near infrared spectroscopy measurements. *Human brain mapping*, 34 (4):878–89, 2013.

Delpy, D. T., Cope, M., van der Zee, P., Arridge, S., Wray, S., and Wyatt, J. Estimation of optical pathlength through tissue from direct time of flight measurement. *Physics in medicine and biology*, 33(12):1433–42, 1988.

Ding, X. P., Fu, G., and Lee, K. Neural correlates of own- and other-race face recognition in children: A functional near-infrared spectroscopy study. *NeuroImage*, 85 Pt 1:335–44, 2014.

Eggebrecht, A. T., White, B. R., Ferradal, S. L., Chen, C., Zhan, Y., Snyder, A. Z., Dehghani, H., and Culver, J. P. A quantitative spatial comparison of high-density diffuse optical tomography and fMRI cortical mapping. *NeuroImage*, 61(4):1120–8, 2012.

Elisee, J., Bonnet, M., and Arridge, S. Accelerated boundary element method for diffuse optical imaging. *Optics letters*, 36(20):4101–3, 2011.

Elwell, C. E., Springett, R., Hillman, E., and Delpy, D. T. Oscillations in cerebral haemodynamics. Implications for functional activation studies. *Advances in experimental medicine and biology*, 471:57–65, 1999.

Erdoan, S. B., Yücel, M. A., and Akn, A. Analysis of task-evoked systemic interference in fNIRS measurements: Insights from fMRI. *NeuroImage*, 2013.

Fang, Q. and Kaeli, D. R. Accelerating mesh-based Monte Carlo method on modern CPU architectures. *Biomedical optics express*, 3(12):3223–30, 2012.

Fang, Q. Mesh-based Monte Carlo method using fast ray-tracing in Plücker coordinates. *Biomedical optics express*, 1(1):165–75, 2010.

Fang, Q. and Boas, D. A. Monte Carlo simulation of photon migration in 3D turbid media accelerated by graphics processing units. *Optics express*, 17(22):20178–90, 2009a.

Fang, Q. and Boas, D. A. Tetrahedral mesh generation from volumetric binary and grayscale images. In *Biomedical Imaging: From Nano to Macro, 2009. ISBI'09. IEEE International Symposium on*, pages 1142–1145. IEEE, 2009b.

Ferradal, S. L., Eggebrecht, A. T., Hassanpour, M., Snyder, A. Z., and Culver, J. P. Atlas-based head modeling and spatial normalization for high-density diffuse optical tomography: In vivo validation against fMRI. *NeuroImage*, 85 Pt 1:117–26, 2014.

Ferrari, M. and Quaresima, V. A brief review on the history of human functional near-infrared spectroscopy (fNIRS) development and fields of application. *NeuroImage*, 63(2):921–35, 2012.

Field, D. A. Qualitative measures for initial meshes. *International Journal for Numerical Methods in Engineering*, 47(4):887–906, 2000.

Fonov, V., Evans, A. C., Botteron, K., Almli, C. R., McKinstry, R. C., and Collins, D. L. Unbiased average age-appropriate atlases for pediatric studies. *NeuroImage*, 54(1):313–27, 2011.

Fournier, M., Mahmoudzadeh, M., Kazemi, K., Kongolo, G., Dehaene-Lambertz, G., Grebe, R., and Wallois, F. Realistic head model design and 3D brain imaging of NIRS signals using audio stimuli on preterm neonates for intra-ventricular hemorrhage diagnosis. *Medical image computing and computer-assisted intervention : MICCAI ... International Conference on Medical Image Computing and Computer-Assisted Intervention*, 15(Pt 3):172–9, 2012.

Franceschini, M. A., Fantini, S., Thompson, J. H., Culver, J. P., and Boas, D. A. Hemodynamic evoked response of the sensorimotor cortex measured noninvasively with near-infrared optical imaging. *Psychophysiology*, 40(4):548–60, 2003.

Franceschini, M. A., Joseph, D. K., Huppert, T. J., Diamond, S. G., and Boas, D. A. Diffuse optical imaging of the whole head. *Journal of biomedical optics*, 11(5):054007, 2006.

Frederick, B. D., Nickerson, L. D., and Tong, Y. Physiological denoising of BOLD fMRI data using Regressor Interpolation at Progressive Time Delays (RIPTiDe) processing of concurrent fMRI and near-infrared spectroscopy (NIRS). *NeuroImage*, 60(3):1913–23, 2012.

Fukui, Y., Ajichi, Y., and Okada, E. Monte Carlo prediction of near-infrared light propagation in realistic adult and neonatal head models. *Applied optics*, 42(16):2881–7, 2003.

Funabiki, Y., Murai, T., and Toichi, M. Cortical activation during attention to sound in autism spectrum disorders. *Research in developmental disabilities*, 33(2):518–24, 2012.

Gagnon, L., Perdue, K., Greve, D. N., Goldenholz, D., Kaskhedikar, G., and Boas, D. A. Improved recovery of the hemodynamic response in diffuse optical imaging using short optode separations and state-space modeling. *NeuroImage*, 56(3):1362–71, 2011.

Gagnon, L., Cooper, R. J., Yücel, M. A., Perdue, K. L., Greve, D. N., and Boas, D. A. Short separation channel location impacts the performance of short channel regression in NIRS. *NeuroImage*, 59(3):2518–28, 2012a.

Gagnon, L., Yücel, M. A., Dehaes, M., Cooper, R. J., Perdue, K. L., Selb, J., Huppert, T. J., Hoge, R. D., and Boas, D. A. Quantification of the cortical contribution to the NIRS signal over the motor cortex using concurrent NIRS-fMRI measurements. *NeuroImage*, 59(4):3933–40, 2012b.

Gagnon, L., Yücel, M. A., Boas, D. A., and Cooper, R. J. Further improvement in reducing superficial contamination in NIRS using double short separation measurements. *NeuroImage*, 85 Pt 1:127–35, 2014.

Gibson, A. P., Hebden, J. C., and Arridge, S. R. Recent advances in diffuse optical imaging. *Physics in medicine and biology*, 50(4):R1–43, 2005.

Glover, G. H. Deconvolution of impulse response in event-related BOLD fMRI. *NeuroImage*, 9(4):416–29, 1999.

Gregg, N. M., White, B. R., Zeff, B. W., Berger, A. J., and Culver, J. P. Brain specificity of diffuse optical imaging: improvements from superficial signal regression and tomography. *Frontiers in neuroenergetics*, 2, 2010.

Grewal, M. and Andrews, A. *Kalman Filtering: Theory and Practice Using MATLAB*. John Wiley & Sons, Ltd, New York, 2nd edition, 2001.

Guven, M., Yazici, B., Intes, X., and Chance, B. Diffuse optical tomography with a priori anatomical information. *Physics in medicine and biology*, 50(12):2837–58, 2005.

Habermehl, C., Holtze, S., Steinbrink, J., Koch, S. P., Obrig, H., Mehnert, J., and Schmitz, C. H. Somatosensory activation of two fingers can be discriminated with ultrahigh-density diffuse optical tomography. *NeuroImage*, 59(4):3201–11, 2012.

Händel, P. Evaluation of a standardized sine wave fit algorithm. In *Proceedings of the IEEE Nordic Signal Processing Symposium, Sweden*, 2000.

Handy, T. C. *Event-related potentials: A methods handbook*. The MIT Press, 2005.

Haykin, S. *Kalman filtering and neural networks*. John Wiley & Sons, Ltd, New York, 2001.

Heiskala, J., Pollari, M., Metsäranta, M., Grant, P. E., and Nissilä, I. Probabilistic atlas can improve reconstruction from optical imaging of the neonatal brain. *Optics express*, 17(17):14977–92, 2009.

Holper, L., Biallas, M., and Wolf, M. Task complexity relates to activation of cortical motor areas during uni- and bimanual performance: a functional NIRS study. *NeuroImage*, 46(4):1105–13, 2009.

Homae, F. A brain of two halves: Insights into interhemispheric organization provided by near-infrared spectroscopy. *NeuroImage*, 85 Pt 1: 354–62, 2014.

Hoshi, Y. and Tamura, M. Detection of dynamic changes in cerebral oxygenation coupled to neuronal function during mental work in man. *Neuroscience letters*, 150(1):5–8, 1993.

Huppert, T. J., Hoge, R. D., Diamond, S. G., Franceschini, M. A., and Boas, D. A. A temporal comparison of BOLD, ASL, and NIRS hemodynamic responses to motor stimuli in adult humans. *NeuroImage*, 29(2):368–82, 2006.

Huppert, T. J., Diamond, S. G., Franceschini, M. A., and Boas, D. A. HomER: a review of time-series analysis methods for near-infrared spectroscopy of the brain. *Applied optics*, 48(10):D280–98, 2009.

Imai, M., Watanabe, H., Yasui, K., Kimura, Y., Shitara, Y., Tsuchida, S., Takahashi, N., and Taga, G. Functional connectivity of the cortex of term and preterm infants and infants with Down's syndrome. *NeuroImage*, 85 Pt 1:272–8, 2014.

Inoue, Y., Sakihara, K., Gunji, A., Ozawa, H., Kimiya, S., Shinoda, H., Kaga, M., and Inagaki, M. Reduced prefrontal hemodynamic response in children with ADHD during the Go/NoGo task: a NIRS study. *Neuroreport*, 23(2):55–60, 2012.

Izzetoglu, M., Chitrapu, P., Bunce, S., and Onaral, B. Motion artifact cancellation in NIR spectroscopy using discrete Kalman filtering. *Biomedical engineering online*, 9:16, 2010.

Jang, K. E., Tak, S., Jung, J., Jang, J., Jeong, Y., and Ye, J. C. Wavelet minimum description length detrending for near-infrared spectroscopy. *Journal of biomedical optics*, 14(3):034004, 2009.

Jasdzewski, G., Strangman, G., Wagner, J., Kwong, K. K., Poldrack, R. A., and Boas, D. A. Differences in the hemodynamic response to event-related motor and visual paradigms as measured by near-infrared spectroscopy. *NeuroImage*, 20(1):479–88, 2003.

Jenkinson, M., Pechaud, M., and Smith, S. Bet2: Mr-based estimation of brain, skull and scalp surfaces. In *Eleventh annual meeting of the organization for human brain mapping*, volume 17, 2005.

Jöbsis, F. F. Noninvasive, infrared monitoring of cerebral and myocardial oxygen sufficiency and circulatory parameters. *Science*, 198(4323): 1264–7, 1977.

Jourdan Moser, S., Cutini, S., Weber, P., and Schroeter, M. L. Right prefrontal brain activation due to Stroop interference is altered in attention-deficit hyperactivity disorder - A functional near-infrared spectroscopy study. *Psychiatry research*, 173(3):190–5, 2009.

Julien, C. The enigma of Mayer waves: Facts and models. *Cardiovascular research*, 70(1):12–21, 2006.

Jurcak, V., Tsuzuki, D., and Dan, I. 10/20, 10/10, and 10/5 systems revisited: their validity as relative head-surface-based positioning systems. *NeuroImage*, 34(4):1600–11, 2007.

Kaiser, V., Bauernfeind, G., Kreilinger, A., Kaufmann, T., Kübler, A., Neuper, C., and Müller-Putz, G. R. Cortical effects of user training in a motor imagery based brain-computer interface measured by fNIRS and EEG. *NeuroImage*, 85 Pt 1:432–44, 2014.

Kamran, M. A. and Hong, K.-S. Linear parameter-varying model and adaptive filtering technique for detecting neuronal activities: an fNIRS study. *Journal of neural engineering*, 10(5):056002, 2013.

Kasess, C. H., Windischberger, C., Cunnington, R., Lanzenberger, R., Pezawas, L., and Moser, E. The suppressive influence of SMA on M1 in motor imagery revealed by fMRI and dynamic causal modeling. *NeuroImage*, 40(2):828–37, 2008.

Kato, T., Kamei, A., Takashima, S., and Ozaki, T. Human visual cortical function during photic stimulation monitoring by means of near-infrared spectroscopy. *Journal of cerebral blood flow and metabolism*, 13(3): 516–20, 1993.

Kazemi, K., Moghaddam, H. A., Grebe, R., Gondry-Jouet, C., and Wallois, F. A neonatal atlas template for spatial normalization of whole-brain magnetic resonance images of newborns: preliminary results. *NeuroImage*, 37(2):463–73, 2007.

Kirilina, E., Jelzow, A., Heine, A., Niessing, M., Wabnitz, H., Brühl, R., Ittermann, B., Jacobs, A. M., and Tachtsidis, I. The physiological origin of task-evoked systemic artefacts in functional near infrared spectroscopy. *NeuroImage*, 61(1):70–81, 2012.

Kita, Y., Gunji, A., Inoue, Y., Goto, T., Sakihara, K., Kaga, M., Inagaki, M., and Hosokawa, T. Self-face recognition in children with autism spectrum disorders: a near-infrared spectroscopy study. *Brain & development*, 33(6):494–503, 2011.

Koenraadt, K. L. M., Roelofsen, E. G. J., Duysens, J., and Keijsers, N. L. W. Cortical control of normal gait and precision stepping: An fNIRS study. *NeuroImage*, 85 Pt 1:415–22, 2014.

Kuklisova-Murga sova, M., Aljabar, P., Srinivasan, L., Counsell, S. J., Doria, V., Serag, A., Gousias, I. S., Boardman, J. P., Rutherford, M. A., Edwards, A. D., Hajnal, J. V., and Rueckert, D. A dynamic 4D probabilistic atlas of the developing brain. *NeuroImage*, 54(4):2750–63, 2011.

Kwong, K. K., Belliveau, J. W., Chesler, D. A., Goldberg, I. E., Weisskoff, R. M., Poncelet, B. P., Kennedy, D. N., Hoppel, B. E., Cohen, M. S., and Turner, R. Dynamic magnetic resonance imaging of human brain activity during primary sensory stimulation. *Proceedings of the National Academy of Sciences of the United States of America*, 89(12):5675–9, 1992.

Ledig, C., Wolz, R., Aljabar, P., Lotjonen, J., Heckemann, R. A., Hammers, A., and Rueckert, D. Multi-class brain segmentation using atlas propagation and em-based refinement. In *Biomedical Imaging (ISBI), 2012 9th IEEE International Symposium on*, pages 896–899. IEEE, 2012.

Leff, D. R., Orihuela-Espina, F., Elwell, C. E., Athanasiou, T., Delpy, D. T., Darzi, A. W., and Yang, G.-Z. Assessment of the cerebral cortex during motor task behaviours in adults: a systematic review of functional near infrared spectroscopy (fNIRS) studies. *NeuroImage*, 54(4):2922–36, 2011.

Lin, P.-Y., Roche-Labarbe, N., Dehaes, M., Carp, S., Fenoglio, A., Barbieri, B., Hagan, K., Grant, P. E., and Franceschini, M. A. Non-invasive optical measurement of cerebral metabolism and hemodynamics in infants. *Journal of visualized experiments : JoVE*, (73):e4379, 2013.

Lina, J.-M., Dehaes, M., Matteau-Pelletier, C., and Lesage, F. Complex wavelets applied to diffuse optical spectroscopy for brain activity detection. *Optics express*, 16(2):1029–50, 2008.

Lina, J. M., Matteau-Pelletier, C., Dehaes, M., Desjardins, M., and Lesage, F. Wavelet-based estimation of the hemodynamic responses in diffuse optical imaging. *Medical image analysis*, 14(4):606–16, 2010.

Lindquist, M. A. and Wager, T. D. Validity and power in hemodynamic response modeling: a comparison study and a new approach. *Human brain mapping*, 28(8):764–84, 2007.

Liu, A. and Joe, B. Relationship between tetrahedron shape measures. *BIT Numerical Mathematics*, 34(2):268–287, 1994.

Lloyd-Fox, S., Blasi, A., and Elwell, C. E. Illuminating the developing brain: the past, present and future of functional near infrared spectroscopy. *Neuroscience and biobehavioral reviews*, 34(3):269–84, 2010.

Luck, S. J. and Vogel, E. K. The capacity of visual working memory for features and conjunctions. *Nature*, 390(6657):279–81, 1997.

Luck, S. J. *An introduction to the event-related potential technique (cognitive neuroscience)*. A Bradford Book, 2005.

Luria, R., Sessa, P., Gotler, A., Jolicoeur, P., and Dell'Acqua, R. Visual short-term memory capacity for simple and complex objects. *Journal of cognitive neuroscience*, 22(3):496–512, 2010.

Lutz, K., Koeneke, S., Wüstenberg, T., and Jäncke, L. Asymmetry of cortical activation during maximum and convenient tapping speed. *Neuroscience letters*, 373(1):61–6, 2005.

Luu, S. and Chau, T. Decoding subjective preference from single-trial near-infrared spectroscopy signals. *Journal of neural engineering*, 6(1): 016003, 2009.

Machado, A., Lina, J. M., Tremblay, J., Lassonde, M., Nguyen, D. K., Lesage, F., and Grova, C. Detection of hemodynamic responses to epileptic activity using simultaneous Electro-EncephaloGraphy (EEG)/Near Infra Red Spectroscopy (NIRS) acquisitions. *NeuroImage*, 56(1):114–25, 2011.

Mihara, M., Miyai, I., Hatakenaka, M., Kubota, K., and Sakoda, S. Sustained prefrontal activation during ataxic gait: a compensatory mechanism for ataxic stroke? *NeuroImage*, 37(4):1338–45, 2007.

Miller, K. L., Luh, W. M., Liu, T. T., Martinez, A., Obata, T., Wong, E. C., Frank, L. R., and Buxton, R. B. Nonlinear temporal dynamics of the cerebral blood flow response. *Human brain mapping*, 13(1):1–12, 2001.

Minagawa-Kawai, Y., Naoi, N., Kikuchi, N., Yamamoto, J.-I., Nakamura, K., and Kojima, S. Cerebral laterality for phonemic and prosodic cue decoding in children with autism. *Neuroreport*, 20(13):1219–24, 2009.

Miyai, I., Yagura, H., Oda, I., Konishi, I., Eda, H., Suzuki, T., and Kubota, K. Premotor cortex is involved in restoration of gait in stroke. *Annals of neurology*, 52(2):188–94, 2002.

Miyai, I., Yagura, H., Hatakenaka, M., Oda, I., Konishi, I., and Kubota, K. Longitudinal optical imaging study for locomotor recovery after stroke. *Stroke; a journal of cerebral circulation*, 34(12):2866–70, 2003.

Molavi, B. and Dumont, G. A. Wavelet-based motion artifact removal for functional near-infrared spectroscopy. *Physiological measurement*, 33(2): 259–70, 2012.

Muehlemann, T., Haensse, D., and Wolf, M. Wireless miniaturized in-vivo near infrared imaging. *Optics express*, 16(14):10323–30, 2008.

Murkin, J. M. and Arango, M. Near-infrared spectroscopy as an index of brain and tissue oxygenation. *British journal of anaesthesia*, 103 Suppl (suppl_1):i3–13, 2009.

Negoro, H., Sawada, M., Iida, J., Ota, T., Tanaka, S., and Kishimoto, T. Prefrontal dysfunction in attention-deficit/hyperactivity disorder as measured by near-infrared spectroscopy. *Child psychiatry and human development*, 41(2):193–203, 2010.

Niedermeyer, E. and da Silva, F. H. L. *Electroencephalography: basic principles, clinical applications, and related fields*. Wolters Kluwer Health, 2005.

Obrig, H. and Steinbrink, J. Non-invasive optical imaging of stroke. *Philosophical transactions. Series A, Mathematical, physical, and engineering sciences*, 369(1955):4470–94, 2011.

Ogawa, S., Tank, D. W., Menon, R., Ellermann, J. M., Kim, S. G., Merkle, H., and Ugurbil, K. Intrinsic signal changes accompanying sensory stimulation: functional brain mapping with magnetic resonance imaging. *Proceedings of the National Academy of Sciences of the United States of America*, 89(13):5951–5, 1992.

Oishi, K., Mori, S., Donohue, P. K., Ernst, T., Anderson, L., Buchthal, S., Faria, A., Jiang, H., Li, X., Miller, M. I., van Zijl, P. C. M., and Chang, L. Multi-contrast human neonatal brain atlas: application to normal neonate development analysis. *NeuroImage*, 56(1):8–20, 2011.

Oostenveld, R. and Praamstra, P. The five percent electrode system for high-resolution EEG and ERP measurements. *Clinical neurophysiology*, 112(4):713–9, 2001.

Plichta, M. M., Heinzel, S., Ehlis, A.-C., Pauli, P., and Fallgatter, A. J. Model-based analysis of rapid event-related functional near-infrared spectroscopy (NIRS) data: a parametric validation study. *NeuroImage*, 35(2):625–34, 2007.

Pogue, B. W. and Paulsen, K. D. High-resolution near-infrared tomographic imaging simulations of the rat cranium by use of a priori magnetic resonance imaging structural information. *Optics letters*, 23(21): 1716–8, 1998.

Pogue, B. W., Patterson, M. S., Jiang, H., and Paulsen, K. D. Initial assessment of a simple system for frequency domain diffuse optical tomography. *Physics in medicine and biology*, 40(10):1709–29, 1995.

Power, S. D., Kushki, A., and Chau, T. Automatic single-trial discrimination of mental arithmetic, mental singing and the no-control state from prefrontal activity: toward a three-state NIRS-BCI. *BMC research notes*, 5(1):141, 2012.

Prastawa, M., Gilmore, J. H., Lin, W., and Gerig, G. Automatic segmentation of MR images of the developing newborn brain. *Medical image analysis*, 9(5):457–66, 2005.

Prince, S., Kolehmainen, V., Kaipio, J. P., Franceschini, M. A., Boas, D., and Arridge, S. R. Time-series estimation of biological factors in optical diffusion tomography. *Physics in medicine and biology*, 48(11):1491–504, 2003.

Purves, D., Augustine, G. J., Fitzpatrick, D., Hall, W. C., Lamantia, A.-S., McNamara, J. O., and White, L. E. *Neuroscience*. Sinauer Associates, Inc., 4th edition, 2007.

Robertson, F. C., Douglas, T. S., and Meintjes, E. M. Motion artifact removal for functional near infrared spectroscopy: a comparison of methods. *IEEE transactions on bio-medical engineering*, 57(6):1377–87, 2010.

Robitaille, N., Marois, R., Todd, J., Grimault, S., Cheyne, D., and Jolicoeur, P. Distinguishing between lateralized and nonlateralized brain activity associated with visual short-term memory: fMRI, MEG, and EEG evidence from the same observers. *NeuroImage*, 53(4):1334–45, 2010.

Saager, R. and Berger, A. Measurement of layer-like hemodynamic trends in scalp and cortex: implications for physiological baseline suppression in functional near-infrared spectroscopy. *Journal of biomedical optics*, 13 (3):034017, 2008.

Saager, R. B. and Berger, A. J. Direct characterization and removal of interfering absorption trends in two-layer turbid media. *Journal of the Optical Society of America A*, 22(9):1874, 2005.

Sanchez, C. E., Richards, J. E., and Almli, C. R. Neurodevelopmental MRI brain templates for children from 2 weeks to 4 years of age. *Developmental psychobiology*, 54(1):77–91, 2012.

Sato, T., Ito, M., Suto, T., Kameyama, M., Suda, M., Yamagishi, Y., Ohshima, A., Uehara, T., Fukuda, M., and Mikuni, M. Time courses of brain activation and their implications for function: a multichannel near-infrared spectroscopy study during finger tapping. *Neuroscience research*, 58(3):297–304, 2007.

Scarpa, F., Cutini, S., Scatturin, P., Dell'Acqua, R., and Sparacino, G. Bayesian filtering of human brain hemodynamic activity elicited by visual short-term maintenance recorded through functional near-infrared spectroscopy (fNIRS). *Optics express*, 18(25):26550–68, 2010.

Scarpa, F., Brigadoi, S., Cutini, S., Scatturin, P., Zorzi, M., Dell'acqua, R., and Sparacino, G. A reference-channel based methodology to improve estimation of event-related hemodynamic response from fNIRS measurements. *NeuroImage*, 72:106–19, 2013.

Schneider, S., Christensen, A., Häuß inger, F. B., Fallgatter, A. J., Giese, M. A., and Ehlis, A.-C. Show me how you walk and I tell you how you feel - A functional near-infrared spectroscopy study on emotion perception based on human gait. *NeuroImage*, 85 Pt 1:380–90, 2014.

Scholkmann, F., Spichtig, S., Muehlemann, T., and Wolf, M. How to detect and reduce movement artifacts in near-infrared imaging using moving standard deviation and spline interpolation. *Physiological measurement*, 31(5):649–62, 2010.

Scholkmann, F., Kleiser, S., Metz, A. J., Zimmermann, R., Mata Pavia, J., Wolf, U., and Wolf, M. A review on continuous wave functional near-infrared spectroscopy and imaging instrumentation and methodology. *NeuroImage*, 85 Pt 1:6–27, 2014.

Schweiger, M. and Arridge, S. R. Optical tomographic reconstruction in a complex head model using a priori region boundary information. *Physics in medicine and biology*, 44(11):2703–21, 1999.

Schweiger, M., Arridge, S. R., Hiraoka, M., and Delpy, D. T. The finite element method for the propagation of light in scattering media: boundary and source conditions. *Medical physics*, 22(11 Pt 1):1779–92, 1995.

Sharp, D. J., Bonnelle, V., De Boissezon, X., Beckmann, C. F., James, S. G., Patel, M. C., and Mehta, M. A. Distinct frontal systems for response inhibition, attentional capture, and error processing. *Proceedings of the National Academy of Sciences of the United States of America*, 107(13):6106–11, 2010.

Shi, F., Yap, P.-T., Wu, G., Jia, H., Gilmore, J. H., Lin, W., and Shen, D. Infant brain atlases from neonates to 1- and 2-year-olds. *PloS one*, 6(4): e18746, 2011.

Shulman, R. G. and Rothman, D. L., editors. *Brain Energetics and Neuronal Activity*. John Wiley & Sons, Ltd, Chichester, UK, 2004.

Singh, A. K., Okamoto, M., Dan, H., Jurcak, V., and Dan, I. Spatial registration of multichannel multi-subject fNIRS data to MNI space without MRI. *NeuroImage*, 27(4):842–51, 2005.

Southgate, V., Begus, K., Lloyd-Fox, S., di Gangi, V., and Hamilton, A. Goal representation in the infant brain. *NeuroImage*, 85 Pt 1:294–301, 2014.

Tachtsidis, I., Leung, T. S., Chopra, A., Koh, P. H., Reid, C. B., and Elwell, C. E. False positives in functional near-infrared topography. *Advances in experimental medicine and biology*, 645:307–14, 2009.

Tarvainen, T., Vauhkonen, M., Kolehmainen, V., and Kaipio, J. P. Hybrid radiative-transfer-diffusion model for optical tomography. *Applied optics*, 44(6):876–86, 2005.

Tian, F. and Liu, H. Depth-compensated diffuse optical tomography enhanced by general linear model analysis and an anatomical atlas of human head. *NeuroImage*, 85 Pt 1:166–80, 2014.

Todd, J. J. and Marois, R. Capacity limit of visual short-term memory in human posterior parietal cortex. *Nature*, 428(6984):751–4, 2004.

Tong, Y. and Frederick, B. D. Time lag dependent multimodal processing of concurrent fMRI and near-infrared spectroscopy (NIRS) data suggests a global circulatory origin for low-frequency oscillation signals in human brain. *NeuroImage*, 53(2):553–64, 2010.

Tong, Y., Bergethon, P. R., and Frederick, B. D. An improved method for mapping cerebrovascular reserve using concurrent fMRI and near-infrared spectroscopy with Regressor Interpolation at Progressive Time Delays (RIPTiDe). *NeuroImage*, 56(4):2047–57, 2011.

Torricelli, A., Contini, D., Pifferi, A., Caffini, M., Re, R., Zucchelli, L., and Spinelli, L. Time domain functional NIRS imaging for human brain mapping. *NeuroImage*, pages 28–50, 2014.

Tsuzuki, D. and Dan, I. Spatial registration for functional near-infrared spectroscopy: From channel position on the scalp to cortical location in individual and group analyses. *NeuroImage*, 85 Pt 1:92–103, 2014.

Tsuzuki, D., Cai, D.-s., Dan, H., Kyutoku, Y., Fujita, A., Watanabe, E., and Dan, I. Stable and convenient spatial registration of stand-alone NIRS data through anchor-based probabilistic registration. *Neuroscience research*, 72(2):163–71, 2012.

Tupak, S. V., Dresler, T., Guhn, A., Ehlis, A.-C., Fallgatter, A. J., Pauli, P., and Herrmann, M. J. Implicit emotion regulation in the presence of threat: Neural and autonomic correlates. *NeuroImage*, 85 Pt 1:372–9, 2014.

Twomey, S. The application of numerical filtering to the solution of integral equations encountered in indirect sensing measurements. *Journal of the Franklin Institute*, 279(2):95–109, 1965.

Vanderwert, R. E. and Nelson, C. A. The use of near-infrared spectroscopy in the study of typical and atypical development. *NeuroImage*, 85 Pt 1:264–71, 2014.

Villringer, A., Planck, J., Hock, C., Schleinkofer, L., and Dirnagl, U. Near infrared spectroscopy (NIRS): a new tool to study hemodynamic changes during activation of brain function in human adults. *Neuroscience letters*, 154(1-2):101–4, 1993.

Virtanen, J., Noponen, T., and Meriläinen, P. Comparison of principal and independent component analysis in removing extracerebral interference from near-infrared spectroscopy signals. *Journal of biomedical optics*, 14(5):054032, 2009.

Virtanen, J., Noponen, T., Kotilahti, K., Virtanen, J., and Ilmoniemi, R. J. Accelerometer-based method for correcting signal baseline changes

caused by motion artifacts in medical near-infrared spectroscopy. *Journal of biomedical optics*, 16(8):087005, 2011.

Vogel, E. K. and Machizawa, M. G. Neural activity predicts individual differences in visual working memory capacity. *Nature*, 428(6984):748–51, 2004.

Wallois, F., Patil, A., Héberlé, C., and Grebe, R. EEG-NIRS in epilepsy in children and neonates. *Neurophysiologie clinique = Clinical neurophysiology*, 40(5-6):281–92, 2010.

Wallois, F., Mahmoudzadeh, M., Patil, A., and Grebe, R. Usefulness of simultaneous EEG-NIRS recording in language studies. *Brain and language*, 121(2):110–23, 2012.

Weber, P., Lütschg, J., and Fahnenstich, H. Cerebral hemodynamic changes in response to an executive function task in children with attention-deficit hyperactivity disorder measured by near-infrared spectroscopy. *Journal of developmental and behavioral pediatrics : JDBP*, 26(2):105–11, 2005.

White, B. R., Liao, S. M., Ferradal, S. L., Inder, T. E., and Culver, J. P. Bedside optical imaging of occipital resting-state functional connectivity in neonates. *NeuroImage*, 59(3):2529–38, 2012.

Wilcox, T., Bortfeld, H., Woods, R., Wruck, E., and Boas, D. A. Using near-infrared spectroscopy to assess neural activation during object processing in infants. *Journal of biomedical optics*, 10(1):11010, 2005.

Wilcox, T., Hirshkowitz, A., Hawkins, L., and Boas, D. A. The effect of color priming on infant brain and behavior. *NeuroImage*, 85 Pt 1:302–13, 2014.

Wilke, M., Schmithorst, V. J., and Holland, S. K. Normative pediatric brain data for spatial normalization and segmentation differs from standard adult data. *Magnetic resonance in medicine*, 50(4):749–57, 2003.

Xiao, T., Xiao, Z., Ke, X., Hong, S., Yang, H., Su, Y., Chu, K., Xiao, X., Shen, J., and Liu, Y. Response inhibition impairment in high functioning autism and attention deficit hyperactivity disorder: evidence from near-infrared spectroscopy data. *PloS one*, 7(10):e46569, 2012.

Xu, Y., Zhang, Q., and Jiang, H. Optical image reconstruction of non-scattering and low scattering heterogeneities in turbid media based on

the diffusion approximation model. *Journal of Optics A: Pure and Applied Optics*, 6(1):29–35, 2004.

Ye, J. C., Tak, S., Jang, K. E., Jung, J., and Jang, J. NIRS-SPM: statistical parametric mapping for near-infrared spectroscopy. *NeuroImage*, 44(2): 428–47, 2009.

Yuan, Z. and Ye, J. Fusion of fNIRS and fMRI data: identifying when and where hemodynamic signals are changing in human brains. *Frontiers in human neuroscience*, 7:676, 2013.

Yücel, M. A., Huppert, T. J., Boas, D. A., and Gagnon, L. Calibrating the BOLD signal during a motor task using an extended fusion model incorporating DOT, BOLD and ASL data. *NeuroImage*, 61(4):1268–76, 2012.

Zhan, Y., Eggebrecht, A. T., Culver, J. P., and Dehghani, H. Image quality analysis of high-density diffuse optical tomography incorporating a subject-specific head model. *Frontiers in neuroenergetics*, 4:6, 2012.

Zhang, Q., Brown, E. N., and Strangman, G. E. Adaptive filtering for global interference cancellation and real-time recovery of evoked brain activity: a Monte Carlo simulation study. *Journal of biomedical optics*, 12 (4):044014, 2007a.

Zhang, Q., Brown, E. N., and Strangman, G. E. Adaptive filtering to reduce global interference in evoked brain activity detection: a human subject case study. *Journal of biomedical optics*, 12(6):064009, 2007b.

Zhang, Q., Strangman, G. E., and Ganis, G. Adaptive filtering to reduce global interference in non-invasive NIRS measures of brain activation: how well and when does it work? *NeuroImage*, 45(3):788–94, 2009.

Zhang, X., Toronov, V., and Webb, A. Simultaneous integrated diffuse optical tomography and functional magnetic resonance imaging of the human brain. *Optics express*, 13(14):5513–21, 2005a.

Zhang, Y., Sun, J. W., and Rolfe, P. RLS adaptive filtering for physiological interference reduction in NIRS brain activity measurement: a Monte Carlo study. *Physiological Measurement*, 33(6):925–942, 2012.

Zhang, Y., Brooks, D. H., Franceschini, M. A., and Boas, D. A. Eigenvector-based spatial filtering for reduction of physiological interference in diffuse optical imaging. *Journal of biomedical optics*, 10(1): 11014, 2005b.

Acknowledgments

First and foremost, I would like to thank my advisor, Prof. Roberto Dell'Acqua, for having always supported me and for the possibility he offered me in these three years to pursue my interests, being at the same time always present when needed. I would like to express my sincere gratitude also to my co-supervisor, Prof. Giovanni Sparacino, for the great advices and fruitful discussions on the methodological aspects of my work. A big thanks goes to the fNIRS group of the University of Padova (Simone Cutini, Fabio Scarpa and Pietro Scatturin): without you this thesis would have never been possible.

I want to express my thankfulness also to Prof. David Boas (Martinos Center for Biomedical Imaging, Boston, U.S.A.) and Prof. Jem Hebden (University College London, U.K.) for having welcomed me in their laboratories as one of their students and having allowed me to deepen my knowledge on optical techniques. Thanks also to the members of these two groups: working with you has been very educative. A particular thanks goes to Rob Cooper: working with you in these two years has been one of the best things that happened in my working life: thanks for everything.

Of course I cannot miss thanking all my Ph.D. students colleagues, above all the cognitive science group (Lisa Ceccherini, Mario Dalmaso, Federica Meconi, Dorina Hysenbelli): we spent three wonderful years together.

Finally I would also like to thank my parents, my sister and my whole enlarged family for being always present and supportive. A particular thanks to Marco Castellaro for having stand me during these three years and particularly during the writing of this thesis.